

UNCLASSIFIED

AD NUMBER

ADB059461

NEW LIMITATION CHANGE

TO

**Approved for public release, distribution
unlimited**

FROM

**Distribution authorized to U.S. Gov't.
agencies only; Test and Evaluation; Jun
1981. Other requests shall be referred to
Air Force Materials Lab., Polymer Branch,
Wright-Patterson AFB, OH 45433.**

AUTHORITY

AFWAL ltr, 19 Nov 1982

THIS PAGE IS UNCLASSIFIED

OFFICIAL FILE COPY



AFWAL-TR-80-4045 Volume II

ADB059461

MECHANICAL PROPERTIES VS MORPHOLOGY OF ORDERED POLYMERS, VOLUME II

E. L. Thomas, R. J. Farris, S. L. Hsu, S. Allen, A. Filippov, J. Minter,
E. Roche, K. Shimamura, T. Takahashi and G. Venkatesh

Polymer Science & Engineering Dept.
The University of Massachusetts
Amherst, MA 01003

July 1981

TECHNICAL REPORT AFWAL-TR-80-4045, Volume II

INTERIM TECHNICAL REPORT COVERING PERIOD 1 SEPTEMBER 1979 THROUGH 30 AUGUST 1980

Distribution limited to U.S. Government agencies only (test and evaluation);
July 1981. Other requests for this document must be referred to AFWAL/MLBP,
Materials Laboratory, Nonmetallic Materials Division, Polymer Branch,
Wright-Patterson Air Force Base, Ohio 45433

SUBJECT TO EXPORT CONTROL LAWS

This document contains information for manufacturing or using munitions of war. Export of the information contained herein, or release to foreign nationals within the United States, without first obtaining an export license, is a violation of the International Traffic-in-Arms Regulations. Such violation is subject to a penalty of up to 2 years imprisonment and a fine of \$100,000 under 22 USC 2778.

Include this notice with any reproduced portion of this document.

20040226204

MATERIALS LABORATORY
AIR FORCE WRIGHT AERONAUTICAL LABORATORIES
AIR FORCE SYSTEMS COMMAND
WRIGHT-PATTERSON AIR FORCE BASE, OHIO 45433

OFFICIAL FILE COPY

BEST AVAILABLE COPY

NOTICE

When Government drawings, specifications, or other data are used for any purpose other than in connection with a definitely related Government procurement operation, the United States Government thereby incurs no responsibility nor any obligation whatsoever; and the fact that the Government may have formulated, furnished, or in any way supplied the said drawings, specifications, or other data, is not to be regarded by implication or otherwise as in any manner licensing the holder or any other person or corporation, or conveying any rights or permission to manufacture, use, or sell any patented invention that may in any way be related thereto.

This technical report has been reviewed and is approved for publication.

Michael W. Wellman

MICHAEL W. WELLMAN, Captain, USAF
Project Monitor

R. L. Van Deuse

R. L. VAN DEUSEN, Chief
Polymer Branch
Nonmetallic Materials Division

FOR THE COMMANDER

F. D. Cherry

FRANK D. CHERRY, Chief
Nonmetallic Materials Division

"If your address has changed, if you wish to be removed from our mailing list, or if the addressee is no longer employed by your organization please notify AFWAL/MLBP, W-PAFB, Ohio 45433 to help us maintain a current mailing list.

Copies of this report should not be returned unless return is required by security considerations, contractual obligations, or notice on a specific document.

REPORT DOCUMENTATION PAGE		READ INSTRUCTIONS BEFORE COMPLETING FORM
1. REPORT NUMBER AFWAL/TR-80-4045, Volume II	2. GOVT ACCESSION NO.	3. RECIPIENT'S CATALOG NUMBER
4. TITLE (and Subtitle) MECHANICAL PROPERTIES VS MORPHOLOGY OF ORDERED POLYMERS VOLUME II		5. TYPE OF REPORT & PERIOD COVERED Interim, End of second year effort. 1 Sept 79 - 30 Aug 80
		6. PERFORMING ORG. REPORT NUMBER
7. AUTHOR(s) E.L. Thomas, R.J. Farris, S.L. Hsu, S. Allen, A. Filippov, J. Minter, E. Roche, K. Shimamura, T. Takahashi and G. Venkatesh		8. CONTRACT OR GRANT NUMBER(s) F33615-78-C-5175
9. PERFORMING ORGANIZATION NAME AND ADDRESS Polymer Science and Engineering Department The University of Massachusetts Amherst, MA 01003		10. PROGRAM ELEMENT, PROJECT, TASK AREA & WORK UNIT NUMBERS 24190407
11. CONTROLLING OFFICE NAME AND ADDRESS Materials Laboratory (AFWAL/MLBP) Air Force Wright Aeronautical Laboratories (AFSC) Wright-Patterson Air Force Base, OH 45433		12. REPORT DATE July 1981
14. MONITORING AGENCY NAME & ADDRESS (if different from Controlling Office)		13. NUMBER OF PAGES 137
		15. SECURITY CLASS. (of this report) Unclassified
		15a. DECLASSIFICATION/DOWNGRADING SCHEDULE
16. DISTRIBUTION STATEMENT (of this Report) Distribution limited to U.S. Government agencies only (test and evaluation); July 1981. Other request for this document must be referred to the Materials Laboratory, Nonmetallic Materials Division, Polymer Branch, AFWAL/MLBP, Wright-Patterson Air Force Base, Ohio 45433.		
17. DISTRIBUTION STATEMENT (of the abstract entered in Block 20, if different from Report)		
18. SUPPLEMENTARY NOTES		
19. KEY WORDS (Continue on reverse side if necessary and identify by block number) Heterocyclic Polymers Rodlike Polymers High Modulus High Strength		
20. ABSTRACT (Continue on reverse side if necessary and identify by block number) Morphological techniques in conjunction with mechanical testing have been employed to elucidate the relationships between mechanical properties of rigid rod polymer fiber and film with sample microstructures and to use this knowledge to obtain the maximum in strength and modulus for these materials. The fibers and films of poly(p-phenylene benzobisthiazole) (PBT) which have been investigated were produced at Carnegie Mellon University and at Celanese Research Corporation from liquid crystalline solutions using a dry-jet-wet spin process		

for fibers and either shear or extrusion for films. Correlation of sample microstructure and resultant mechanical properties with processing conditions has been done to help optimize processing conditions.

Microstructural studies involve predominantly scanning and transmission electron microscopy, wide angle x-ray scattering and electron diffraction. Mechanical behavior has been assessed in uniaxial tensile, fatigue, bending and torsion. Tensile properties have been measured over the range -100°C to +200°C. Studies of low molecular weight model compounds and poly-p-phenylene benzobisoxazole (PBO) and PBT polymers in solution and solid states have also been done by laser Raman and Fourier transform infrared spectroscopy.

Spectroscopic studies suggest that the polymers in solution exist in the protonated form. Model compounds have proven to be extremely helpful in this study, because they can be dissolved in non-protonic solvent such as chloroform, or in strong acid such as MSA or CSA. Quantitative assignments for the vibrations observed and their changes have elucidated the protonation effect for these polymers.

Morphological studies focused on determining the molecular orientation and lateral ordering in the polymer using a variety of morphological techniques, notably, wide angle x-ray scattering, electron diffraction, high resolution lattice imaging and dark field electron microscopy and small angle neutron scattering. Additional morphological studies were directed at determining processing microstructure relations and the degree of residual stress and residual solvent retained in the fiber or film after processing and after additional heat treatment.

While most of the materials produced to date have extremely high degrees of orientation, thus far, the key differences have been in the lateral ordering of the chains. Better lateral ordering has been observed in heat treated samples, and in particular, samples processed directly from the polymerization solvent, polyphosphoric acid, but no true 3-dimensional crystal structure is formed. It remains to be seen if this feature is a direct consequence of the chemical structure of PBT molecules or is simply the result of non-optimized processing and heat treatment conditions.

The surprisingly nonlinear behavior and apparent plasticity of the as-spun fibers and the modulus increase after plastic deformation caused considerable concern. These effects are caused by microstructural element buckling due to residual stresses produced during the fiber formation process. This hypothesis has been experimentally confirmed by both mechanical tests and microscopic examination of the fibers. Although the ultimate fiber properties are still limited by defects, it appears that better fibers are being produced as knowledge about the spinning and coagulation process is gained.

FOREWORD

This report covers the work performed by the University of Massachusetts, Amherst, Massachusetts 01003, on "Mechanical Properties versus Morphology of Ordered Polymers". The work was conducted under contract F33615-78-C-5175 for the Materials Laboratory. The performance period was from 1 September 1979 to 1 September 1980. This report was submitted in December 1980.

The work was performed in the Polymer Science and Engineering Department with Professor Edwin L. Thomas acting as principal investigator, and Professors R.J. Farris and S.L. Hsu as coprincipal investigators. The assistance of Messrs. S. Allen, A. Filippov and J. Minter and Drs. E. Roche, K. Shimamura, T. Takahashi and G. Venkatesh is gratefully acknowledged. The project engineer was Captain Michael W. Wellman, AFWAL/MLBP, Materials Laboratory, Wright-Patterson Air Force Base, Ohio.

TABLE OF CONTENTS

	PAGE
SECTION 1: OVERVIEW.....	1
1.1 Spectroscopic Studies.....	2
1.2 Morphological Studies.....	3
1.3 Mechanical Studies.....	5
SECTION 2: SPECTROSCOPY.....	6
2.1 Introduction.....	6
2.2 Experimental.....	7
2.3 Discussion.....	8
2.4 Summary.....	16
SECTION 3: MORPHOLOGICAL INVESTIGATIONS.....	42
3.1 The Structure of PBT.....	42
3.2 Light Optical Microscopy of PBT.....	45
3.2.1 Coagulation Studies.....	45
3.2.2 Void Content of Fibers.....	46
3.2.3 Light Microscopy of Ribbons.....	47
3.3 SEI and X-ray Microanalysis of Tapes.....	49
3.4 TEM Studies of Fibers and Tapes.....	49
3.4.1 Diffraction Studies.....	50
3.4.2 Radiation Damage.....	50

TABLE OF CONTENTS (cont'd.)

3.4.3	Image of Coherently Scattering Regions.....	51
3.4.4	Effect of Heat Treatment as Assessed by Dark Field Imaging.....	52
3.4.5	Deformation Bands.....	53
3.4.6	Microtoming.....	54
3.4.7	Lattice Imaging of PBT.....	54
3.5	SAXS of PBT Fibers and Ribbons.....	55
3.6	SANS of PBT Solutions and Tapes.....	55
SECTION 4: MECHANICAL PROPERTIES.....		99
4.1	Tensile Properties.....	99
4.2	Stress-Strain Behavior of As-Spun Fibers.....	99
4.3	Stress-Strain Behavior of Heat Treated Fibers.....	100
4.4	Review of the Mechanical Behavior-Microstructure Observations.....	100
4.5	Internal Stress Model.....	102
4.6	Mechanism of Plastic Deformation.....	104
4.7	Increase of Elastic Modulus During Plastic Deformation.....	105
4.8	Change of Mechanical Properties with Annealing.....	106
4.9	Fatigue Properties.....	108
4.10	Fatigue Properties of Heat Treated Fibers.....	109
4.11	Fatigue Properties of As-Spun Fibers.....	110

TABLE OF CONTENTS (concluded)

4.12 Torsion Tests.....	111
4.13 Environmental Effects.....	112
REFERENCES.....	135

LIST OF ILLUSTRATIONS

FIGURE	PAGE
2.1 Infrared spectrum of c-PBO model compounds in KBr.....	24
2.2 Infrared spectrum of t-PBT model compounds in KBr.....	25
2.3 Raman spectra of model compounds in the solid state	
(a) c-PBO.....	26
(b) t-PBO.....	27
(c) t-PBT.....	28
(d) c-PBT.....	29
2.4 Low frequency Raman spectra of t-PBO at 296°K and 110°K....	30
2.5 Ultraviolet absorption spectra of the model compounds in CHCl ₃ :	
(a) c-PBO.....	31
(b) t-PBO.....	32
(c) t-PBT.....	33
(d) c-PBT.....	34
2.6 Raman spectrum of t-PBT in CHCl ₃	35
2.7 Raman spectrum of t-PBO in CHCl ₃	36
2.8 Raman spectra of the model compounds in 100% H ₂ SO ₄	
(a) c-PBO.....	37
(b) t-PBO.....	38
(c) t-PBT.....	39
(d) c-PBT.....	40

LIST OF ILLUSTRATIONS (cont'd.)

FIGURE

2.9	Effect of acid concentration on the Raman spectrum of t-PBO in CHCl_3	41
3.1	Structure of PBT proposed by Roche <u>et al</u> (A) <u>a b</u> projection of unit cell (B) Schematic view showing packing of chains (C) Comparison between projection of unit cells proposed by Roche [23] and Atkins [24].....	62
3.1c	Comparison between projection of unit cells proposed by Roche [23] and Atkins [24].....	63
3.2	Refined structure of PBT A. <u>a b</u> projection of PBT unit cell B. Schematic view of packing of chains.....	64
3.3	Cylindrically averaged Fourier transform of a single PBT chain.....	65
3.4	Cylindrically averaged Fourier transform from a single PBT chain of 10 repeat units.....	66
3.5	Comparison between electron diffraction from PBT and cylindrically averaged transform.....	67
3.6	Schlieren texture in 9% PBT in MSA after 48 hours relaxation.	68
3.7	Inversion wall in 9% PBT in MSA as a function of orientation: polarizer vertical, analyser horizontal.....	69
3.8	Anisotropic PBT/MSA domains in an isotropic matrix as viewed by interference and polarized light microscopy.....	70

LIST OF ILLUSTRATIONS (cont'd)

FIGURE

3.9	(A) Radial structure of 1.2% PBT coagulated with H ₂ O (crossed polars) (B) enlarged view of one radial branch (C) interference micrograph of area like (B).....	71
3.10	(A) Interference micrograph of 1.7% PPTA coagulated with H ₂ O (b) crossed polars.....	72
3.11	Coagulation of a drop of 6.2 wt% PBT in MSA with H ₂ O.....	73
3.12	(a) PBT 27554-42-1 475°C heat treatment (b) PBT 27554-24-8B typical 'as spun' fiber.....	74
3.13	Reflected light micrograph of PBT films (a) PBT 3271-9-4 as extruded, side 1..... (b) PBT 3271-9-4 as extruded, side 2..... (c) PBT 3271-9-4 annealed at 475°C, side 1..... (d) PBT 3271-9-4 annealed at 475°C, side 2.....	75 76 77 78
3.14	Reflected polarized light micrograph of PBT-28555-25-4 (a) side 1 (b) side 2.....	79
3.15	Reflected polarized light micrograph of PBT-28555-25-4 annealed at 475°C (a) side 1 (b) side 2.....	80
3.16	SEI of PBT film from PPA solution.....	81
3.17	Xray microanalysis of PBT film from PPA.....	82
3.18	WAXD and SAED of as extruded and annealed PBT films.....	83
3.19	Decrease of scattered intensity from e ₂ ,e ₃ ,e ₄ reflections from PBT.....	84

LIST OF ILLUSTRATIONS (Cont'd.)

FIGURE

3.20	Determination of D^* for e_{2-4} reflections from PBT 28555-25-4.	85
3.21	BF/DF pair from PBT 28555-25-4 annealed at 475°C prepared by detachment replication.....	86
3.22	Successive DF images from e_1 and e_{2-4} reflections PBT 28555-25-4 annealed at 475°C.....	87
3.23	DF image from PBT 28555-19-2 as spun.....	88
3.24	DF image from 28555-19-5 as spun.....	89
3.25	DF image from heat treated PBT 28413-40-1.....	90
3.26	DF image from heat treated PBT 28413-40-4.....	91
3.27	Kink bands observed in PBT fibers prepared by sonication.....	92
3.28	Microdensitometry of SAED from PBT 28413-40-1 rolled at 400°C	93
3.29	DF image from rolled specimen of PBT 28413-40-1 from e_1	94
3.30	Microtomed section of PBT fiber embedded in epoxy.....	95
3.31	Axial bright field lattice image of PBT showing 5.8 Å lattice spacing.....	96
3.32	SAXS from as-spun PBT fibers.....	97
3.33	SAXS from annealed PBT fibers.....	98
4.1	Stress-strain behavior of as-spun PBT fibers.....	115
4.2	Stress-strain behavior of free annealed fibers.....	116
4.3	Comparison of heat treated and as-spun fiber behavior.....	117
4.4	Fibrillar morphology of PBT fibers revealed by mechanical peeling.....	118
4.5	Representation of axial residual stresses in as-spun fibers..	119

LIST OF ILLUSTRATIONS (Cont'd.)

FIGURE

4.6	Laser damaged as spun PBT fiber-optical micrograph.....	120
4.7	Residual stress structural model.....	121
4.8	Residual stress structural model with buckling of compressed elements.....	122
4.9	Surface of (a) as spun undeformed and (b) as spun deformed fibers.....	123
4.10	Mechanically peeled fibers (a) as spun undeformed (b) as spun deformed.....	124
4.11	Dependence of fiber stress on free annealing temperature....	125
4.12	Stress-temperature bounds for relief of residual stresses....	126
4.13	Loading conditions for fatigue testing.....	127
4.14	The distribution of the number of specimens as a function of lifetime in fatigue tests.....	128
4.15	Elastic component of twisting strain (γ_e) as a function of total strain (γ).....	129
4.16	Effect of twisting on longitudinal strength of PBT fibers....	130
4.17	SEM micrograph of fracture surface of PBT fiber in torsion-tension test.....	131
4.18	Effect of exposure to harsh environment on fiber modulus....	132
4.19	Effect of exposure to harsh environments on fiber strength...	133
4.20	Effect of exposure to harsh environments on fiber strain at break.....	134

LIST OF TABLES

TABLE	PAGE
2.1 Raman and Infrared Spectral Data for PBO Model Compounds (in cm^{-1}).....	18
2.2 Raman and Infrared Spectral Data for PBT Model Compounds (in cm^{-1}).....	21
3.1 Calculated and Observed Equatorial Structure Factors for PBT.....	57
3.2 Defect Analysis of Celanese Fibers PBT-27554-#.....	58
3.3 Orientation by Dichroism.....	59
3.4 Processing Histories & Mechanical Properties of Tapes.....	60
3.5 Dark Field Image Sizes for Various Fibers.....	61
4.1 Mechanical Properties of Selected Fibers.....	114

SECTION 1: OVERVIEW

The goal of this project is to determine for rigid rod polymer fibers and films the relationships between mechanical properties and sample microstructures and to use this knowledge to obtain the maximum in strength and modulus for these materials. The fibers and films of poly(p-phenylene benzobisthiazole) (PBT) which have been investigated were produced at Carnegie Mellon University (Professor G.C. Berry) and at Celanese Research Corporation (Dr. E.C. Chenevey) from liquid crystalline solutions using a dry-jet-wet spin process for fibers and either shear or extrusion for films.

This past year has seen a dramatic improvement in the mechanical properties of PBT. Heat treated fibers have been produced with a modulus of 2100 grams per denier (g/d) and a tenacity of 20 g/d. These properties place PBT in a prominent position with respect to other high performance materials. In addition to their high specific modulus and strength, the fibers' thermal and environmental stability is outstanding. Correlation of sample microstructure and resultant mechanical properties with processing conditions has been done to help optimize processing conditions.

Microstructural studies involve predominantly scanning and transmission electron microscopy, wide angle x-ray scattering and electron diffraction. Mechanical behavior has been assessed in uniaxial tensile, fatigue, bending and torsion. Tensile properties have been measured over the range -100°C to +200°C. Studies of low molecular weight model compounds and poly(p-phenylene benzobisoxazole) (PBO) and PBT polymers in solution and solid states have also been done by laser Raman and Fourier transform infrared spectroscopy.

During the past year the following publications have appeared:

1. W.W. Adams, L.V. Azaroff and A.K. Kulshreshtha, *Zeit. fur Krist.* 150, 321-326 (1979). "Xray Diffraction by a Nematic Polybenzothiazole Fiber."
2. E.J. Roche, T. Takahashi and E.L. Thomas, *Amer. Chem. Soc. Symposium, Fiber Diffraction Methods*, 141, 303 (1980), "Structure of High Modulus Fibers of Polyparaphenylene Benzobisthiazole."
3. S.R. Allen, A.G. Filippov, R.J. Farris and E.L. Thomas, *J. Appl. Poly. Sci.* 26, 291 (1981), "Macrostructure and Mechanical Behavior of Fibers of Polyparaphenylene Benzobisthiazole."

and the following papers have been submitted for publication:

4. G. Venkatesh and S.L. Hsu, *Macromolecules*, "Spectroscopic Study of Rigid Rod Polymers I: Structures of Model Compounds."
5. S.R. Allen, A.G. Filippov, R.J. Farris, E.L. Thomas, C.P. Wong, G.C. Berry and E.C. Chenevey, *Macromolecules*, "Mechanical Studies of High Strength, High Modulus Polyparaphenylene Benzobisthiazole Fibers."
6. G. Venkatesh and S.L. Hsu, *Macromolecules*, "Spectroscopic Studies of Rigid Rod Polymers II: Structures of Protonated Structures."

The general approach of the University of Massachusetts contract for microstructure-mechanical property relations has been along three lines. The following three areas summarize the three sections of this report:

1. Spectroscopic Studies (see Section 2: Dr. S.L. Hsu)
2. Morphological Studies (see Section 3: Dr. E.L. Thomas)
3. Mechanical Studies (see Section 4: Dr. R.J. Farris)

1.1 Spectroscopic Studies

Fourier Transform Infrared (FTIR) and Laser Raman investigations have

provided key data on solution and solid state polymer conformation. With the cooperation of Dr. Evers at Materials Laboratory, WPAFB the model compounds studies are leading to additional understanding of protonation and degradation effects. A collaborative study with Professor Berry is underway in order to elucidate the structures of protonated and solid polymers.

In the past year, our spectroscopic studies were directed towards a better understanding of the chain conformation and chain packing associated with these high modulus fibers. In the first area of study, as expected, we have evidence showing the polymers in solution exist in the protonated form. Model compounds have proven to be extremely helpful in this study, because they can be dissolved in non-protonic solvent such as chloroform, or in strong acid such as methane sulfonic acid (MSA) or chlorosulfonic acid (CSA). Quantitative assignments for the vibrations observed and their changes have elucidated the protonation effect for these polymers.

The source of information available to vibrational spectroscopy is band position, band intensity, band shape and dynamic measurements of their changes. Experimental studies, in conjunction with normal vibration calculations, should provide qualitative explanations of features sensitive to changes in the secondary structure of polymers. If properly assigned, band positions can be informative regarding chain rigidity and degree of chain extension. It should be emphasized that since spectroscopic measurements do not depend on the periodicity, these results complement the x-ray, neutron and electron diffraction studies in the contract.

1.2 Morphological Studies

The thrust of the morphological studies program for this past year has

focused on determining the molecular orientation and lateral ordering in the polymer using a variety of morphological techniques, notably, wide angle x-ray scattering, electron diffraction, high resolution lattice imaging and dark field electron microscopy and small angle neutron scattering. Additional morphological studies were directed at determining processing microstructure relations and the degree of residual stress and residual solvent retained in the fiber or film after processing and after additional heat treatment.

Employment of the detachment replication technique of fibers and films has been quite successful leading to high quality electron diffraction patterns and dark field images. Radiation damage lifetime assessment has indicated that PBT is more radiation resistant than poly(p-phenylene terephthalamide) (PPTA). The recent achievement of lattice images in PBT from the e_1 reflection bears this out and is moreover a significant development towards the detailed understanding of lateral ordering in rigid molecule systems.

While most of the materials produced to date have extremely high degrees of orientation, thus far, the key differences have been in the lateral ordering of the chains. Better lateral ordering has been observed in heat treated samples, and in particular, samples processed directly from the polymerization solvent, polyphosphoric acid (PPA). In order to realize high strength as well as high modulus, efficient chain-chain interaction, that is, good lateral packing of the chains, is necessary. Our latest electron diffraction, dark field and lattice imaging investigations show extremely high molecular orientation and very well developed lateral order for heat treated fiber and film, but no true 3-dimensional crystal formation. It remains to be seen if this feature is a direct consequence of the chemical structure of PBT molecules or is simply the

result of non-optimized processing and heat treatment conditions.

1.3 Mechanical Studies

The past year's investigation of the mechanical behavior of the rigid rod PBT fibers has been very productive. In our initial studies the surprisingly nonlinear behavior and apparent plasticity of the as-spun fibers and the modulus increase after plastic deformation caused considerable concern. The mechanism leading to these effects has now been identified. These effects are caused by microstructural element buckling due to residual stresses produced during the fiber formation process. This hypothesis has been experimentally confirmed by both mechanical tests and microscopic examination of the fibers. The model is consistent with the changes in properties observed with heat treatment and the voids and flaws observed in fibers. Although the ultimate fiber properties are still limited by defects, it appears that better fibers are being produced as knowledge about the spinning and coagulation process is gained. Hopefully, in the not to distant future, very high quality fibers can be produced which will enable us to determine the ultimate potential of these materials.

The mechanical properties section of the report also describes a model for heat treatment with tension, torsional effects on single filaments, and the influence of some harsh environments on fiber properties. Also discussed are the fatigue characteristics of both heat treated and as spun fibers. Much of our future work will be in the area of optimization of heat treatment conditions. During the past year a small heat treatment line was constructed which allows control of fiber tension, temperature, environment and residence time. This device has been tested and will be used heavily during the coming year.

SECTION 2: SPECTROSCOPY

2.1 Introduction

It is known from previous studies carried out in the first year, quite different spectra were obtained for poly(p-phenylene benzobisoxazole), PBO and poly(p-phenylene benzobisthiazole) PBT when dissolved in 100% sulfuric acid or methane sulfonic acid (MSA) or polyphosphoric acid (PPA) compared to the solid polymer. These differences occur both in the conformationally sensitive low frequency region (0-100 cm^{-1}) and in the medium frequency region between 1000 and 1600 cm^{-1} . Since these polymers are known to remain in the fully extended state even in very dilute solutions [1-3], and have also been postulated to exist in protonated forms in strong acids and with the addition of water form aggregates, the large spectroscopic differences observed between polymers in the solution and solid states are of great interest and need to be clarified.

Only a limited number of spectroscopic characterization studies on extended chain polymers exist in the literature [4,5]. In this past year we have given particular attention to the changes observed in order to elucidate the structures of PBO and PBT in both the solid state and the solution state.

Although PBO polymer is available only in the cis form and PBT polymer only in the trans form, model compounds are available in both the cis and trans conformations. In this report, PBO or PBT will refer only to the polymers, while c-PBO, t-PBO, c-PBT or t-PBT will be used to designate model compounds. The spectroscopic analysis of these model compounds serve as a useful basis to elucidate the structure of the polymers.

2.2 Experimental

Cis and trans forms of crystalline PBO and PBT model compounds were furnished by Dr. Al Fratini of the University of Dayton and Captain Wellman of the Materials Laboratory, Wright Patterson Air Force Base.

Infrared spectra ($4000-400\text{ cm}^{-1}$) were obtained with a Nicolet 7199 Fourier Transform Infrared Spectrometer. Data were usually taken in the form of KBr pellets containing 1% sample by weight. Three hundred scans at 2 cm^{-1} resolution were signal averaged to yield spectra of high signal to noise ratio. Representative spectra for c-PBO and t-PBT model compounds are shown on Figures 2.1 and 2.2 respectively.

Raman data were obtained with a Jobin-Yvon HG 2S Raman Spectrometer. The Raman Spectra were obtained using less than 15 mw of laser power in order to minimize the possibility of thermal degradation. Spectra of high signal to noise ratio were obtained for model compounds in the solid state as well as in solutions using excitations varying from 514.5 nm to 457.9 nm of an Argon ion laser. The Raman spectra obtained for all four model compounds in the solid state are shown in Figure 2.3. In all cases, intense peaks exist in the very low frequency region. Their positions and shapes are sensitive to temperature. Representative spectra obtained for t-PBO at room and low temperatures are shown in Figure 2.4.

Solution ultraviolet and visible absorption spectra were obtained with a Beckman Model Acta VI Spectrometer. Although the rigid-rod polymers are only soluble in strong acids, their model compounds are soluble in both non-protonic solvents such as CHCl_3 and strong acids. Representative spectra obtained in chloroform are shown in Figure 2.5.

2.3 Discussion

The vibrational spectra obtained for the model compounds differ significantly from one another in band position as well as in relative intensity. The Raman spectra generally are simpler than their corresponding infrared spectra. From Tables 2.1 and 2.2, except for the very low frequency region ($< 100 \text{ cm}^{-1}$) it can be seen there are few bands of significant intensity below 900 cm^{-1} in Raman. The reason for this selectivity is unclear at this moment. Not surprisingly, the electronic spectra of these conjugated heterocyclic model compounds all exhibit strong absorptions in the 300-400 nm region. In Raman spectroscopy, when the frequency for the incident laser excitation radiation is close to or coincident with the frequency of an electronic absorption band of the molecule, enhancement of the scattered intensity is expected. In addition, only the electronic transitions at or near the frequency of the laser excitation are resonance enhanced [6,7]. In these studies only preresonance enhancement were observed, since the shortest excitation wavelength used, 457.9 nm, is still nearly 100 nm from the absorption maxima. However, the scattered Raman intensity observed for polymers or oligomers in solution varied with the wavelength of the incident laser excitation.

In the regions where significant changes were observed, Raman bands of high intensity are likely assignable to the backbone, namely the central heterocyclic group, the outer phenyl ring and the C-C bond linking them. Furthermore, from x-ray diffraction studies [8], c-PBO has an orthorhombic space group ($Cmca$) while t-PBT has a monoclinic space group, $P2_1/c$. Since the trans compounds possess inversion symmetry, infrared and Raman data should be mutually

exclusive, as shown in Tables 2.1 and 2.2. For cis compounds no such symmetry restrictions exist, coincidence between infrared and Raman observations is therefore established.

Because of their use in structural analysis, the bands found in the 1200 and 1600 cm^{-1} regions were examined carefully. In these two regions, the Raman spectra of the model compounds differ significantly from one another in band position as well as in relative intensity. For example, the intense Raman bands observed at approximately 1276 and 1624 cm^{-1} are progressively shifted to lower frequencies in c-PBO, t-PBO, t-PBT and c-PBT. There is also a progressive reduction in intensity. The usually strong 1600 cm^{-1} frequency band is very weak, nearly absent in the Raman spectrum of c-PBT. The higher frequency band in the 1600 cm^{-1} region (c-PBO: 1624, t-PBO: 1614, t-PBT: 1602 cm^{-1}) is assigned to the ring stretching of the terminal phenyl ring and the lower frequency one in the 1200 cm^{-1} region to the C-C stretching of the carbons linking the main ring and the phenyl ring. Such assignments are consistent with the ones in biphenyl [9]. The Raman spectrum obtained for biphenyl in the liquid or solid state exhibits the ring stretching vibrations at 1612 and 1595 cm^{-1} . An intense polarized Raman band at 1285 cm^{-1} has been assigned to the C-C stretch of the carbon atoms linking the two rings [9].

For these model compounds, the intensity variation of the Raman active band found in the 1600 cm^{-1} region is particularly interesting. If this band is to be assigned to the ring stretching of the phenyl ring, its intensity should depend on the extent of conjugation between the rings of the backbone. Because of the different ionic radii associated with sulfur and oxygen, structural differences for PBO and PBT model compounds may arise from the rotation about the

single bond connecting the phenyl ring to the heterocyclic ring, thus affecting the electron delocalization of the molecule. The π electron sharing or conjugation is maximum when rings are coplanar [10]. When the rings are at right angles to one another, the π electron conjugation is completely interrupted. The investigations on sterically hindered biphenyls by Schmid and Brosa [11] show that there exists a quantitative relationship ($\cos^2\theta$ law) between the Raman intensity of the ring stretching vibration at about 1600 cm^{-1} and the angle of twist, θ . When the rings are coplanar as in fluorene, the Raman intensity has its largest value. When the rings are at large angles the resonance stabilization does not take place and the Raman lines will be weak, as in benzene [11].

X-ray results [8] and conformational energy calculations [12] have shown that the rings are planar in c-PBO and are at an angle of 23° or more, due to the steric hinderance between S and H of the phenyl ring, in t-PBT. Such structural differences should be evident in the Raman spectra obtained. Indeed, the band assignable to the ring stretching vibration is found to be most intense in c-PBO followed by t-PBO and t-PBT. This is consistent with the twist angles between the end phenyl ring and the heterocyclic group found for these three molecules [9,12,13]. In contrast, the near absence of this band in c-PBT suggests a low degree of conjugation. The preliminary x-ray diffraction results [13] of c-PBT suggest that the heterocycles on either side of the central benzene ring exist in a bow form, with the extremities of the heterocycles and phenyl rings being tilted out of the plane. This sort of complex situation may lead to a disruption of π -electron conjugation. This difference in structure of the model compounds is also evident in the electronic absorption spectra

obtained. For c-PBO dissolved in chloroform there are strong electronic absorption bands near 348, 333 and 320 nm. t-PBO and t-PBT show similar absorption curves with minor shifts in absorption maxima to longer wavelengths. In contrast, because of the low electron delocalization of this molecule, c-PBT shows significantly different spectral features in this region. Bands at 360, 344 and 335 nm are much weaker in c-PBT than their counterparts in t-PBT. Unlike others, the most intense band for c-PBT model compound is located below 300 nm.

The structural analysis based on the relative intensity of the 1600 cm^{-1} band is further supported by significant reduction in intensity for molecules in non-protonic solvents such as CHCl_3 . The Raman spectra of the model compounds in CHCl_3 are substantially similar to the solid state spectra. In the case of t-PBT, for which other structural studies have been carried out, the Raman band at 1602 cm^{-1} due to the ring stretching of the phenyl group is just visible as a weak band shown in Figure 2.6. This significant reduction in intensity of this band in solution suggests that the conjugation between the main ring and the phenyl ring in chloroform has decreased considerably, consistent with the prediction of the conformational energy calculations [12]. The angle predicted from calculations without taking into account intermolecular interactions is $\pm 60^\circ$, while the observed angle, from x-ray studies is $\pm 23^\circ$. It appears that the intermolecular interactions tend to keep the angle of twist low in the solid state. However, once the intermolecular interactions are minimized by dissolving in chloroform, the phenyl group is free to twist to higher angles, as required by the conformational energy. Similar mechanisms appear to be responsible for the observed reduction in intensity of the 1620 cm^{-1} band in t-PBO

when dissolved in chloroform. This is shown in Figure 2.7.

The isolated C=N stretching mode usually absorbs at approximately 1650 cm^{-1} . In conjugated molecules such as oxazole, thiazole, imidazole, benzoxazole, pyridine, etc., there is such a strong interaction between the C=N and C=C stretching vibrations that they completely lose their individual identity. As a result, a complex series of bands usually appears in the aromatic stretching region between $1600\text{-}1400\text{ cm}^{-1}$ [14-18]. Therefore, the Raman band at about $1602\text{-}1625\text{ cm}^{-1}$ as previously assigned to the ring stretching of the phenyl ring may contain contributions from other vibrations as well. The bands observed at 1550 cm^{-1} in the PBO model compounds and at 1505 cm^{-1} in the PBT model compounds can be assigned to be predominately the C=N stretching vibration. These assignments are based on the vibrational analysis of benzoxazole and benzothiazole [11]. The band observed at $1596\text{-}1604\text{ cm}^{-1}$ in the PBO model compounds and at $1593\text{-}1597\text{ cm}^{-1}$ in the PBT model compounds can be assigned to C=C stretching of the central ring. It is well known the ring stretching fundamental of benzene and related aromatic molecules is usually located around 1595 cm^{-1} . This band in the model compounds is unaffected by dissolution and protonation [20], an observation consistent with the results obtained from conformational energy calculations. In that study it was shown the inner ring is essentially unperturbed by the electronic redistribution due to protonation [12].

In addition to the loss of intermolecular interaction in solution, PBT, PBO and their model compounds may exist in a protonated form. The Raman spectra of these model compounds dissolved in H_2SO_4 are shown in Figure 2.8. These spectra are significantly different from the corresponding solid state spectra, especially in the case of c-PBO and t-PBO. The spectra in MSA are identical to the

spectra in H_2SO_4 . The electronic absorption spectra of these model compounds have indicated that such changes in the vibration spectra, especially in the Raman spectra, are to be expected. It has been observed in the case of pyridine that when it forms donor-acceptor complexes or forms hydrogen bonds to solvent molecules an increase in the frequencies of the C=C and C=N stretching vibrations is observed [18,21]. The increases in the ring stretching vibrations in the 1600 cm^{-1} region are maximum for the strong electron acceptors such as BCl_3 , moderate for the proton donors such as HCl and minimum for D_2O which forms relatively weak N...D0 bonds [21]. Filimoniv and Bystrov [21] tried to explain these increases in terms of a change in hybridization of the valence bonds formed by the nitrogen. In the case of c-PBO and t-PBO both nitrogen and oxygen may be protonated, while in the case of c-PBT and t-PBT it is mostly nitrogen.

Accordingly, one should expect much larger frequency shifts in the case of PBO compounds than in PBT compounds. This is in fact what is actually observed. The C=N stretching frequency shifts from 1550 cm^{-1} in the solid state to 1600 cm^{-1} in the acid spectra of c-PBO and t-PBO. In contrast, the C=N stretching mode is shifted from 1505 cm^{-1} in the solid state spectra to 1525 cm^{-1} in the acid spectra of c-PBT and t-PBT. The ring stretching band of the phenyl ring which is very intense in the solid state spectrum of c-PBO and moderately intense in the case of t-PBT is extremely weak in the acid spectra of all the model compounds. These observations suggest that in the protonated state the phenyl ring is twisted through a large angle in all the model compounds. The acid spectra of the trans PBO and PBT model compounds also show the presence of weak bands at 1641 and 1624 cm^{-1} respectively. The origin of these bands is not clear at the moment.

The Raman frequencies in the 1240 to 1315 cm^{-1} region in the solid state spectra of the model compounds usually exhibit two intense bands in the acid spectra. In the thiazoles they are located at 1295 and 1318 cm^{-1} . On the other hand, these bands are shifted to 1310 and 1340 cm^{-1} in the oxazoles. The significant differences in the intensity distribution between the c- and t-PBO model compounds are unclear at this moment. Another spectroscopic feature of the PBO protonated species is the upward shift associated with the breathing vibration of the heterocyclic ring. This band is observed at 928 cm^{-1} and 950 cm^{-1} in the solid state and acid, respectively. Similar changes have been observed in pyridine when it forms donor-acceptor complexes [18,21].

The following studies were carried out in order to understand more fully the process of protonation and its reversibility with concentration. Trifluoracetic acid, a highly protonating solvent, was added to chloroform solutions of the model compounds. The concentration of the acid was varied from 0.01 to 20 weight percent. The electronic absorption and laser Raman spectra obtained suggest that complete protonation of PBT model compounds occurs at a lower concentration of acid (i.e., 0.6%) while the PBO compounds require much higher acid concentrations (i.e., in the range of 2%). These requirements of different acid concentrations to completely protonate the PBO and PBT model compounds can be explained by the different electronegativities of the heteroatoms of the backbone of the model compounds or polymers.

Two types of dilution experiments were carried out in order to examine the reversibility of the protonation process. In the first set of experiments the donor (CF_3COOH) - acceptor (PBO or PBT model compound) molar ratio was kept constant, and the starting solution was diluted with chloroform. In the second

set of experiments the solute concentration in the chloroform solution was kept constant, and the acid concentration was decreased by adding neutral solution in chloroform. The UV absorption and laser Raman measurements obtained for successive dilutions of the starting solution containing 1, 5 or 10% acid have shown that the process of protonation could be completely reversed. Some typical spectra for t-PBO are shown in Figure 2.9, which shows the changes in position and intensity of the Raman bands of t-PBO with increasing acid (CF_3COOH) concentration.

The analysis of the model compounds has led to a better understanding of the spectroscopic features associated with the structural changes of the PBT and PBO polymers. The Raman bands observed for PBT polymer in the solid state at 1481 and 1601 cm^{-1} are to be assigned primarily to the C=N and ring stretching mode of the heterocyclic group. The ring stretching mode of the phenyl ring in the polymer is of the same low intensity as seen in the PBT model compounds. This observation suggests that the phenyl ring is twisted out of the plane of the central heterocyclic ring. When dissolved in MSA, these bands are shifted to 1515 and 1610 cm^{-1} respectively, consistent with the expected changes observed in the model compounds. In the case of PBO polymer, the Raman bands observed at 1550, 1622 and 1637 cm^{-1} are respectively assigned to the C=N and C=C stretching of the heterocycle and the ring stretching of the terminal phenyl group. The intensity pattern of these bands is similar to that of the c-PBO model compound, suggesting that the phenyl group and the central ring are approximately coplanar in comparison to PBT. On protonation the band at 1550 cm^{-1} of the solid state is shifted to 1625 cm^{-1} , and the 1637 cm^{-1} band observed in the solid state disappears, as in the case of c-PBO model compound on protonation.

This observation suggests that the phenyl group in both the polymers has more or less free rotation in solution in agreement with the conclusions from the viscosity and light scattering studies.

2.4 Summary

The analysis of the electronic and vibrational spectra of the model compounds, in conjunction with x-ray and conformational energy calculations have clarified one aspect of these heterocyclic molecules, i.e. the electronic delocalization between the phenyl and the heterocyclic rings. The extent of the conjugation greatly affects the relative intensity of the Raman active ring stretching vibration in the 1600 cm^{-1} region. This difference in the electron delocalization is undoubtedly related to the different structures associated with the four model compounds. Our analysis suggests these structural differences are related to the twist angle between the phenyl ring and the heterocyclic group. This conclusion is supported by theoretical conformation analysis, and by x-ray diffraction. When dissolved in MSA or 100% H_2SO_4 , the ring stretching modes associated with the terminal phenyl ring are all extremely weak suggesting that the phenyl ring is twisted through large angles in all the model compounds. The smaller upward shift in the C=N stretching modes of the thiazoles, when protonated in contrast with the large changes seen in the PBO compounds suggests that in the PBO compounds both the nitrogen and oxygen are protonated. In the case of the model compounds, the protonation effect can be reversed by dilution or compensation of the acid group.

Though much simpler, the spectroscopic features associated with the structural changes of PBO and PBT polymers are similar to those observed for c-PBO

and t-PBT respectively, thus implying the need to study the model compounds. How these structural differences affect the processing conditions and the resulting mechanical properties should be clarified and are the subjects of the current research efforts.

TABLE 2.1

Raman and Infrared Spectral Data for PBO Model Compounds (in cm^{-1})

<u>Raman</u>	<u>c-PBO</u>	<u>Infrared</u>	<u>Raman</u>	<u>t-PBO</u>	<u>Infrared</u>
		3096 (w)			
		3080 (sh)			3083 (w)
		3060 (vvw)			3058 (vvw)
		3035 (sh)			3038 (vvw)
		3000 (sh)			3006 (vvw)
				1618.5 (sh)	
1624 (vvs)		1622 (s)	1614 (vs)		1609 (m)
1603.5 (vs)			1596.5 (s)		
1587 (w)		1586 (m)	1581.5 (w)		1585 (m)
1559 (vs)		1560 (vs)	1544.6 (vvs)		1561 (vs)
1491 (m)		1490 (vs)	1487 (vw)		1485 (s)
1451 (m)		1450 (vs)	1447 (m)		1451 (vs)
		1430 (vs)			1427 (vs)
		1395 (vw)			1396 (vw)
		1365 (vs)			1370 (s)
1334 (vvw)		1335 (vs)	1327.5 (w)		1324 (m)
1314 (s)		1316 (vw)	1311 (vs)		1305 (vw)
1302 (s)		1301 (w)	1297.5 (s)		
1275 (vs)		1275 (s)	1267 (vs)		1285 (s)

(vvs) very, very strong; (vs) very strong; (w) weak; (m) medium; (s) strong;
 (sh) shoulder; (vw) very weak; (vvw) very, very weak

TABLE 2.1 (continued)

<u>Raman</u>	<u>c-PBO</u>	<u>Infrared</u>	<u>Raman</u>	<u>t-PBO</u>	<u>Infrared</u>
1207 (vw)		1208 (s)		1222 (vw)	1211 (w)
1174 (vw)		1173 (vw)			1170 (vvw)
1159 (vs)		1159 (vvw)		1152 (vw)	1159 (vw)
		1140 (s)			
		1111 (s)		1120 (w)	1128 (vs)
		1071 (vw)			1072 (vw)
1052 (vvw)		1050 (vs)			1052 (vs)
1021 (vvw)		1020 (vs)			1021 (s)
1004 (m)			1001 (m)		
991 (vw)		990 (sh)			985 (sh)
		966 (vw)			961 (vw)
929 (s)		928 (vs)		928 (s)	929 (m)
		918 (s)			920 (s)
		862 (vs)			860 (vs)
		835 (s)			
817 (vw)		816 (s)			815 (m)
777 (w)		776 (vs)	*		775 (vs)
		749 (w)			728 (m)
714 (vvw)		706 (sh)		713 (w)	690 (vs)
697 (vvw)		696 (vs)		694.5 (w)	685 (vs)

(vvs) very, very strong; (vs) very strong; (w) weak; (m) medium; (s) strong;
 (sh) shoulder; (vw) very weak; (vvw) very, very weak

TABLE 2.1 (continued)

<u>Raman</u>	<u>c-PBO</u>	<u>Infrared</u>	<u>Raman</u>	<u>t-PBO</u>	<u>Infrared</u>
		695 (vs)			678 (sh)
		674 (s)			
	621 (vw)				
522 (vw)		520 (m)	529 (w)	518 (m)	
510 (m)			516 (w)		
		481 (m)		479 (m)	
		415 (s)		413 (m)	
		395 (sh)		394 (sh)	
224 (vvw)			219 (vvw)		
218 (vvw)					
211 (vvw)			206 (vvw)		
			116.5 (vvw)		
			111.5 (vvw)		
79 (sh)			89.3 (m)		
70 (m,b)			73.6 (s)		
			37.1 (m)		
			26.5 (m)		
17.0 (vs)					

(vvs) very,very strong; (vs) very strong; (w) weak; (m) medium; (s) strong; (sh) shoulder; (vw) very weak; (vvw) very, very weak; (m,b) medium intensity, broad width

TABLE 2.2

Raman and Infrared Spectral Data for PBT Model Compounds (in cm^{-1})

<u>t-PBT</u>		<u>c-PBT</u>	
<u>Raman</u>	<u>Infrared</u>	<u>Raman</u>	<u>Infrared</u>
	3080 (vvw)		3076 (sh)
	3060 (vw)		3058 (vvw)
	3020 (vvw)		3021 (vvw)
	3000 (sh)		3000 (sh)
	1671 (m)		
1602 (s)	1611 (vvw)		
1593 (vs)		1596.7 (vs)	
1517.5 (vw)		1520 (m)	
1508 (w,sh)			
1503 (vvs)	1519 (s)	1510 (vvs)	1510 (s)
1474 (vs)	1486 (vs)	1482 (s)	1482 (vs)
1462 (vvw)			
1440 (vs)	1448 (vs)	1443 (m)	1440 (m)
	1426 (m)	1420 (m)	
	1401 (s)		1401 (w)
1310.5 (w)	1318 (s)	1316.5 (vvw)	1314 (vw)
1295.5 (w)	1306 (m)	1296.5 (vw)	1305 (vw)
1279 (s)		1276 (m)	1273 (m)
		1245 (sh)	

(vvs) very,very strong; (vs) very strong; (w) weak; (m) medium; (s) strong;
 (sh) shoulder; (vw) very weak; (vvw) very, very weak

TABLE 2.2 (continued)

<u>t-PBT</u>		<u>c-PBT</u>	
<u>Raman</u>	<u>Infrared</u>	<u>Raman</u>	<u>Infrared</u>
1245 (s)	1250 (s)	1240 (m)	1235 (s)
1228 (m)	1219 (w)		
1203 (s)			
1183 (vw)		1183 (vw)	
1163.4 (vvw)	1165 (w)		1148 (m)
	1100 (w)	1110 (m)	1100 (vvw)
	1072 (m)		1069 (m)
	1056 (w)		
1019 (vw)	1019 (m)		1024 (m)
999 (m)	1001 (w)	999.5 (m)	1000 (vvw)
	965 (sh)		
	958 (vs)		958 (vs)
	915 (m)		912 (m)
	876 (vs)		890 (s)
	869 (vs)		858 (vs)
	843 (m)	791 (vvw)	790 (vvw)
749 (w)	759 (vs)		763 (s,sh)
			756 (vs)
683 (w)	699 (s)	711 (vw)	712 (vvw)
	689 (sh)		704 (m)

(vvs) very,very strong; (vs) very strong; (w) weak; (m) medium; (s) strong; (sh) shoulder; (vw) very weak; (vvw) very, very weak

TABLE 2.2 (continued)

<u>t-PBT</u>			
<u>Raman</u>	<u>Infrared</u>	<u>Raman</u>	<u>Infrared</u>
	681 (vs)		685 (vs)
	665 (m)		670 (sh)
618 (vvw)	601 (s)		610 (s)
	468 (w)		480 (w)
	416 (s)		419 (m)
	395 (w)		394 (w)
337 (vvw)			117 (w)
207 (vvw)			
		101.5 (vw)	
98 (vw)		82 (vvw)	
86 (vw)		78 (vvw)	
78.5 (vw)		36.4 (m)	
35 (s)		23.4 (s)	
32 (s)		17 (w)	

(vvs) very,very strong; (vs) very strong; (w) weak; (m) medium; (s) strong;
 (sh) shoulder; (vw) very weak; (vvw) very, very weak

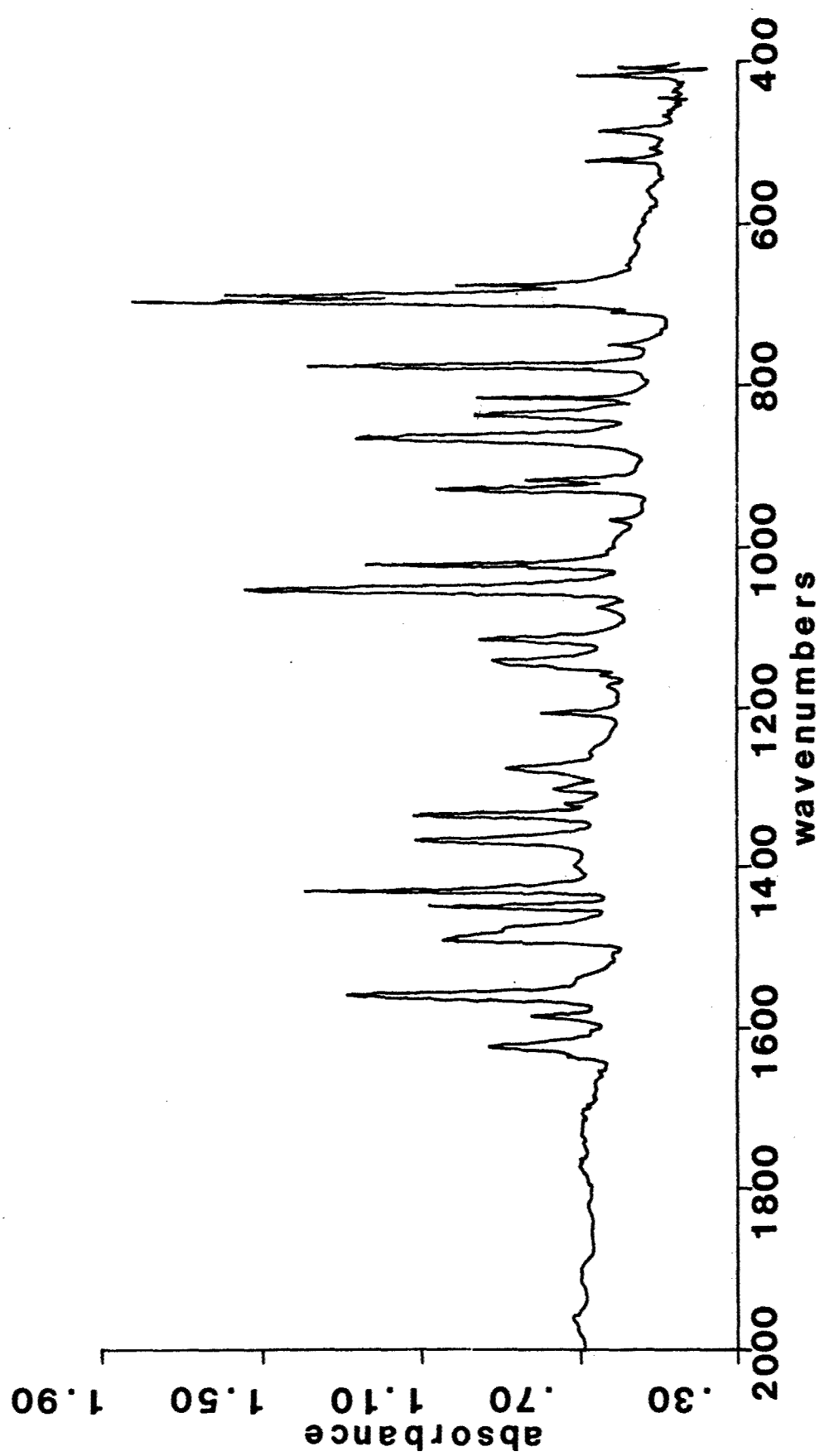


Figure 2.1: Infrared spectrum of c-PBO model compounds in KBr.
Concentration 1% by weight.

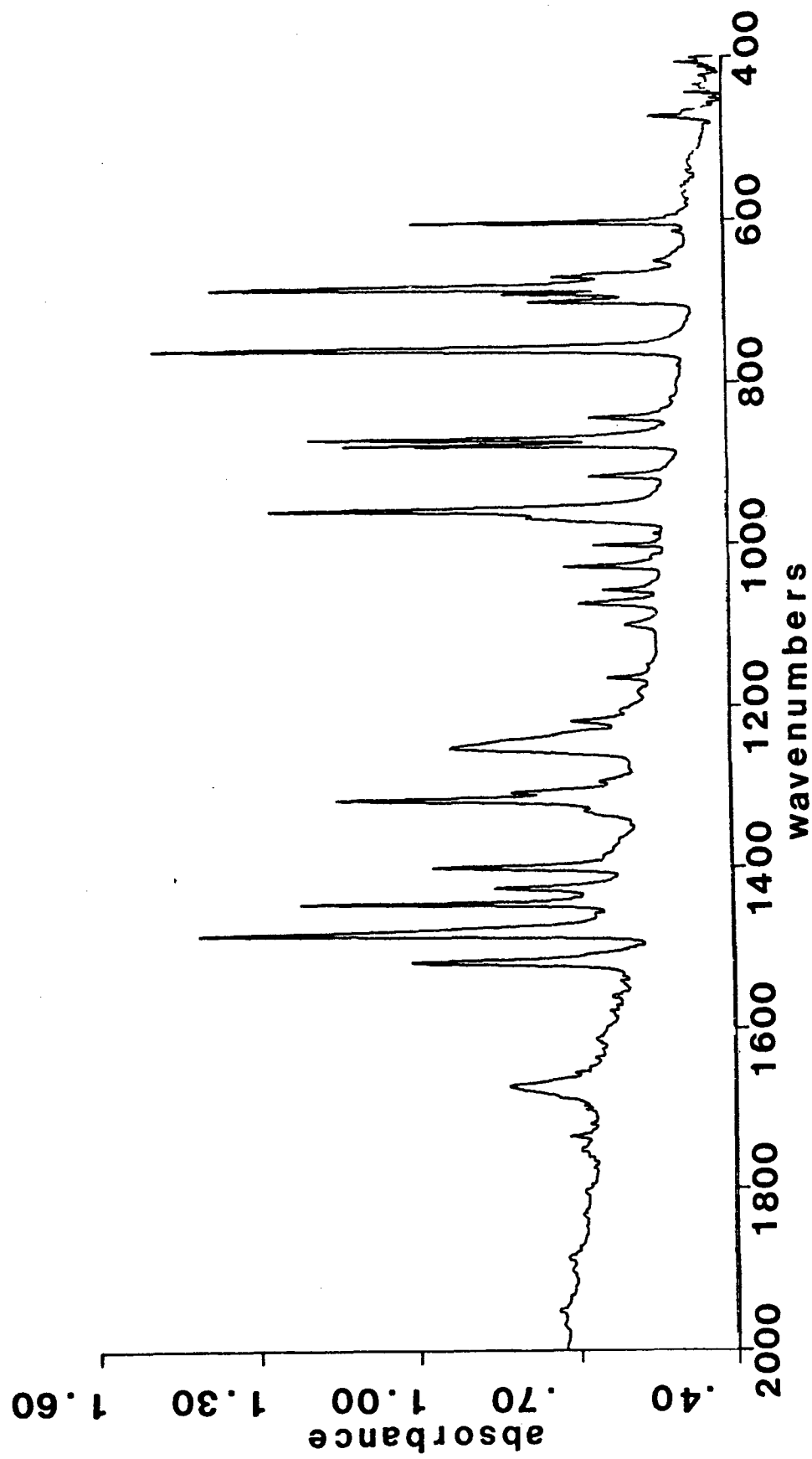


Figure 2.2: Infrared spectrum of t-PBT model compounds in KBr.
Concentration 1% by weight.

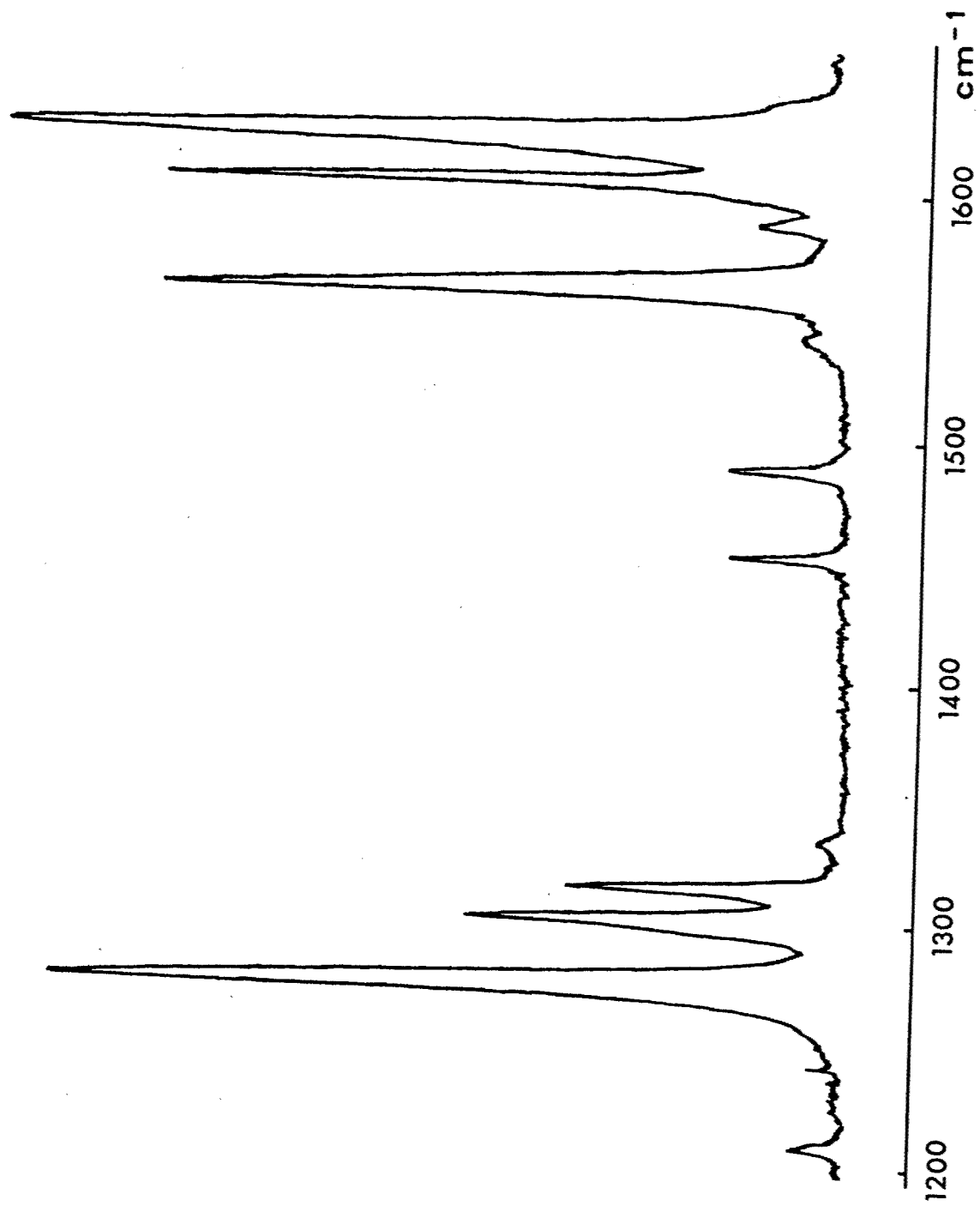


Figure 2.3: (a) Raman spectra of model compounds in the solid state: C-PBO
Laser excitation: 15mW at 514.5 nm. Bandpass: 0.7 cm^{-1} at 510.0 nm.

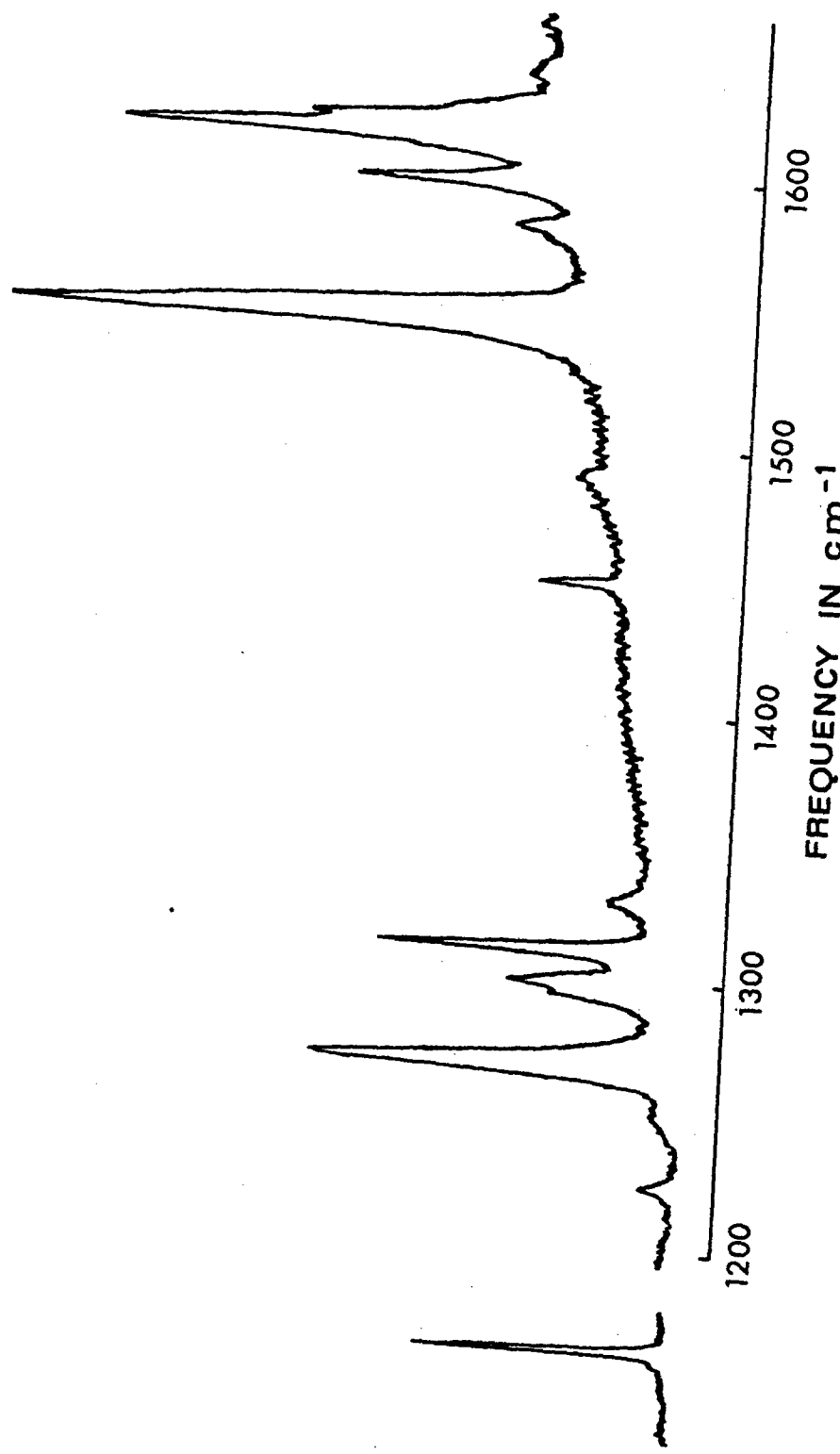


Figure 2.3: (b) Raman spectra of model compounds in the solid state: t-PBO
Laser excitation: 15mW at 514.5 nm. Bandpass: 0.7 cm^{-1} at 510.0 nm.

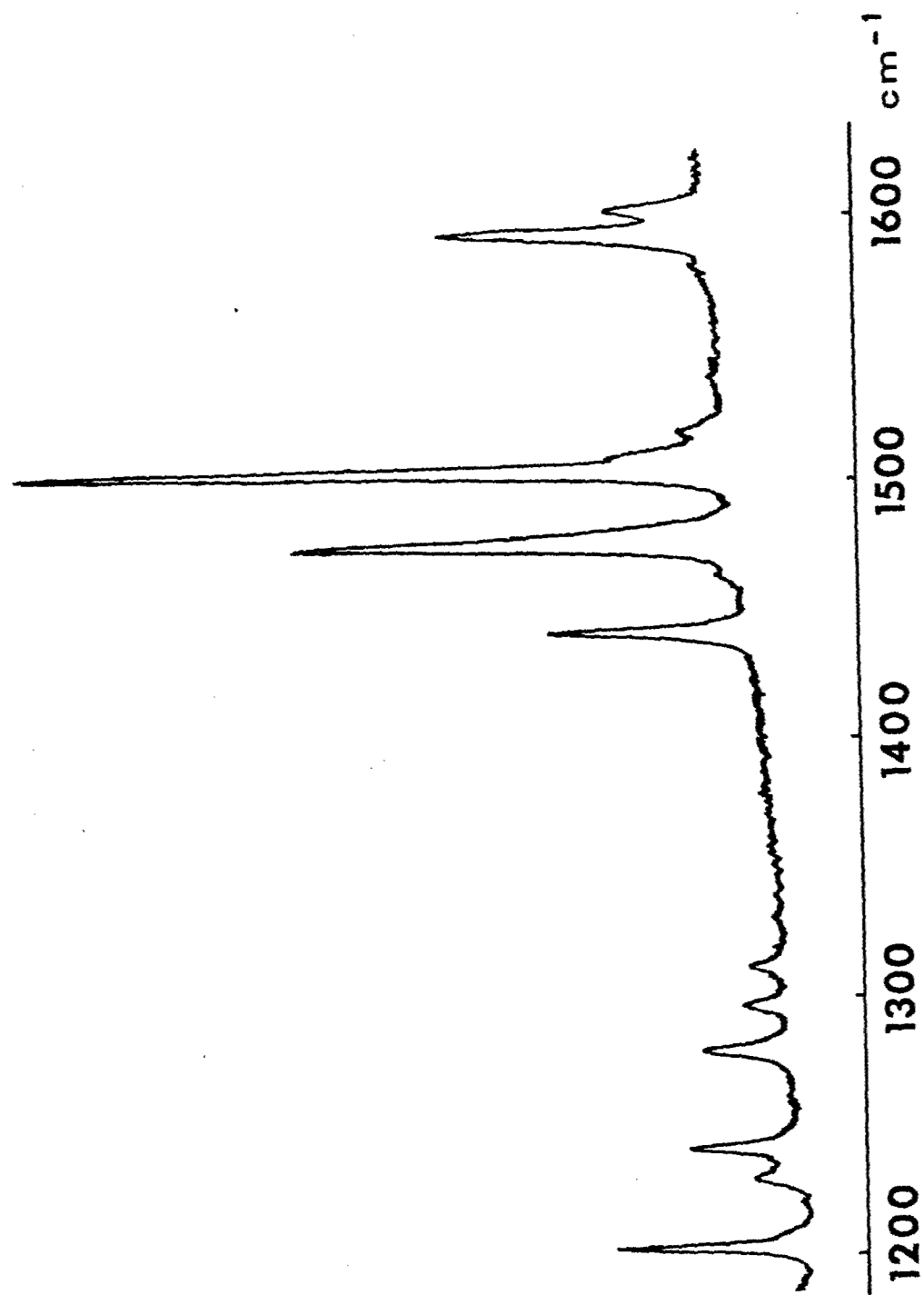


Figure 2.3: (c) Raman spectra of model compounds in the solid state of t-PBT
Laser excitation: 15 mW at 514.5 nm. Bandpass: 0.7 cm^{-1} at 510.0 nm.

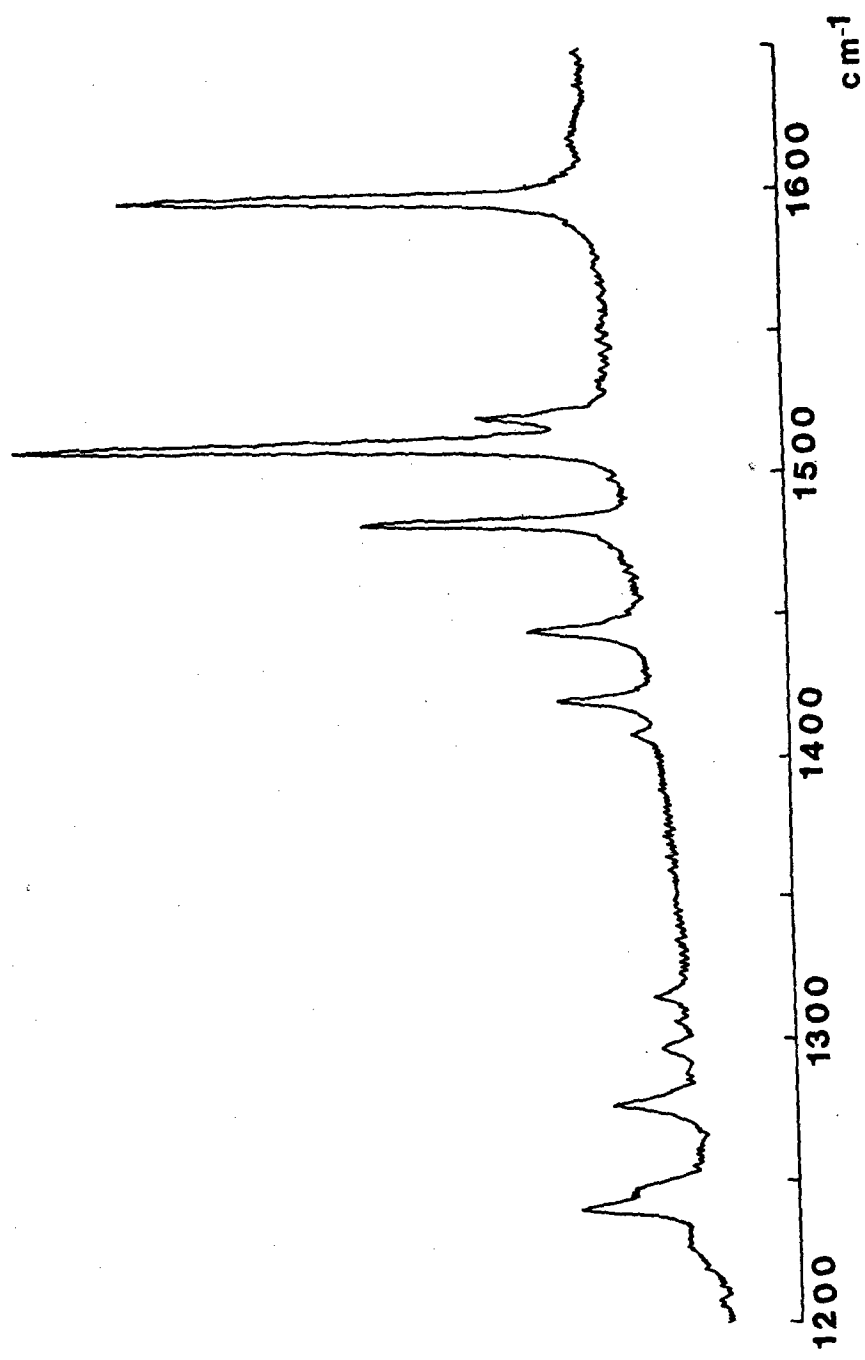
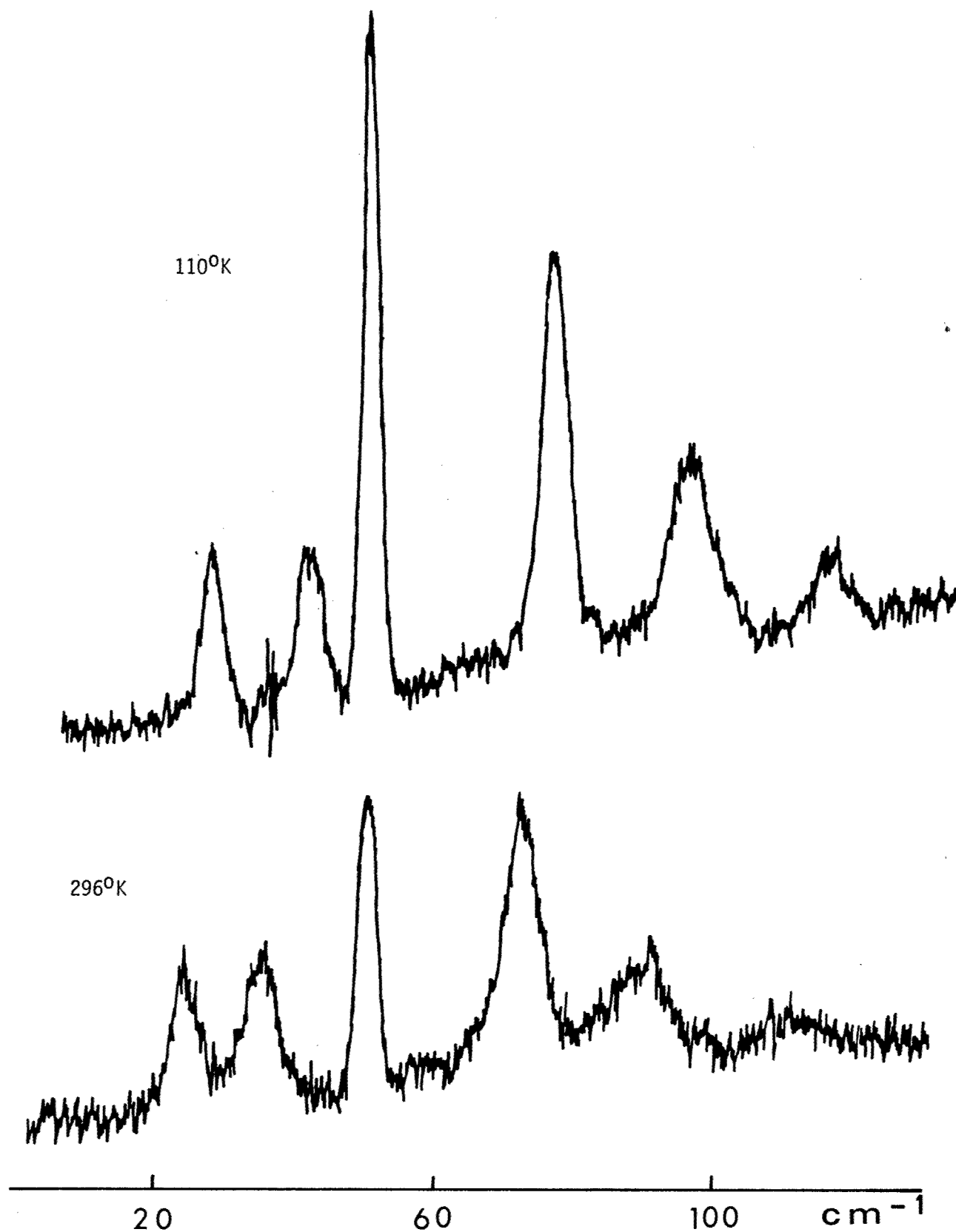


Figure 2.3: (d) Raman spectra of model compounds in the solid state; c-PBT. Laser excitation: 15 mW at 514.5 nm. Bandpass: 0.7 cm^{-1} at 510.0 nm.



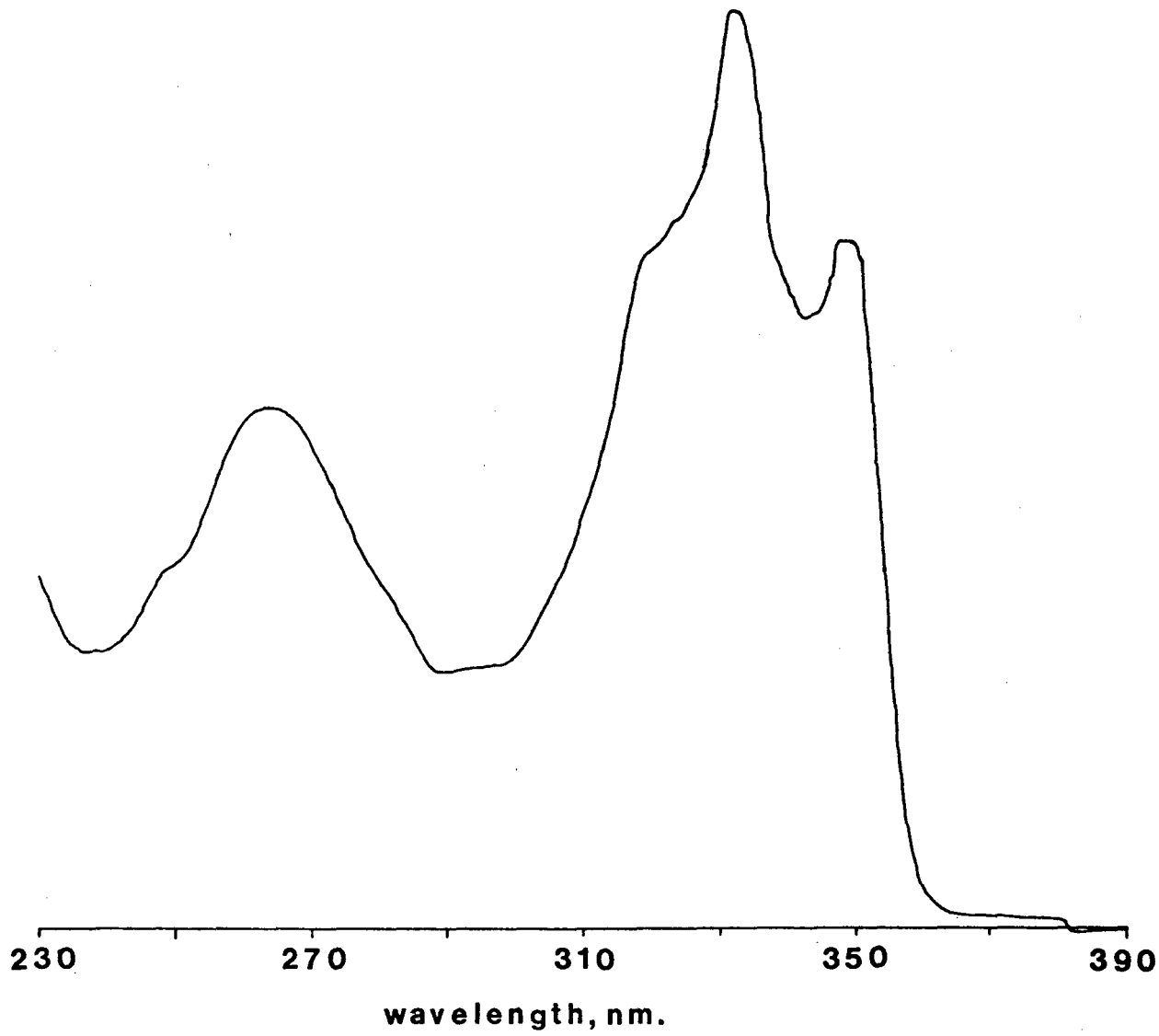


Figure 2.5: (a) Ultraviolet absorption spectra of the model compounds in CHCl_3 : c-PBO (Concentration 1% by weight)

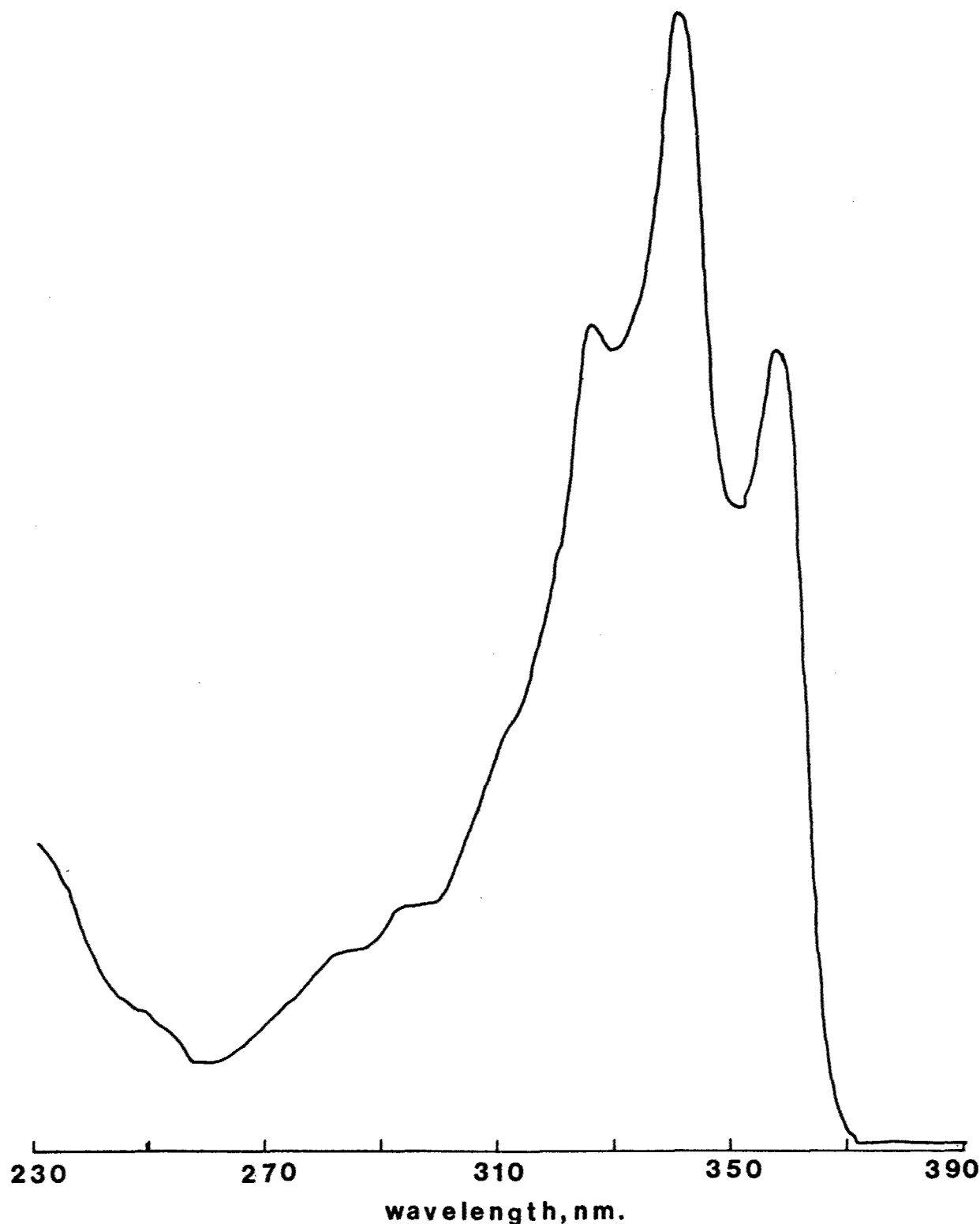


Figure 2.5: (b) Ultraviolet absorption spectra of the model compounds in CHCl_3 : t-PBO (Concentration 1% by weight)

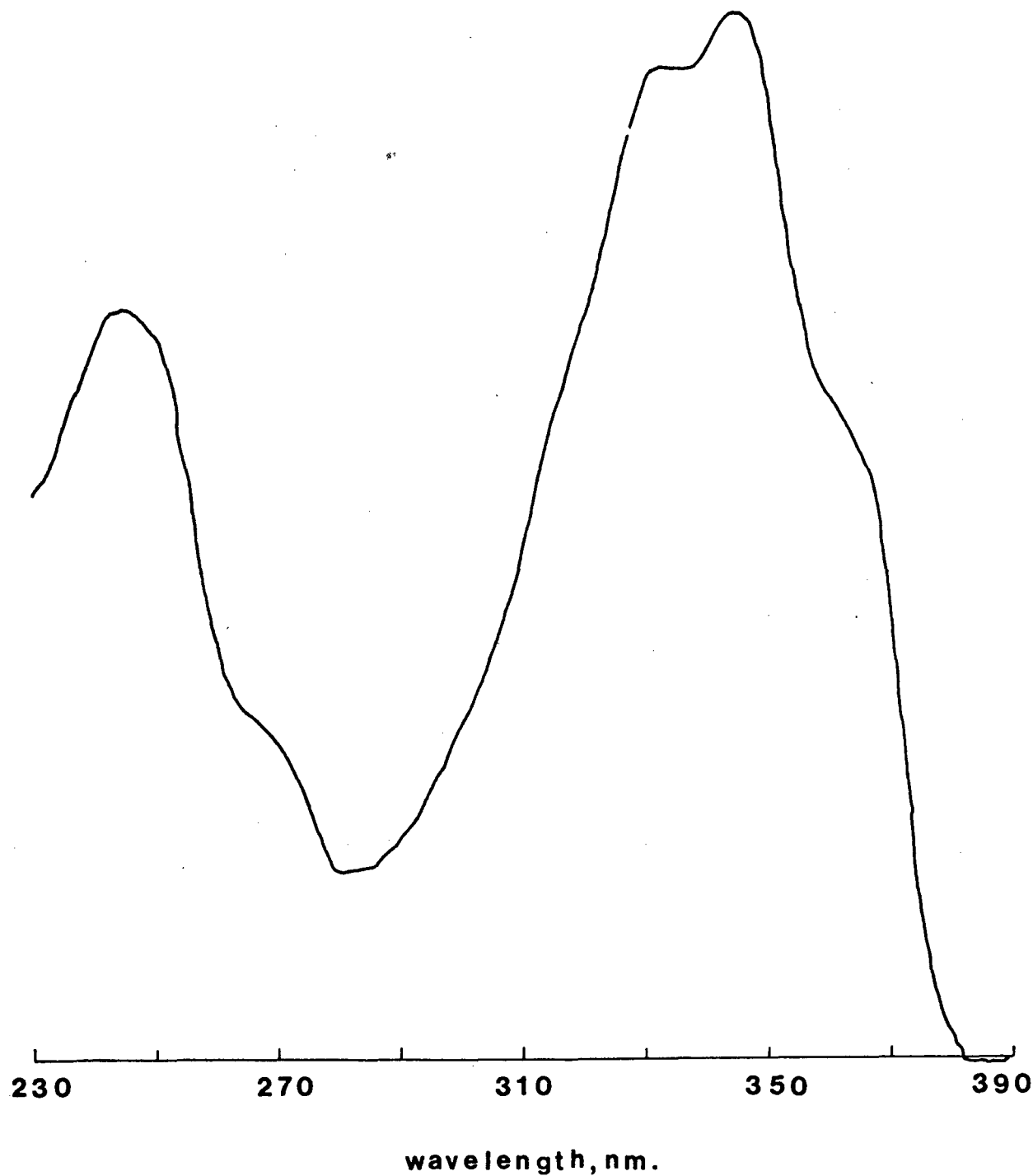


Figure 2.5: (c) Ultraviolet absorption spectra of the model compounds in CHCl_3 : t-PBT
(Concentration 1% by weight)

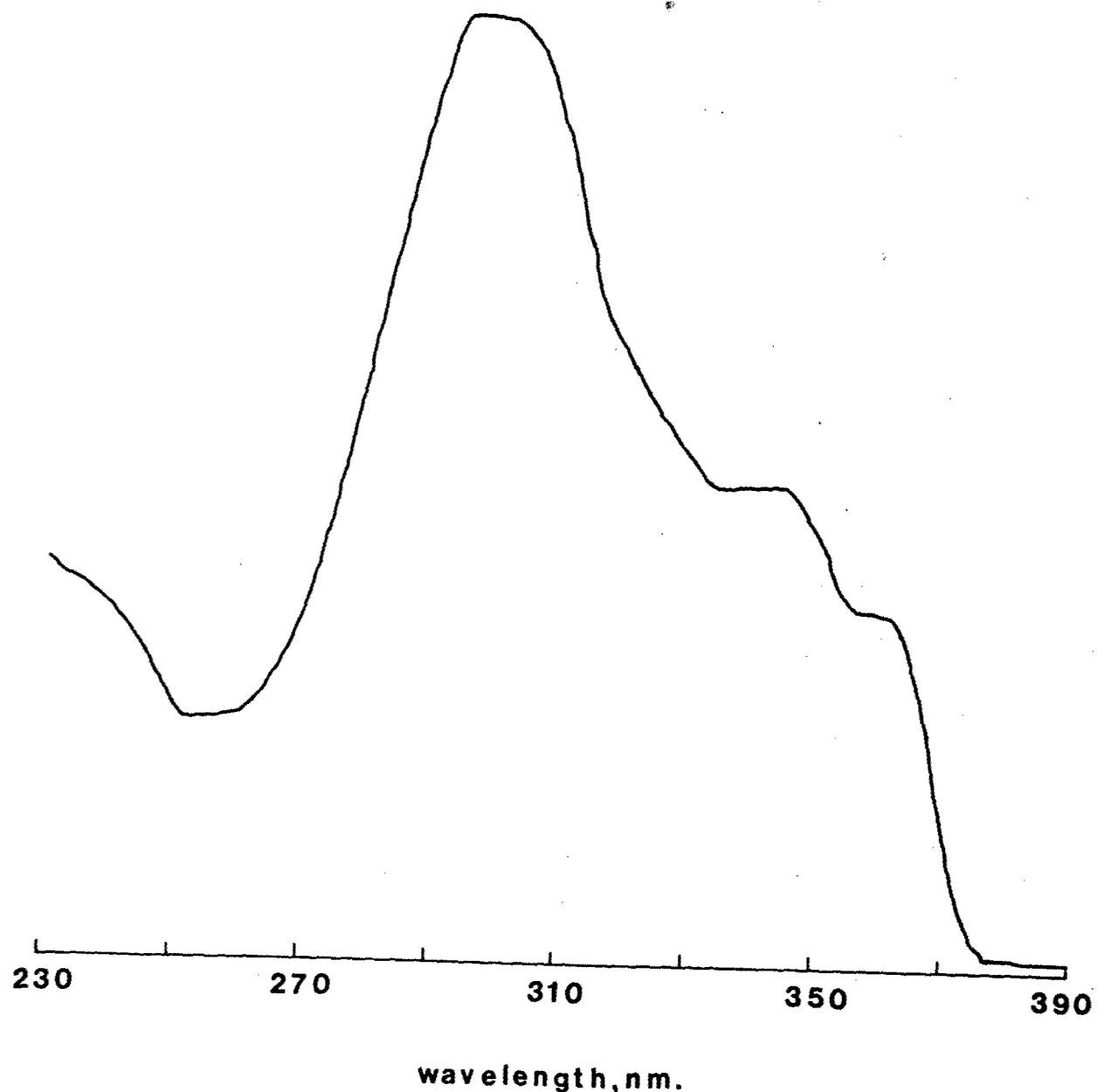


Figure 2.5: (d) Ultraviolet absorption spectra of the model compounds in CHCl_3 ; c-PBT (Concentration 1% by weight)

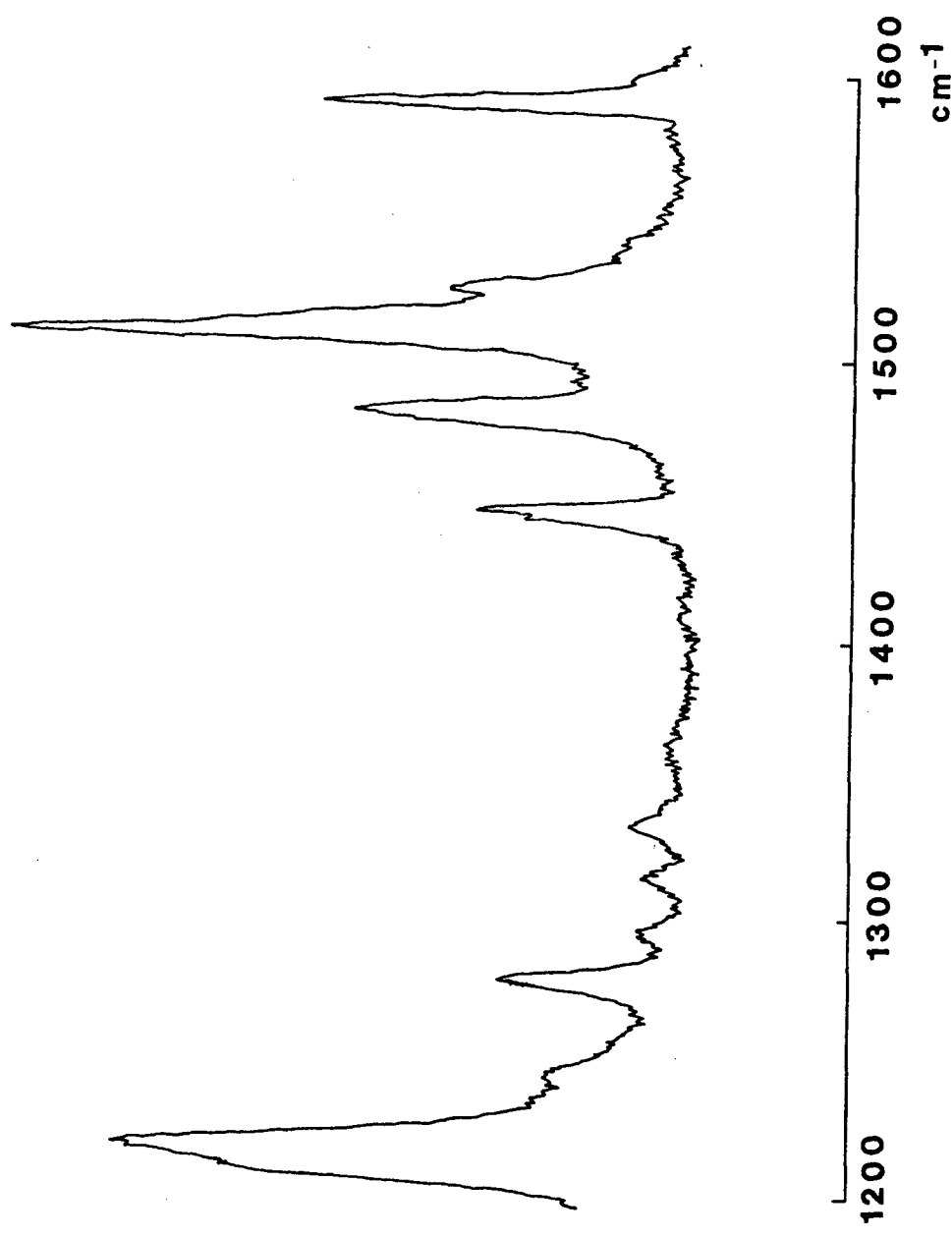


Figure 2.6: Raman spectrum of t-PBT in CHCl_3 . Laser power: 15 mW at 514.5 nm. Bandpass: 1.0 cm^{-1} at 510.0 nm. Concentration is 1% by weight.

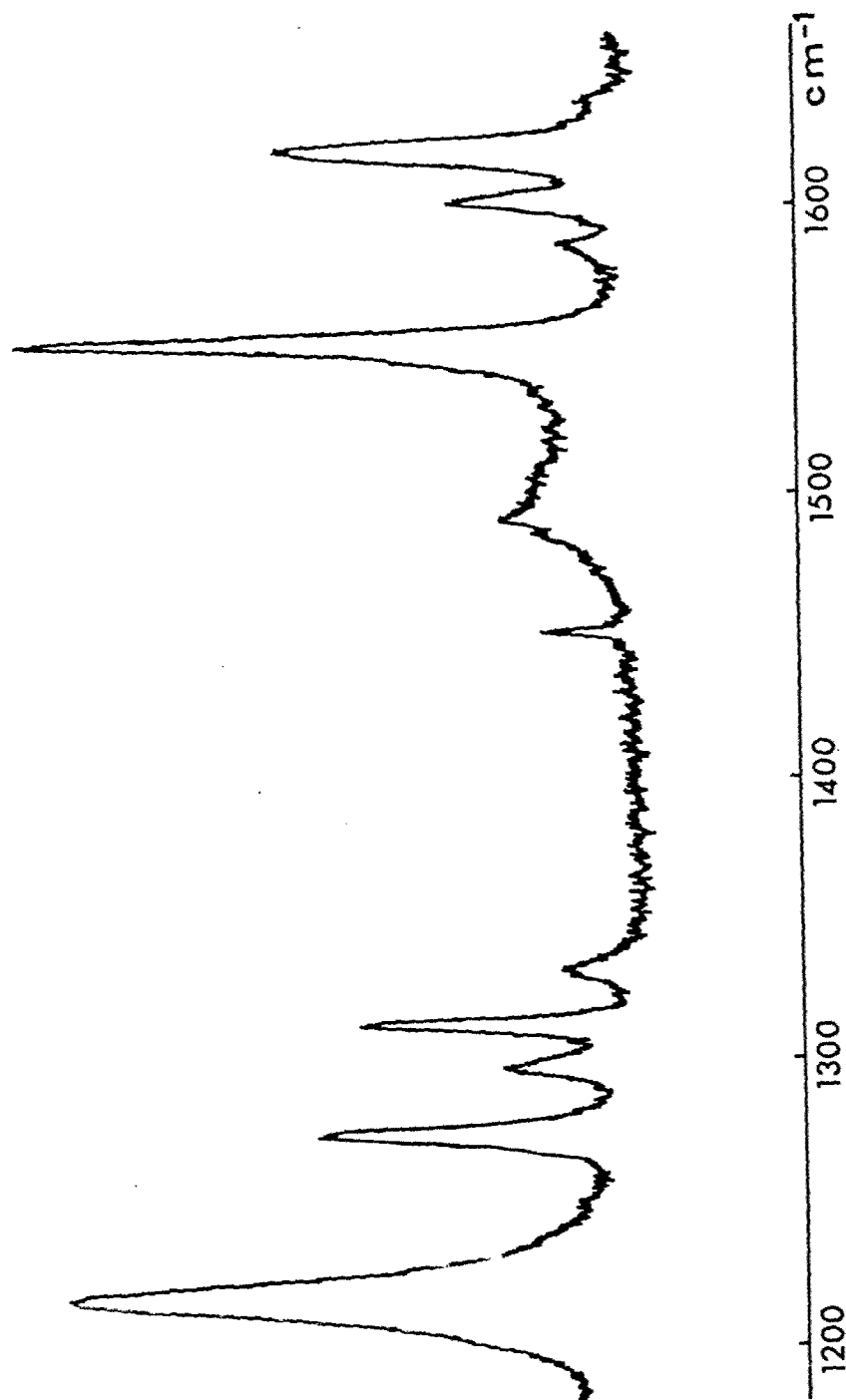


Figure 2.7: Raman spectrum of t-PBO in CHCl_3 . Laser power: 15 mW at 514.5 nm. Bandpass: 1.0 cm^{-1} at 510.0 nm. Concentration is 0.8% by weight.

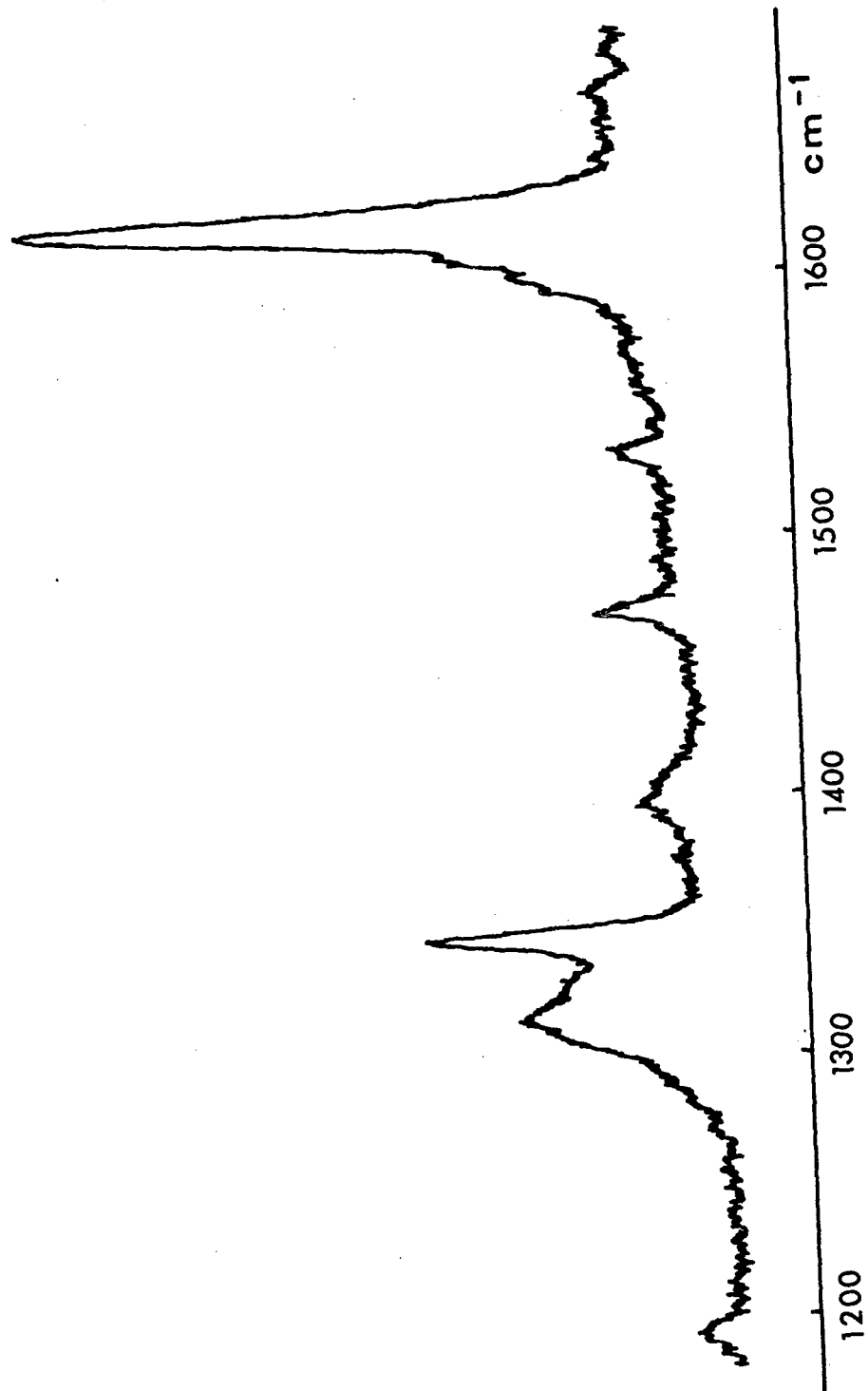


Figure 2.8: (a) Raman spectra of the model compounds in 100% H_2SO_4 : c-PBO.
Laser excitation: 15 mW at 514.5 nm. Bandpass: 1.0 cm^{-1} at 510.0 nm.
Concentration: 1% by weight.

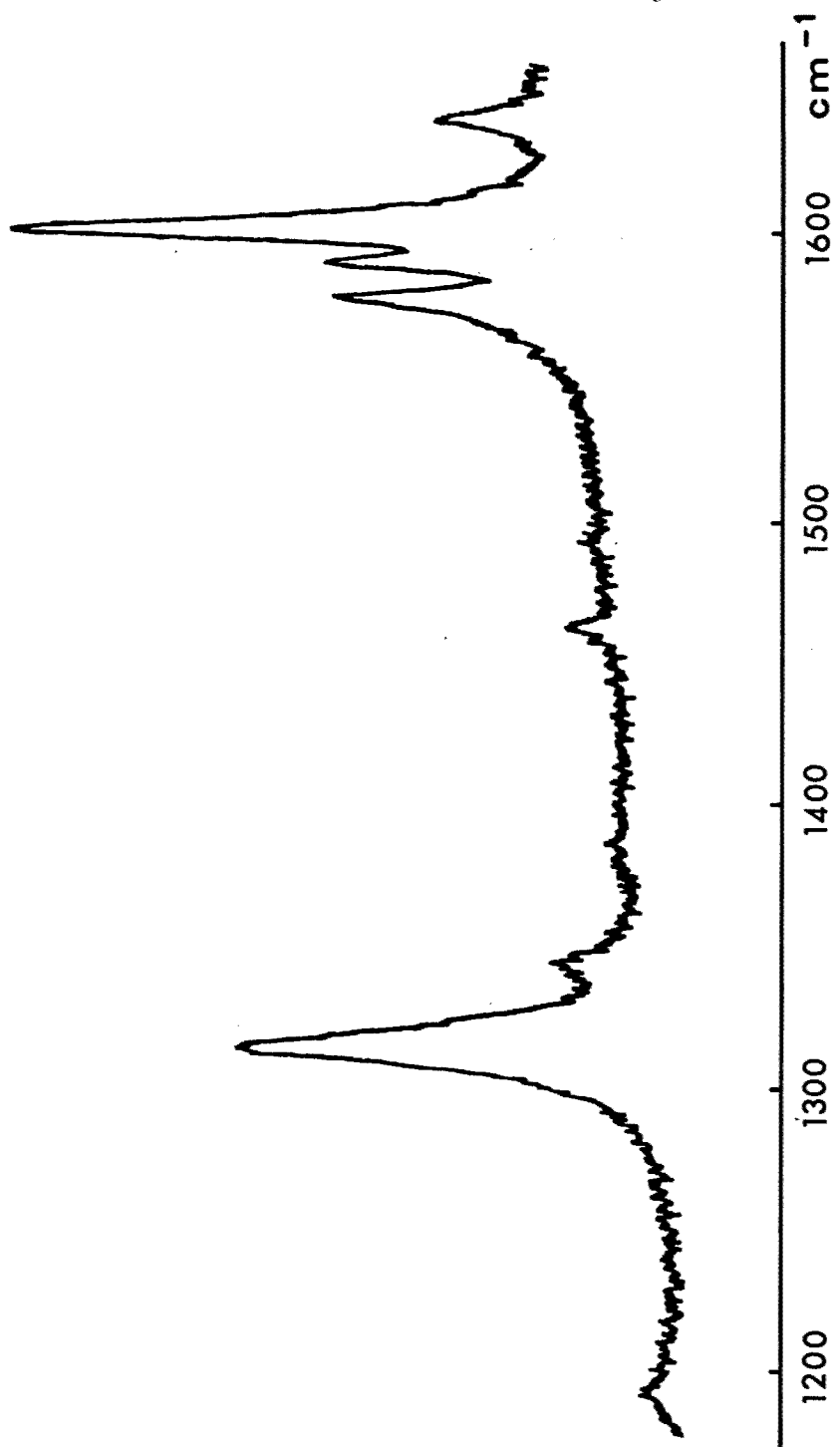


Figure 2.8: (b) Raman spectra of the model compounds in 100% H_2SO_4 : t-PBO.
Laser excitation: 15 mw at 514.5 nm. Bandpass: 1.20 cm^{-1} at 510.0 nm.
Concentration: 1% by weight.

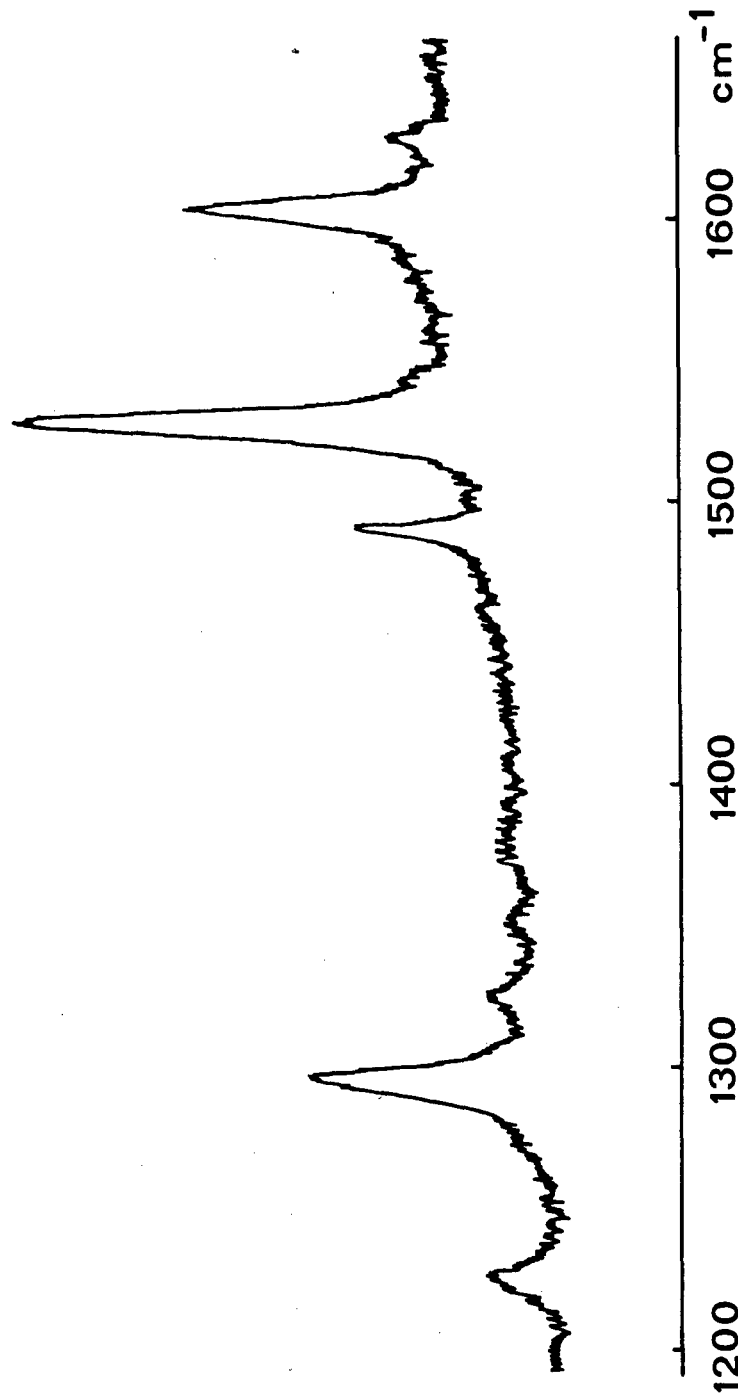


Figure 2.8: (c) Raman spectra of the model compounds in 100% H_2SO_4 : t-PBT.
Laser excitation: 15 mw at 514.5 nm. Bandpass: 1.0 cm^{-1} at 510.0 nm.
Concentration: 1% by weight.

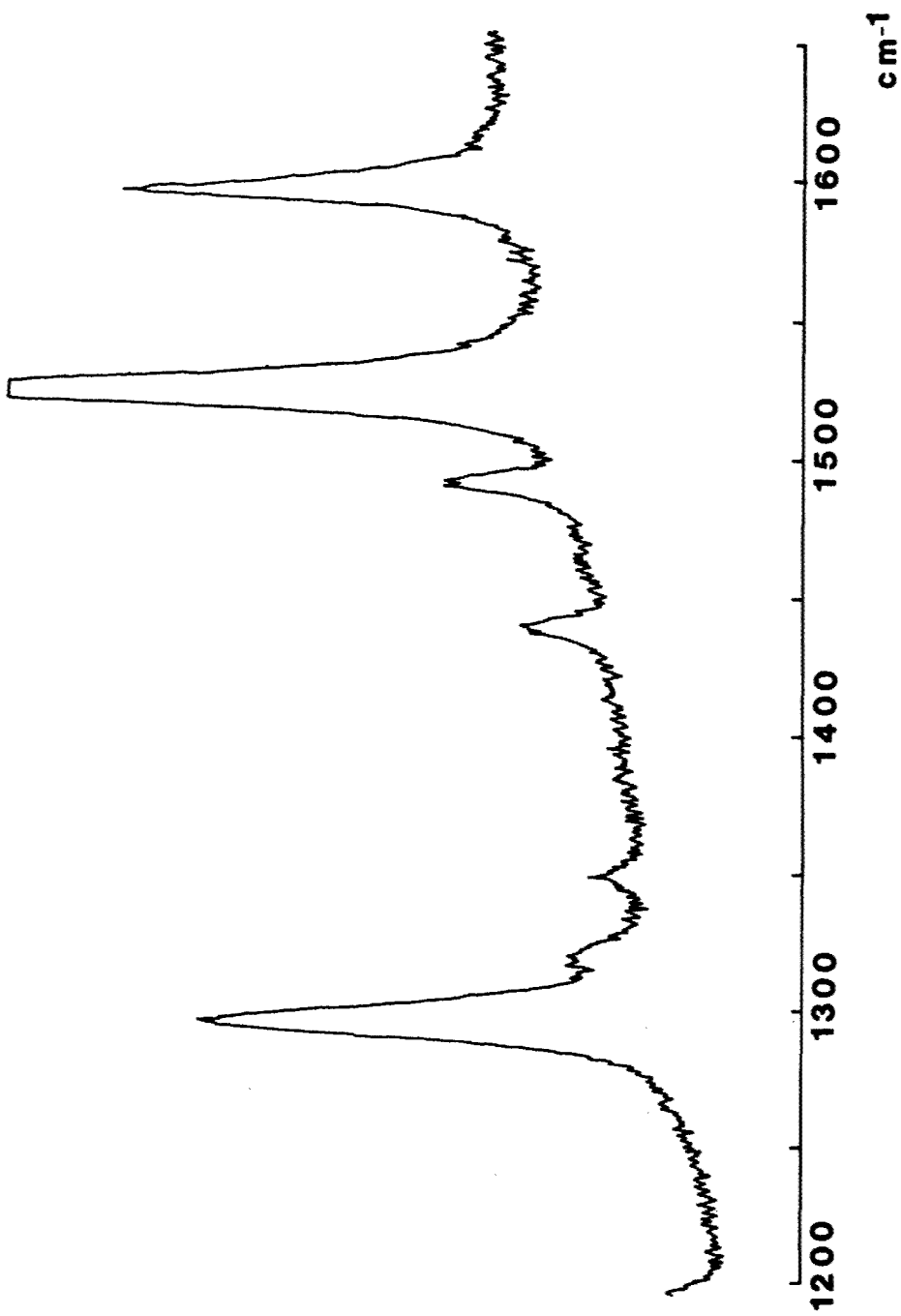


Figure 2.8: (d) Raman spectra of the model compounds in 100% H_2SO_4 : c-PBT.
Laser excitation: 15 mw at 514.5 nm. Bandpass: 1.0 cm^{-1} at 510.0 nm.
Concentration: 1% by weight.

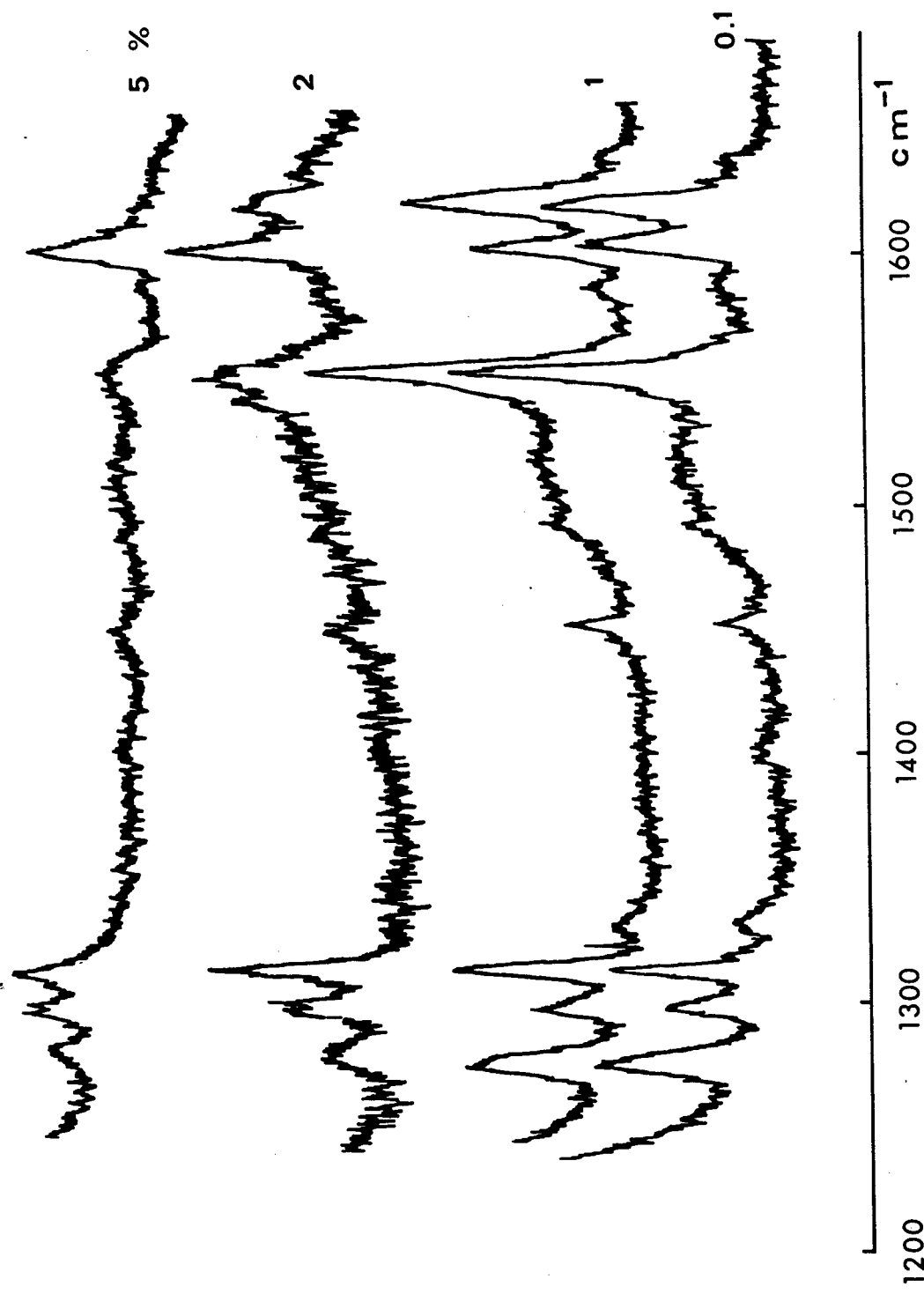


Figure 2.9: Effect of increasing acid concentration on the Raman spectrum to t-PBO in CHCl₃. Acid concentration is shown on the figure.

SECTION 3: MORPHOLOGICAL INVESTIGATIONS

In this section we report results of microscopical and scattering investigations of the microstructure of solutions, fibers and ribbons of poly(p-phenylene benzobisthiazole) (PBT). The following topics are treated: a discussion of the structure of PBT; light optical microscopy of solutions, fibers and tapes; secondary electron imaging (SEI) and x-ray microanalysis of tapes; transmission electron microscopy (TEM) of fragments from fibers and tapes; small angle x-ray scattering (SAXS) from fibers and tapes; and small angle neutron scattering (SANS) from solutions and tapes.

3.1 The structure of PBT

Understanding of the deformation behavior of a material requires a detailed understanding of the structure of the material. Adams et al [22] studied some of the earliest fibers produced at Carnegie Mellon and interpreted wide angle x-ray and electron diffraction patterns in terms of a model consisting of parallel periodic cylinders packed in a hexagonal array. This model was based on diffraction patterns consisting of up to 20 diffuse meridional layer lines and two rather broad equatorial maxima. Roche et al. [23] studied as-spun fibers produced at Celanese at higher spin draw ratios which had somewhat improved mechanical properties. Electron diffraction patterns from these fibers exhibited approximately the same 20 diffuse meridional layer lines and moreover, contained seven resolvable equatorial reflections. From these patterns a monoclinic net of chains with random translational stagger along the chain axis was proposed. Two possible unit cells were suggested:

<u>Unit Cell I</u>		<u>Unit Cell II</u>	
$a = 5.83 \text{ \AA}$	$\gamma = 96^\circ$	$a = 7.10 \text{ \AA}$	$\gamma = 63^\circ$
$b = 3.54 \text{ \AA}$	$Z = 1$	$b = 6.65 \text{ \AA}$	$Z = 2$
$c = 12.4$		$c = 12.4$	

Unit Cell I corresponds to the very simple arrangement of parallel sheets shown in Figure 3.1.

More recently, fibers and ribbons annealed at 475°C under load have become available. Electron diffraction patterns now exhibit ten resolved reflections along the equator. The meridional layer lines still consist of diffuse streaks. The latest patterns yield a slightly longer fiber repeat distance, $12.45 \pm 0.05 \text{ \AA}$. A refinement of unit cell I, is given below:

Unit Cell IA

$a = 5.97 \text{ \AA}$	$\gamma = 95.2^\circ$
$b = 3.62 \text{ \AA}$	$Z = 1$
$c = 12.45 \text{ \AA}$	$\rho = 1.65 \text{ gm/cm}^3$

Preliminary analysis of the intensities of the equatorial reflections predicts a setting angle ϕ , between the a axis and the phenyl ring of about 35° and an angle, α , between the a axis and the bisthiazole moiety of -5° (see Figure 3.2a). For these values, the calculated R factor is 0.096. R is defined as:

$$R = \frac{\sum |f_C - f_0|}{\sum f_0}$$

where f_0 and f_C are the observed and calculated structure factors, respectively. The observed and calculated structure factors for the equatorial reflections are given in Table 3.1.

Atkins [24] examined the cylindrically averaged Fourier transform of a single repeat unit in planar conformation based on the bond angles and distances obtained by Wellman [33] for the model compound (Figure 3.3). When 10 such units are joined together to form a single chain, discrete layer lines are obtained in the Fourier transform (Figure 3.4). The second and seventh layer lines are very weak. As noted by Atkins, a comparison of the molecular transform with the electron diffraction patterns from as-spun and heat treated fiber shows remarkable agreement with observed relative intensities of the layer lines (see Figure 3.5).

Atkins [24] also proposed two unit cells based on the equatorial reflections:

Atkins I		Atkins II	
$a = 6.55 \text{ \AA}$	$\gamma = 63.62^\circ$	$a = 11.96 \text{ \AA}$	$\gamma = 79.1^\circ$
$b = 3.56 \text{ \AA}$	$Z = 1$	$b = 3.56 \text{ \AA}$	$Z = 1$
$c = 12.35 \text{ \AA}$	$\rho = 1.71 \text{ g/cm}^3$	$c = 12.35 \text{ \AA}$	$\rho = 1.71 \text{ g/cm}^3$

As can be seen from Figure 3.1c, these cells are simply different versions of Roche's cell I. As proposed by Adams [22] and Roche [23], the molecular arrangement of Atkins is also a 2-dimensional net with translational freedom of the chains along the fiber axis and not a three dimensional lattice. This view is further supported by equatorial lattice images and the lack of coherently diffracting regions in the meridional dark field image, discussed in Section 3.4.

In summary, three dimensional crystalline order has not yet been achieved in PBT ribbons or fibers. Current samples consist of coherently scattering regions with molecules laterally well packed in a two dimensional net with

irregular translations of chains along the fiber axis. It remains for future optimization of processing and heat treatment conditions to achieve full three dimensional crystalline order in PBT.

3.2 Light Optical Microscopy of PBT

3.2.1 Coagulation Studies

A dope of 9% PBT in MSA has been examined by polarized light and interference microscopy. Immediately after the droplet was sandwiched between a clean dry glass slide and coverslip, the sample was sealed with molten paraffin. Initial examination revealed a large number of very small defects. After the sample had relaxed for 48 hours, one could observe the classical Schlieren texture (see Figure 3.6) similar to that observed in low molecular weight nematic compounds [25]. Upon rotation of the stage (see Figure 3.7), one observes that the "threads" exhibit maximum extinction at different rotation angles than for the background. These localized regions are where the molecular orientation changes, and have been termed "inversion walls" [26]. Isolated domains near the main droplet appear like spherulites under crossed polars. Closer examination indicates, however, that the extinctions are due to alignment around point defects termed "disclinations" [25,27] (see Figure 3.8).

We have examined the coagulation process and resultant morphology of films formed from solutions of PBT-2122-72 (IV = 18) and poly (p-phenylene terephthalamide), PPTA ($[\eta] = 4.7 \text{ dl/g}$) in MSA. Previously, when a 1.2 wt% PBT in MSA solution was coagulated with H_2O at room temperature between a glass slide and cover slip without a shim, the glass-air-solution interface was unstable and the solution flowed under the weight of the cover slip and caused fingering. When the

coagulant was subsequently introduced, the coagulation front moved in quickly at the indentations in the interface and formed a radially oriented structure (see Figure 3.9). This suggests the solution phase separates into a polymer rich and a MSA/H₂O rich phase. Examination of the back focal plane of the objective lens with a small condenser iris provided an H_y light scattering pattern with minima at 0°, 90°, 180° and 270° to the incident polarization direction and maxima at 45° to the minima. Such scattering patterns are typical of random arrays of bundles of rods. A 1.8% PPTA solution in MSA coagulated with water exhibited similar behavior forming spherical domains (see Figure 3.10).

The glass/solution/air interface of a 6.2 wt% PBT/MSA solution between a glass slide and cover slip was stable, and upon addition of H₂O, the coagulation front moved smoothly into the 3 mm drop for approximately 0.4 mm when a series of roughly circular regions on the average of 100 microns in diameter developed around the perimeter of the coagulation front (see Figure 3.11). This was followed by smooth coagulation until the front neared the drop center where (significantly) a hole was formed. These holes are probably analogous to the voids observed in fibers (see following section) and reflect internal stresses which are developed during coagulation.

3.2.2 Void Content of Fibers

Additional fiber samples have been supplied by Celanese and a table of defect content of all previous fiber samples has been compiled (see Table 3.2). Overall, the number of voids tends to decrease with increase in MSA content in the coagulation bath and lower coagulation bath temperature.

Fibers continuously heat treated at 475°C under N₂ (which were not opaque like the Carnegie Mellon heat treated fibers) as well as further "as-spun" samples have been examined. A survey indicated the fewest fiber defects were observed for a +6 to +8°C coagulation bath. A 10°C bath yielded more defects - perhaps because the fiber did not have sufficient residence time to fully coagulate before entering a harsher (100% H₂O) wash bath.

The heat treated fiber exhibited an axial fine structure not present in "as-spun" fibers (see Figure 3.12). This was corroborated by SEI and so may suggest subfibril formation which correlates with dark field observations and increased SAXS equatorial scattering.

3.2.3 Light Microscopy of Ribbons

PBT tapes prepared from MSA dope in conjunction with Dr. J. Odell and Professor G.C. Berry at Carnegie Mellon University were examined under polarized light. Striations appear perpendicular to the shearing direction. Odell suggested, on the basis of the striation frequency, that these were due to tape vibration from the drive motor. PBT tapes prepared from PPA dope by Odell after modification of the apparatus do not exhibit these striations.

The dichroic ratio, D, of selected fibers and films was measured by outfitting a Zeiss microscope with a KODAK GBX safelight filter with the maximum transmittance at 660 nm and bandpass from 610-780 nm. Successive images were recorded with polarized light with the fiber or film oriented perpendicular and then parallel to the polarization direction. The optical density, σ , was measured from the negative with a spot microdensitometer. D was calculated (see Table 3.3) as follows:

$$D = \frac{\log \frac{\sigma_{\parallel}}{\sigma_0}}{\log \frac{\sigma_{\perp}}{\sigma_0}}$$

where σ_{\parallel} and σ_{\perp} are the optical densities of the fiber or film oriented parallel or perpendicular to the polarization direction, respectively, and σ_0 is the optical density of the background which was considered to be non-absorbing. The orientation function of the transition moment f_{moment} was calculated as

$$f = \frac{D-1}{D+2} = \frac{3 \langle \cos^2 \theta \rangle - 1}{2} .$$

Measures of sample orientation by dichroism are low compared to electron diffraction measures (see section 3.4) and may be due to two effects. First, the transition moment may not be along the chain direction and, secondly, error is introduced into σ_{\parallel} and σ_{\perp} by the fog level of the film.

Samples of PBT films produced by Celanese were examined by reflected light microscopy prior to detachment replication for electron microscopy. Micrographs of both sides of PBT-3271-9-4 before and after heat treatment are shown in Figures 3.13, 3.14 and 3.15 for comparison. The films change in color from maroon to gold with heat treatment, and a blistering of the surface after heat treatment is also noticed.

PBT tapes formed by elongational flow from an MSA dope were also examined by incident polarized light. Voids were observed on both sides of the tape, and

when the stage was rotated into the extinction position, transverse bands could be observed only on one side. However, since the side of the tape which had contacted the rollers during processing was not specified, this phenomena cannot be related at present to processing history. Voids were also observed in the heat treated samples, but additionally, large blisters are present after heat treatment (see Figure 3.15).

3.3 SEI and X-ray Microanalysis of Tapes

SEI of the surface of PBT films from PPA dopes shows axial orientation (see Figure 3.16). Samples of PBT tapes formed from PPA dope in a shear flow were examined for phosphorous content by x-ray microanalysis. The residual PPA content was calculated from the ratio of the integrated intensity of the sulfur peak at 2240ev to that of the phosphorous peak at 2140ev, and assuming that PBT contains 24.1% sulfur, and that PPA contains 41.6% phosphorous. Both the as-spun and heat treated samples contain $2.3 \pm 0.1\%$ PPA ($0.96 \pm 0.04\%$ phosphorous) compared to the average value of 4.9% PPA (2.0%) reported by Celanese for fibers PBT-28555-19-3,-4 and -5 [28]. Processing histories of the tape samples examined are given in Table 3.4 and typical x-ray energy spectra are shown in Figure 3.17.

3.4 TEM Studies of Fibers and Tapes

A JEOL 100CX electron microscope operated at 100KV was used. Images and electron diffraction patterns were recorded on Kodak 4463 and 4489 film. Specimens thin enough for transmission electron microscopy were prepared by detachment replication [27]. Dark field (DF) images were obtained by the tilted beam technique with objective aperture cutoffs of 0.8 nm^{-1} and 2.2 nm^{-1} .

Electron dose was determined by measuring the current on a calibrated phosphor observation screen using the method of Grubb and Groves [30].

3.4.1 Diffraction Studies

Selected area electron diffraction (SAED) and wide angle x-ray diffraction (WAXD) patterns from as-extruded and annealed films are shown in Figure 3.18. WAXD patterns show that the as-extruded film sample is oriented in the draw direction (average azimuthal spread 30-35°); however, the equatorial reflections are broad, indicating only relatively short range lateral order. After annealing under slight tension, the equatorial reflections sharpen indicating a longer range lateral order while the orientation in the extrusion direction remains essentially unchanged.

In contrast to the WAXD patterns, which come from a volume of the films approximately 1 mm x 1 mm x .02 mm, the SAED patterns give a measure of order from a volume of the film approximately 1 μm x 1 μm x 50 nm. SAED patterns of as extruded ribbons exhibit higher orientation in the draw direction than for the bulk ribbon due to misorientation of fibrillated sheets in the WAXD experiment. WAXD line profiles from as processed materials are consistent with SAED, indicating poor lateral order. SAED from annealed ribbons suggests a perfection in lateral order with the high orientation in the extrusion direction remaining unchanged.

3.4.2 Radiation Damage

The diffracted intensity decreases with increasing electron dose to a plateau value caused by scattering from the amorphous carbon support and radiation damaged PBT. The decay of the diffracted intensity with increasing

dose, D , is well modeled as

$$i(D) - i(\infty) = i_0 \exp(-D/D^*)$$

where D^* represents the dose for the intensity to fall to $1/e$ of its initial value and is a characteristic dose for the material. D^* for the second, third and fourth (e_2-e_4) equatorial reflections was determined to be 1.6 coul/cm^2 for annealed PBT (see Figures 3.19 and 3.20). Using data of Dobb [31], D^* is at best 0.2 coul/cm^2 for PPTA. Literature values of $4 \times 10^{-3} \text{ coul/cm}^2$ are reported for both polyoxymethylene (POM) and polyethylene (PE) [30]. Thus PBT is more stable than PPTA, POM or PE. This permits recording of more images at a given magnification or a single higher resolution image at a higher magnification.

DF images were examined as a function of electron dose and the laterally ordered regions were found to remain essentially fixed, constant in size and merely decreased in intensity with increased total dose. One can therefore obtain useful equatorial DF images up to a total dose of approximately D^* .

3.4.3 Imaging of Coherently Scattering Regions

Bright field (BF) (Figure 3.21) micrographs of detached fragments from as extruded and annealed PBT ribbons show that fibrillated sheetlike fragments are detached. Figure 3.22 shows e_1 and e_2-e_4 DF images from the same area of an annealed PBT film. The projection of the laterally ordered regions averages 10 nm wide by 16 nm long with no regions observed to be longer than 40 nm. The micrographs show a relatively uniform spatial distribution of laterally ordered regions within the fragment. When the objective aperture is set to accept only the non-equatorial component of the e_2-e_4 reflections, one still finds a uniform

spatial distribution of laterally ordered regions within the fragment. This shows that PBT ribbons do not possess a "pleated sheet" type structure similar to that proposed for PPTA by Dobb [32].

Meridional DF images from annealed PBT ribbons do not exhibit any prominent diffraction contrast. This is in agreement with the model proposed by Roche [23] and Atkins [24] since laterally ordered chains with translational freedom along the chain axis do not form fully 3-dimensional crystalline regions and therefore cannot be imaged by (oo ℓ) DF electron microscopy.

Equatorial DF from as-extruded films reveals a bright speckle always less than 2 nm in size. Such small scale image detail requires careful work to quantify since the microscope optics strongly influence the image at this level. Furthermore, images must be obtained only from the thinnest areas of the fragments in order to satisfy the requirement that the thickness of the specimens be not much greater than the size of the projected object in order to avoid artefacts arising from a two dimensional projection of a three dimensional object. Recognizing these problems, it is estimated that laterally ordered regions in as-extruded PBT ribbons are less than 2 nm in size.

3.4.4 Effect of Heat Treatment as Assessed by Dark Field Imaging

Figures 3.23 and 3.24 are dark field images using reflections e₁ and e₂ - e₄ of as-spun PBT (fiber #28555-19-2,19-5). These as-spun fibers do not show sharp reflections on the equator. As in the case of as-spun ribbons, very small (2 ~ 4 nm) coherently scattering regions were observed in the dark field image. From the point of view of size of the coherently scattering regions, there is no significant difference between the mechanically good and poor as-spun fibers (see Table 3.5).

When as-spun fibers are heat treated, the mechanical properties are improved. Dark field images show that the diffracting regions increase in width (to 5 times) and length (to 10 times) compared to the as-spun fibers (see Figures 3.25, 3.26 and Table 3.5).

3.4.5 Deformation Bands

Microscopy of sonicated specimens showed the presence of deformation bands produced during sample preparation (see Figure 3.27). Two types of deformation bands have been formed in ribbon-like fragments of PBT and (PPTA). Type I deformation bands are characterized by an abrupt inclination of the chains with respect to the fiber axis and longitudinal fracture of the fiber. Type II deformation bands appear as thick regions normal to the fiber axis. Detailed electron diffraction studies have been carried out to study the crystallography of the bands. Only the e_1 reflection is observable on the equator for type II deformation bands. Type I deformation bands have a combination of e_2 and e_4 reflections on the equator with a second set of e_4 reflections unaccompanied by a second set of e_2 reflections at an angle approximately 55° to the equator.

PBT fiber (28413-40-1) was mechanically rolled along the fiber axis by placing a fiber on a glass slide on a hot plate at 450°C and rolling with a glass rod. The originally rod-shaped PBT fiber deformed into a tape-like shape. This deformed (rolled) fiber was treated in the same method as mentioned above for detaching specimens for electron microscopy. Figure 3.28 shows the results of microdensitometry of the equatorial region of diffraction patterns of the original fiber, deformed, and heavily deformed specimens. In the pattern of the heavily deformed specimen, the e_1 and e_4 reflections are very intense, whereas

the e_2 and e_3 reflections have disappeared with rolling. The trend of intensity variation with rolling revealed that e_1 and e_4 belong to the same type of hk reflection. Figure 3.29 shows a dark field image by e_1 in which the population of bright diffracting regions is very dense - consistent with the preferred orientation of e_1 evidenced in the diffraction pattern.

3.4.6 Microtoming

Preliminary attempts of microtoming of PBT fibers perpendicular and parallel to the fiber axis have been carried out at room temperature. Fibers were imbedded in a mixture of Epon 12 and hardner, and kept at approximately 60°C for three days. The ratio of amount of Epon 12 to that of hardner determined hardness of the embedding material. A ratio of 1/1 was too soft to hold the fibers on sectioning but a 3/1 ratio made slicing possible in a plane perpendicular to the fiber axis.

Figure 3.30 is a TEM electron micrograph of the fiber cross section. The fiber was originally circular but after slicing, the section has deformed into an ellipsoid. The ratio of the two axes of the ellipsoid ranged from 1.2 to 2.0. The PBT material deforms much more than the embedding material. Electron diffraction showed chain molecules were tilted toward the sectioning direction.

3.4.7 Lattice Imaging of PBT

Heat treated PBT fiber (#28413-40-4) was detachment replicated for high resolution electron microscopy. Thin regions of the fiber suspended over small holes in the carbon film substrate were examined at 100,000X direct magnification in axial bright field using an objective aperture with rather large (3 nm^{-1}) cutoff. This aperture admits reflections e_1 - e_3 and m_1 - m_3 . Radiation

studies (see section 3.4.2) indicate the possibility of lattice imaging using the e_1 or e_2 reflections.

Figure 3.31 shows several regions exhibiting fringes of approximately 5.8 Å spacing with the fringe periodicity normal to the fiber axis corresponding to the prominent e_1 reflection ($d = 5.88 \text{ \AA}$). Lattice image regions are circa 200 Å in width and circa 400 Å in length (along the fiber axis) in agreement with the bright coherently diffracting regions visible in conventional e_1 dark field images.

3.5 SAXS of PBT Fibers and Ribbons

SAXS from as extruded and annealed PBT fibers and ribbons is governed by void scattering, i.e., a continuous, monotonic decrease in the equatorial scattered intensity, and no long period is observed (see Figure 3.32 and 3.33). This suggests that there are no periodic fluctuations in electron density. When one also considers the lack of an 'amorphous halo' in the WAXD and SAED patterns, it is reasonable to conclude the material is single phased with ordered regions separated from other laterally ordered regions by defects. An increase in SAXS intensity upon heat treating suggests that there is an increase in the volume fraction of voids during heat treatment.

3.6 SANS of PBT Solutions and Tapes

Six different (dilute) D_4H_2 -PBT/MSA solutions have been sent to Carnegie Mellon for light scattering studies. The polymer was dried for several days at 125°C under vacuum. MSA was distilled under vacuum and stored under a blanket of prepurified nitrogen prior to use. Solutions were prepared in a glove box with air circulated over Drierite. No precautions were taken to exclude dust,

which requires the solutions to be clarified prior to light scattering.

A nematic PBT dope (9.24 wt%) was prepared from equal weights of D₄H₂-PBT-3271-13 (IV = 4.75) and PBT-3271-2-(IV = 7.3). Part of this solution and the 34.3×10^{-4} g/ml solution are to be sealed in their respective quartz cells for subsequent small angle neutron scattering (SANS) at Oak Ridge National Laboratory. The remainder of the 9.24 wt% solution is to be used to prepare films for SANS.

Table 3.1
Calculated and Observed Equatorial Structure Factors for PBT

hk	f_c^*	f_o
10	58.3	58.3
01	100.0	100.0
11	46.1	41.7
20	31.9	29.1
21	0.1	5.8
21	12.2	11.7
30	1.9	5.8
31,02	26.5	29.1
12	9.1	14.1
31	13.3	18.3

R = .096

* temperature factor of 6 \AA^2 assumed

TABLE 3.2
Defect Analysis of Celanese Fibers PBT-27554-#

#	I.V. Polymer	Total Voids per mm	dpf ¹	% MSA Bath 1/2	Temp °C	SDR ³	% Polymer in dope	Tenacity ² g/den
6-1	14	too thick	5.1	37.5	RT	2	9.5	9.0/8.0
6-2	14	15.6	4.2*	37.5	RT	2	9.5	8.9/11.0
6-3	14	15.6	3.1*	50	RT	2	9.5	10.0/16.5
9-1	18	.7	5.4*	50	RT	2	9.5	9.1/10.2
9-3	18	1.7	5.3*	50	RT	2	9.5	8.5/8.7
9-5	18	.56	3.3*	50	RT	3.9	9.5	9.3/8.3
9-6	18	3.9	6.5*	37.5	RT	2	9.5	8.0/8.6
9-7	18	5.1	5.2*	37.5	RT	2	9.5	8.2/7.9
9-10	18	7.3	5.3*	25	RT	2	9.5	7.0/8.5
9-11	18	3.5	6.3*	25	RT	2	9.5	7.4/8.4
24-4	18	2.3	1.6*	50	23	3.9	9.5	9.5
24-6	18	1.4		50	8	4.8	9.5	
24-8	18	1.9	1.9*	50	8	3.5	9.5	10.8
24-9	18	0.55	2.6*	50/50	8/24	2	9.5	10.2
27-1	18	unseparable	1.7*	50	-10		9.5	9.4
27-2	18	3.0	2.2*	50	-5		9.5	8.7
27-3	18	2.3	3.8*	50	19		9.5	5.0
27-4	18	unseparable	1.9*	50/50	12-19/23		9.5	8.8
27-5	18	4.8	4.0*	50/50	4-0/23		9.5	5.2
27-6	18	4.4	3.7*	50/50	-1/23		9.5	5.5
27-7	18	2.1	1.8*	50	0		9.5	9.2
33-4-2	18	1.6		50	24	3.8	11	
33-5-255	18	1.6		50	24	4.9	11	
48-1	31	too thick	20-7@	50	RT	.26	8	.69
48-2	31	2.1	4.4@	50	RT	.96	8	3.2
48-3	31	2.6	2.2@	50	RT	1.9	8	8.2
48-4	31	4.2	1.6@	50	RT	2.9	8	8.5
48-5	31	2.5	1.3@	50	RT	3.8	8	7.6
48-6	31	too thick	9.4@	50	RT	.53	8	1.7
48-7	31	1.9	4.7@	50	RT	1.1	8	6.6
48-8	31	2.5	3.2@	50	RT	1.6	8	9.0
48-9	31	3.2	2.3@	50	RT	2.1	8	10.3
48-10	31	3.3	1.8@	50	RT	2.6	8	10.6
48-11	31	2.8	2.2@	50	RT	2.1	8	10.2
48-12	31	2.1	2.3@	50	RT	2.1	8	10.5
48-13	31	.52	4.6@	62.5	RT	1.1	8	8.6
48-14	31	.38	2.4@	62.5	RT	2.1	8	10.0

¹The deniers, supplied by Celanese, were determined by two methods

*denotes vibrascope @denotes weight

The two measurements differed by 45% for the case of fiber 48-2, the vibrascope giving higher values in all cases where both were measured.

²Tenacity values are reported Celanese value/UMass value

³SDR - spin draw ratio

Table 3.3
Orientation by Dichroism

<u>Sample</u>	<u>D</u>	<u>f</u>	<u>$\langle \cos^2 \rangle_{moment}$</u>	<u>$\langle \theta \rangle_{moment} (^\circ)$</u>
Film-II-61-B-3	0.895	-0.362	0.309	56.2
Film-2-2	1.62	0.171	0.447	48.0
Fiber 27554-42-1	2.60	0.348	0.565	41.3
Fiber 27554-24-8-B	6.23	0.635	0.757	29.5

TABLE 3.4

Processing Histories & Mechanical Properties of Tapes

<u>SAMPLE*</u>	<u>HEAT TREATMENT</u>	<u>MODULUS(g/den)</u>	ϵ_b (%)	T_b^+ (g/den)	$\dot{\gamma}_{FORM}(s^{-1})$
as-spun	-----	145	5.0	5.0	26
heat treated	400°C 10 min. 50 g load	659	0.8	9.6	26

*Samples and mechanical data supplied by Dr. J. Odell

T_b - strength at break

ϵ_b - strain at break

$\dot{\gamma}_{FORM}$ - shear rate of film formation

TABLE 3.5
Dark Field Image Sizes for Various Fibers

Fiber	T_b g/d	Modulus g/d	Diffracting Length	Region Width
As-Spun 28555-19-2	13.6	377	2-4	2-4
As-Spun 28555-19-5	13.8	578	2-4	2-4
Heat Treated 28413-40-1	8.5	590	2-30	4-20
Heat Treated 28413-40-4	20.0	1900	2-40	10-20

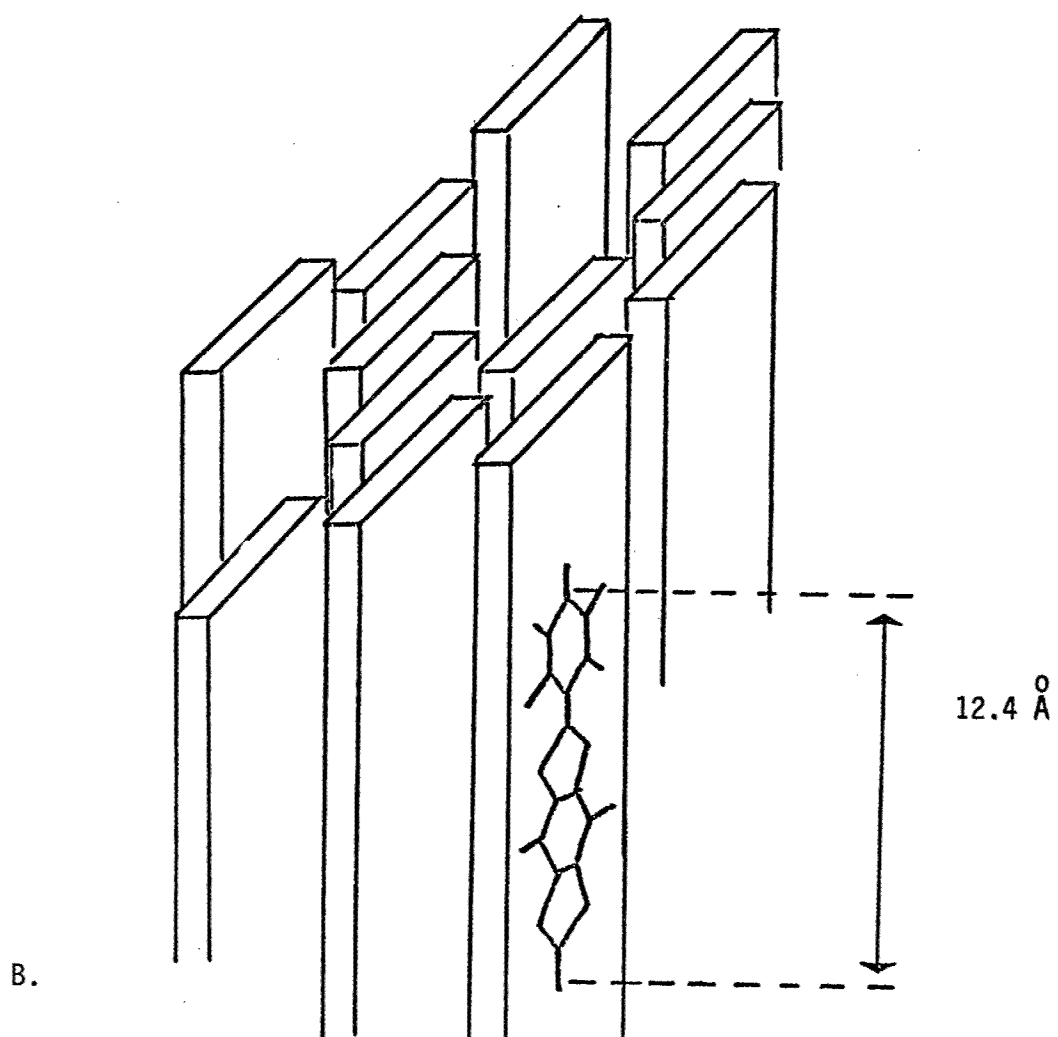
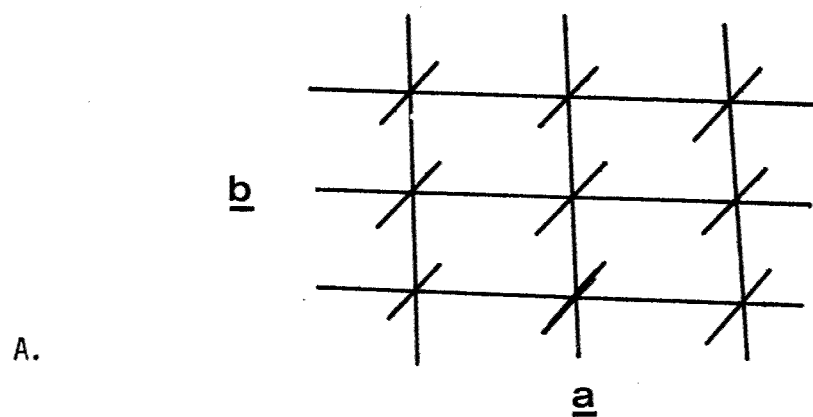


Figure 3.1: Structure of PBT proposed by Roche [23]

A. a b projection of unit cell

B. Schematic view showing packing of chains

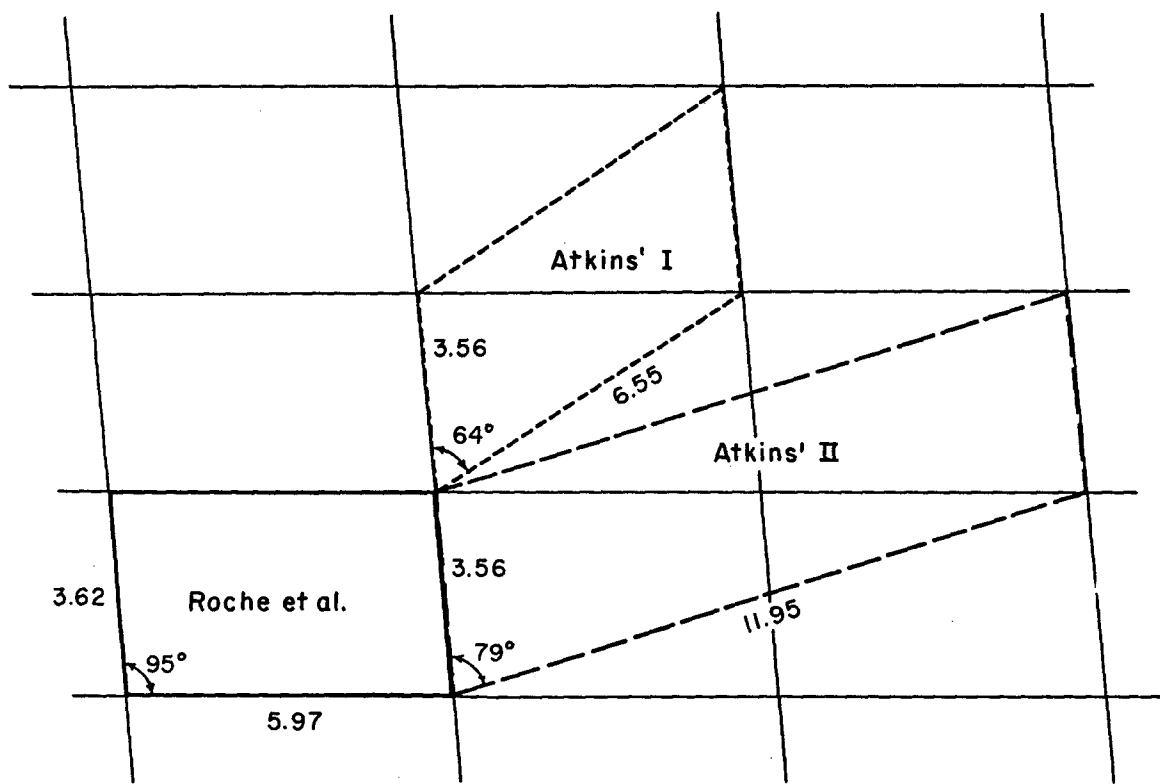
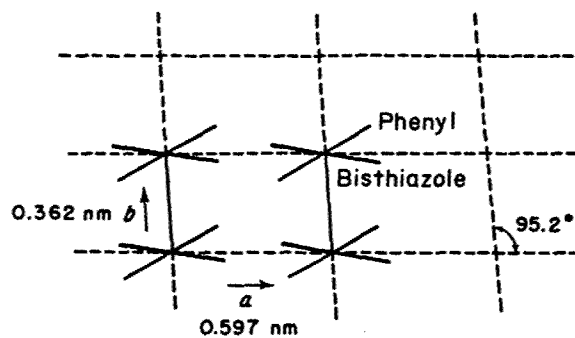
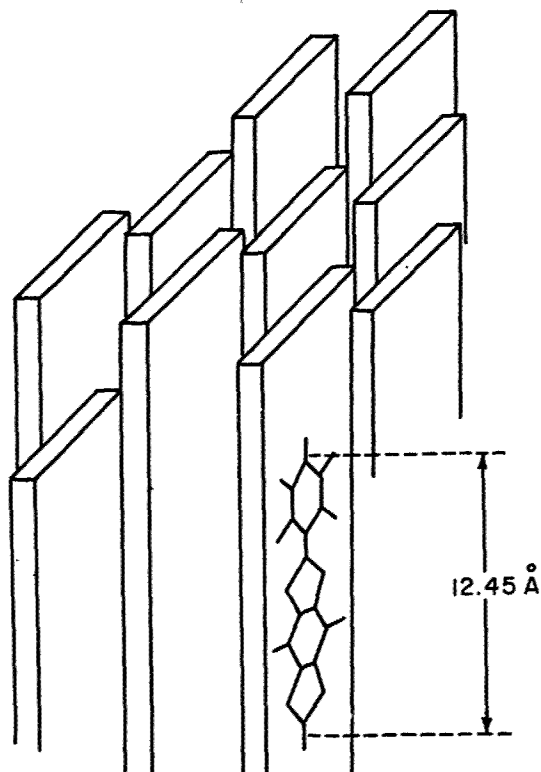


Figure 3.1c: Comparison between projection of unit cells proposed by Roche [23] and Atkins [24]



A.



B.

Figure 3.2: Refined structure of PBT
 A. a b projection of PBT unit cell
 B. schematic view of packing of chains

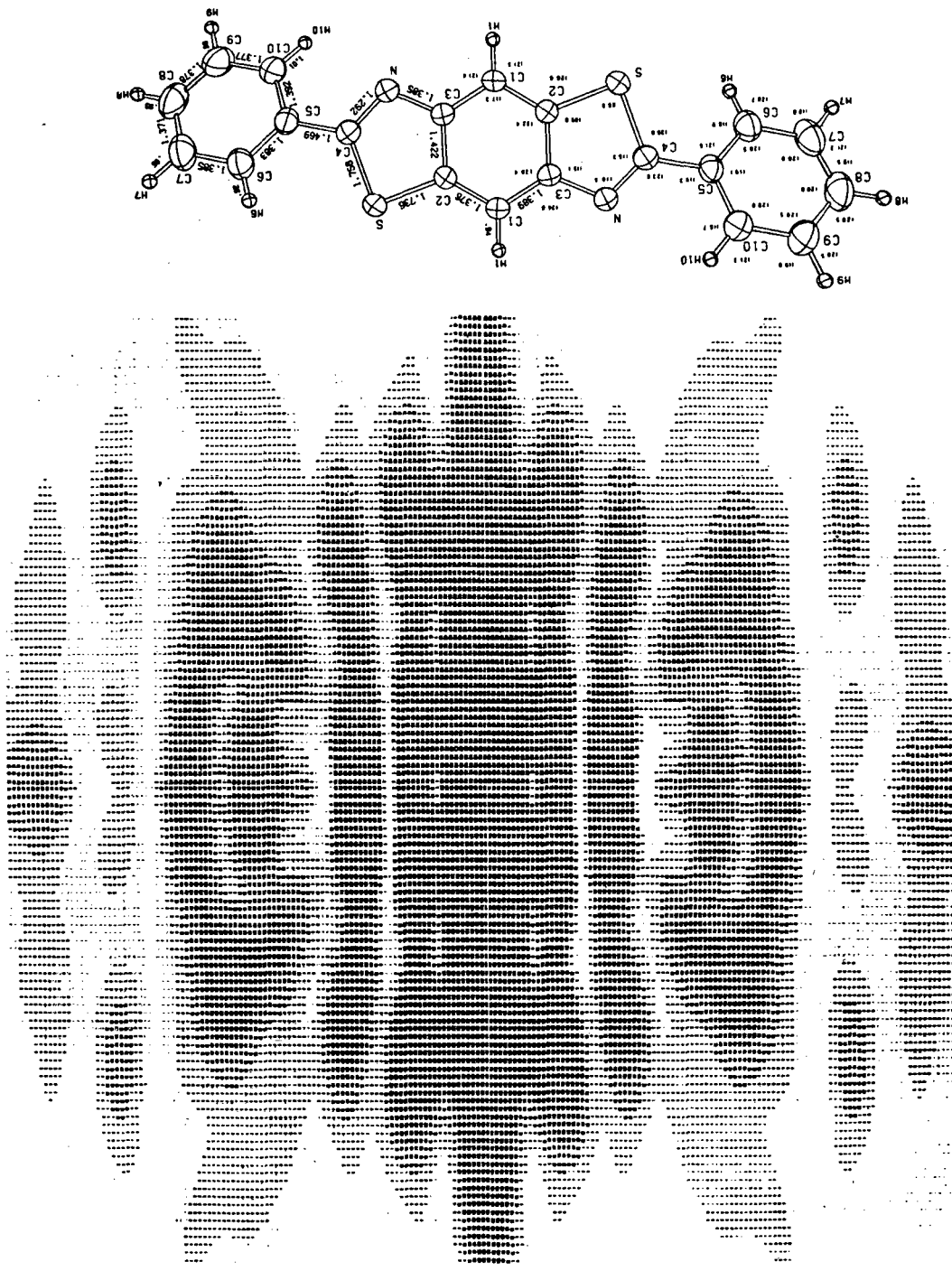


Figure 3.3: Cylindrically averaged Fourier transform of a single PBT repeat unit (courtesy Atkins [24])

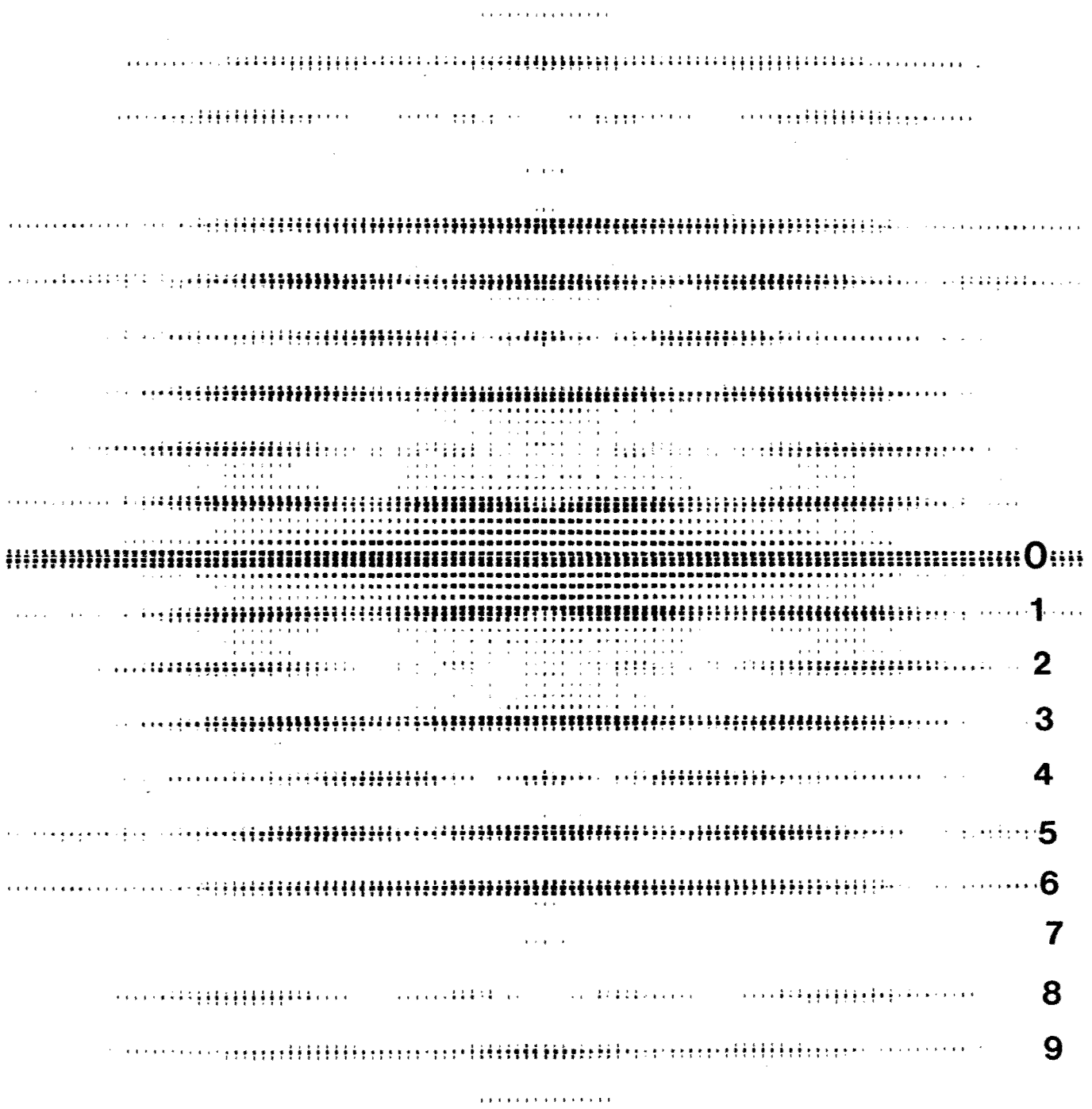


Figure 3.4: Cylindrically averaged Fourier transform from a single PBT chain of 10 repeat units. Chain axis is vertical (courtesy Atkins [24])

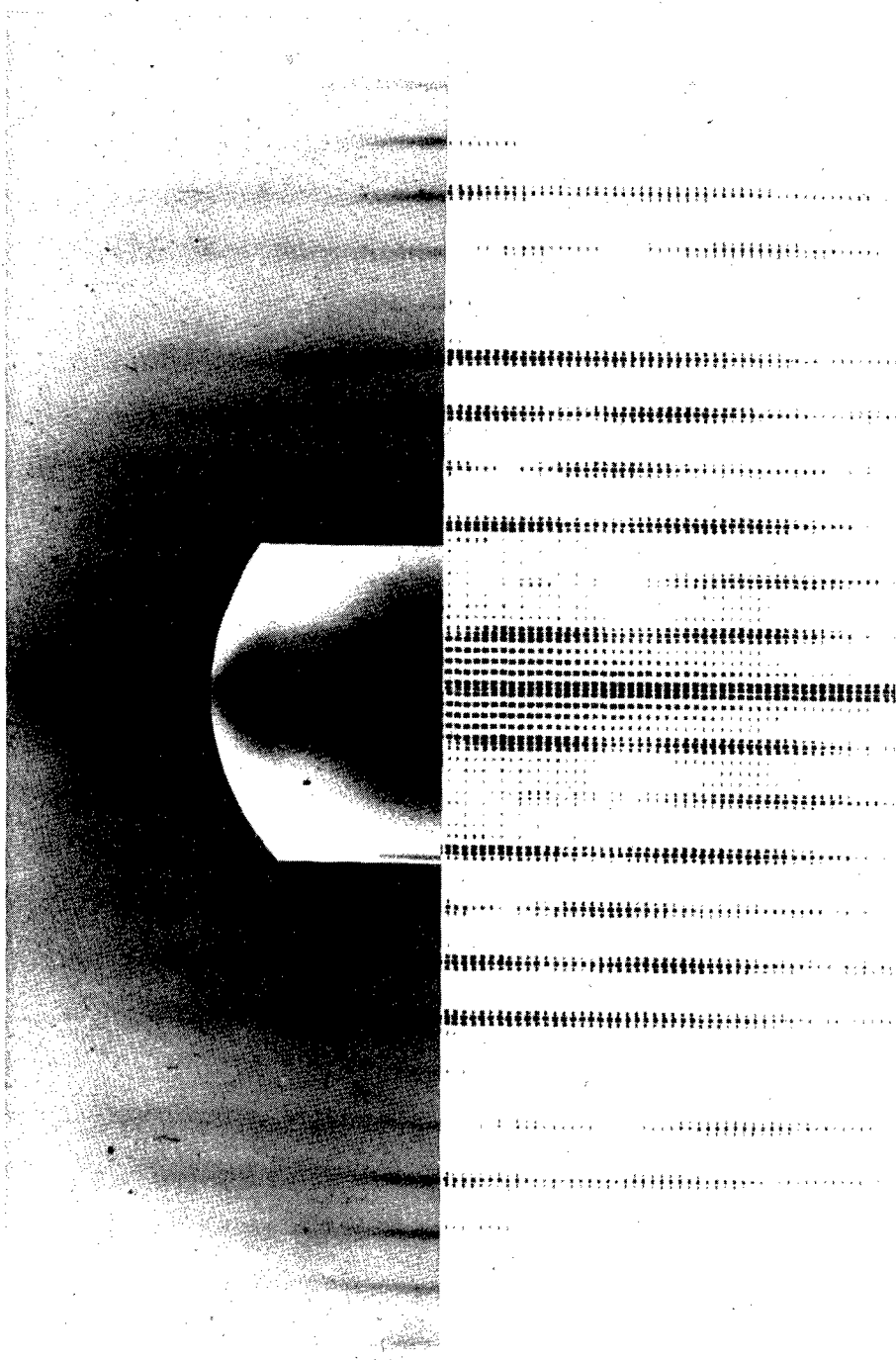


Figure 3.5: Comparison between electron diffraction from PBT and cylindrically averaged transform



Figure 3.6: Schlieren texture in 9% PBT in MSA after 48 hours relaxation

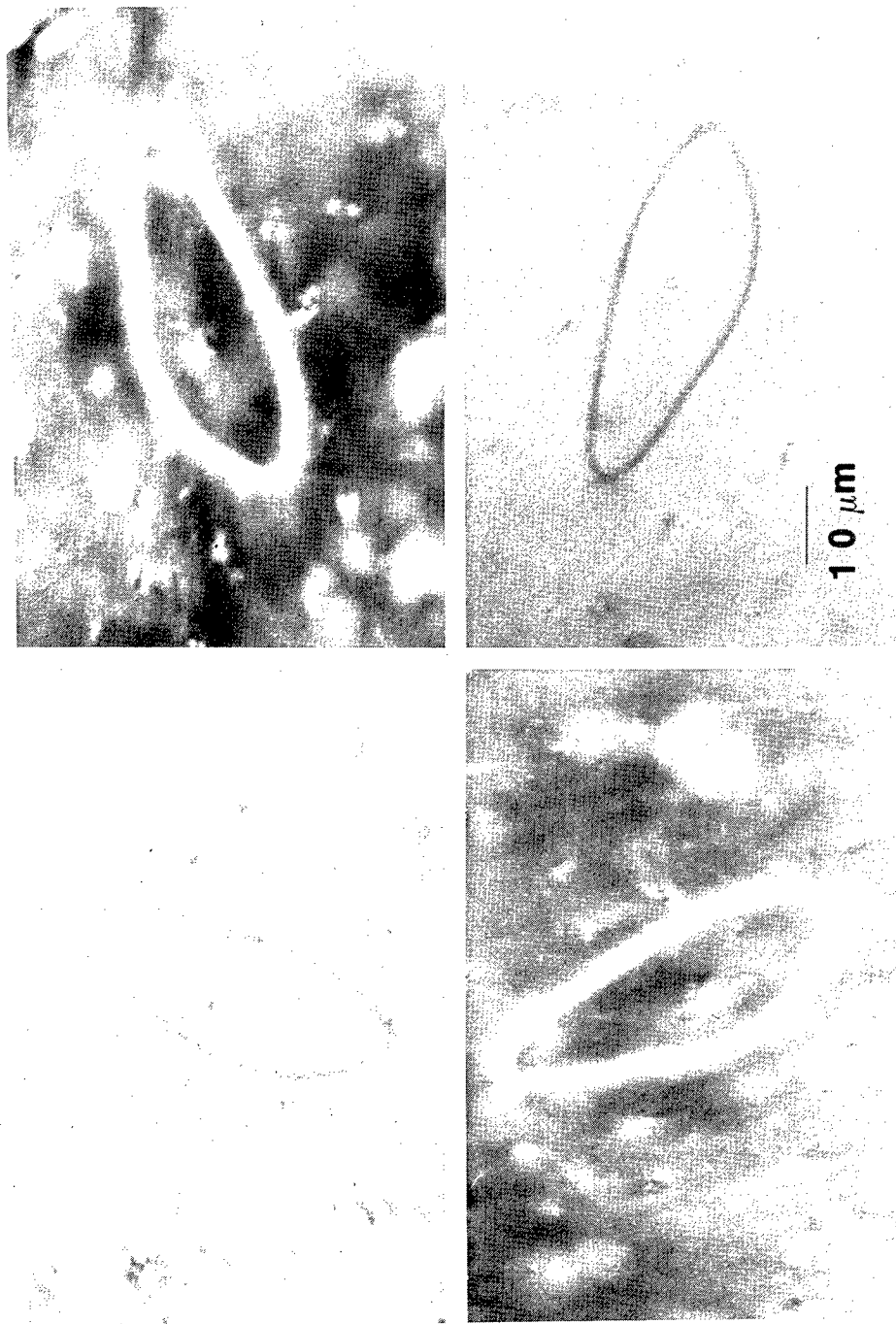


Figure 3.7: Inversion wall in 9% PBT in MSA as a function of orientation:
polarizer vertical, analyser horizontal

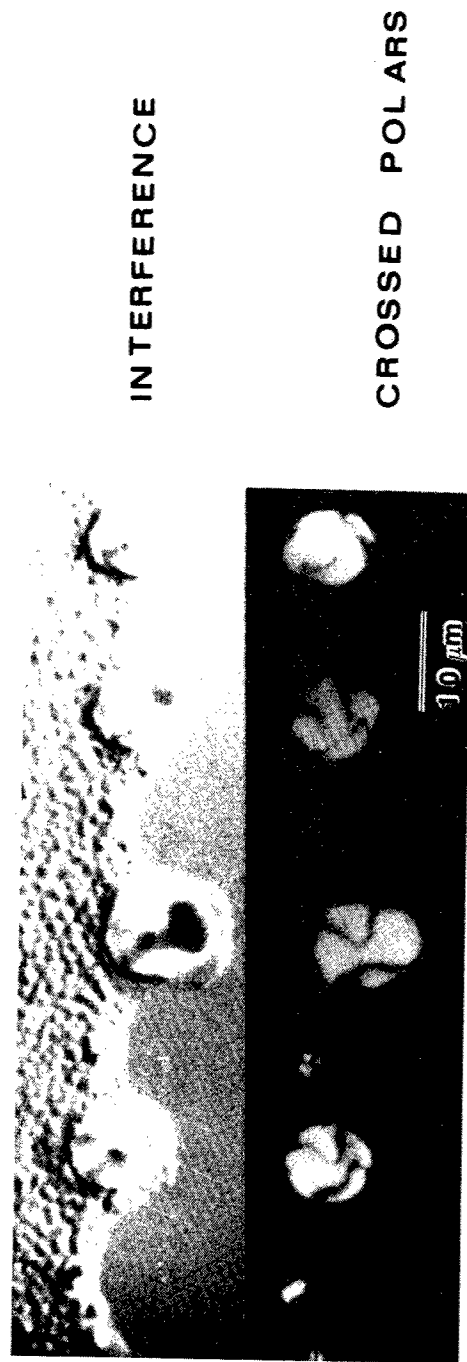


Figure 3.8: Anisotropic PBT/MSA domains in an isotropic matrix as viewed by interference and polarized light microscopy

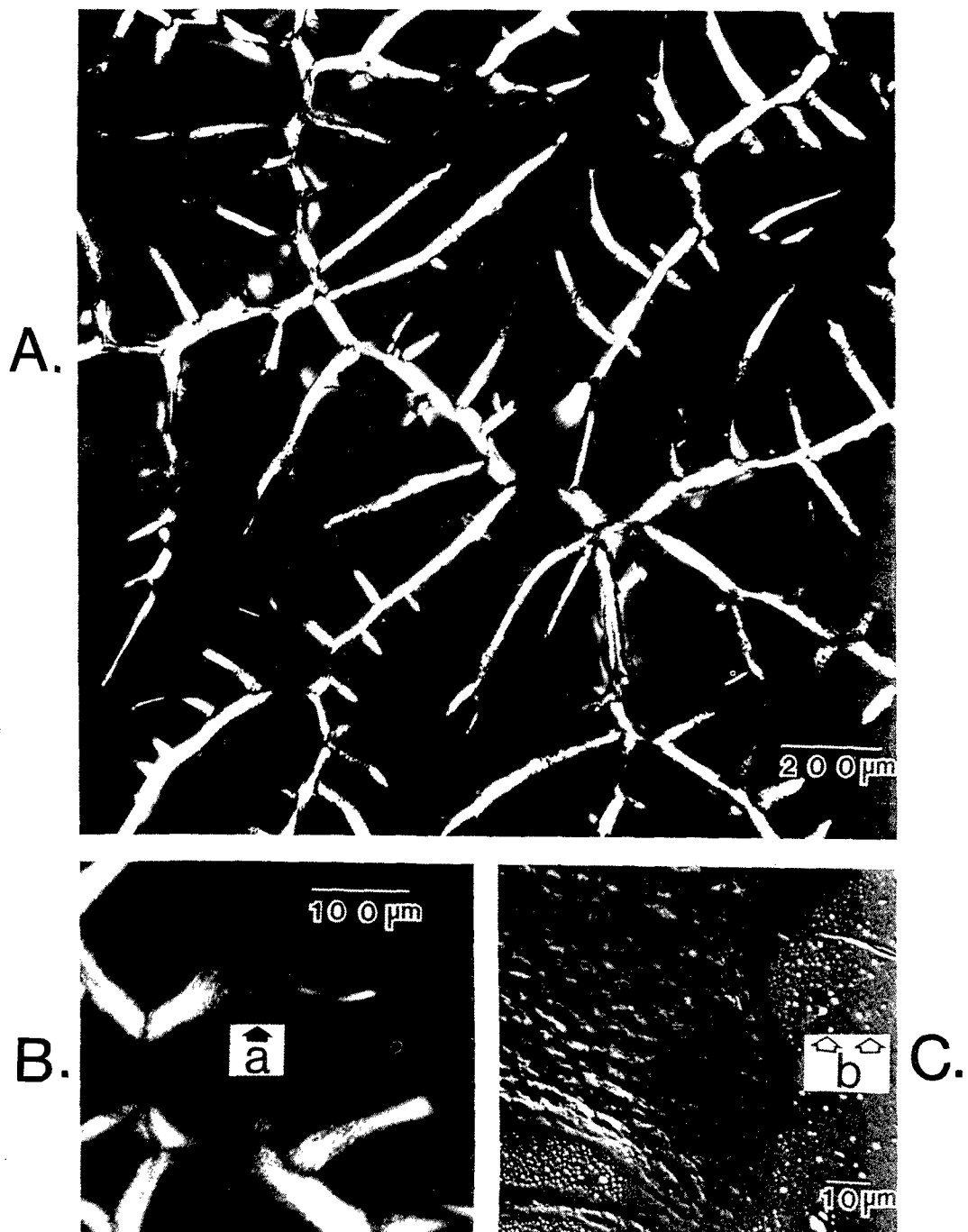


Figure 3.9: (A) Radial structure of 1.2% PBT coagulated with H₂O (crossed polarizers) (B) Enlarged view of one radial branch (C) Interference micrograph of area like (B).
 a. indicates PBT rich region b. indicates MSA/H₂O rich region

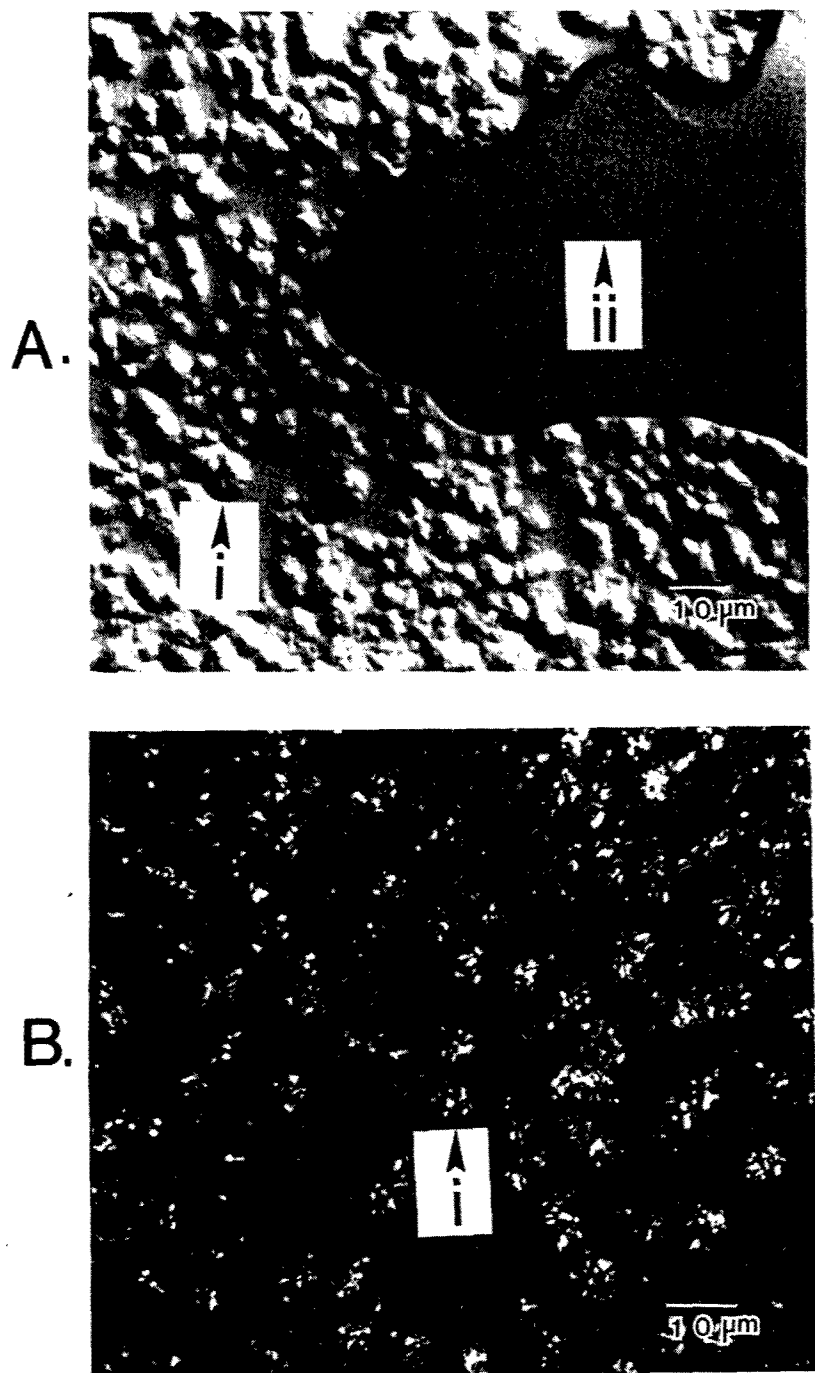


Figure 3.10: (A) Interference micrograph of 1.7% PPTA coagulated with H_2O (b) Crossed polars
i. represents PPTA rich domains
ii. represents MSA/ H_2O rich domains

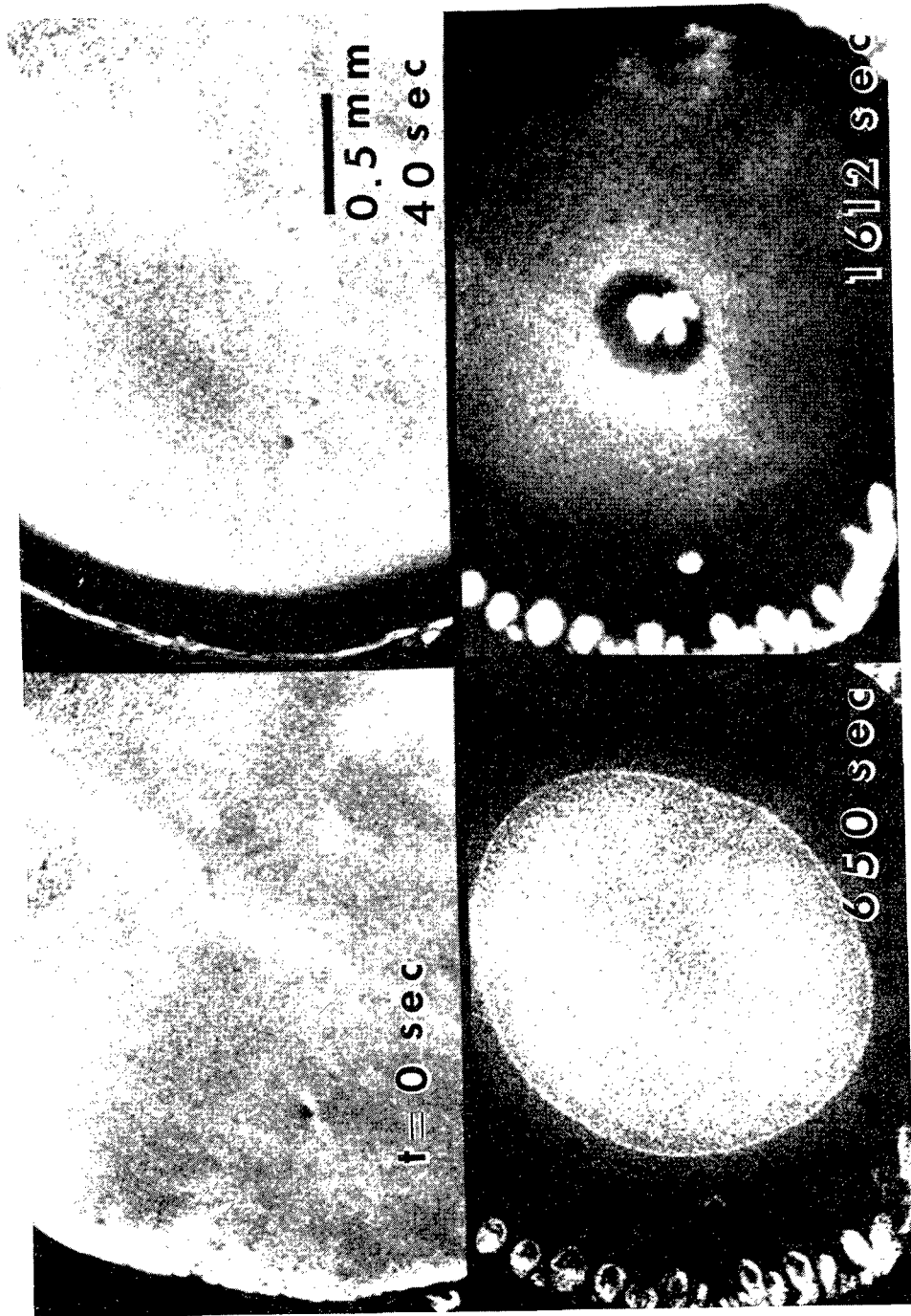


Figure 3.11: Coagulation of a drop of 6.2 wt% PBT in MSA with H_2O

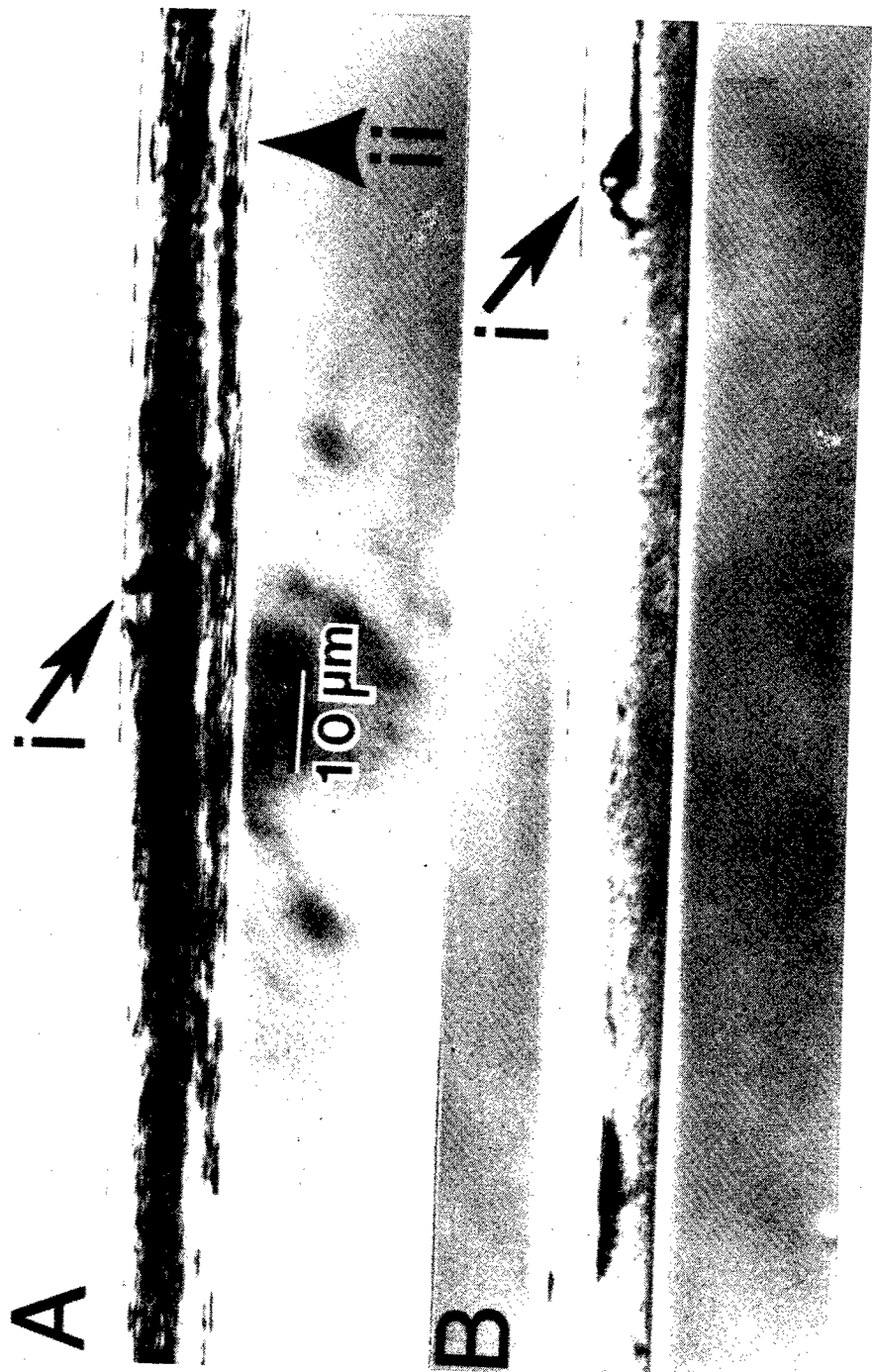


Figure 3.12: (A) PBT 27554-42-1 475°C heat treatment
(B) PBT 27554-24-8B typical 'as-spun' fiber
i. indicates voids present in both fibers
ii. indicates fibrillation during heat treatment

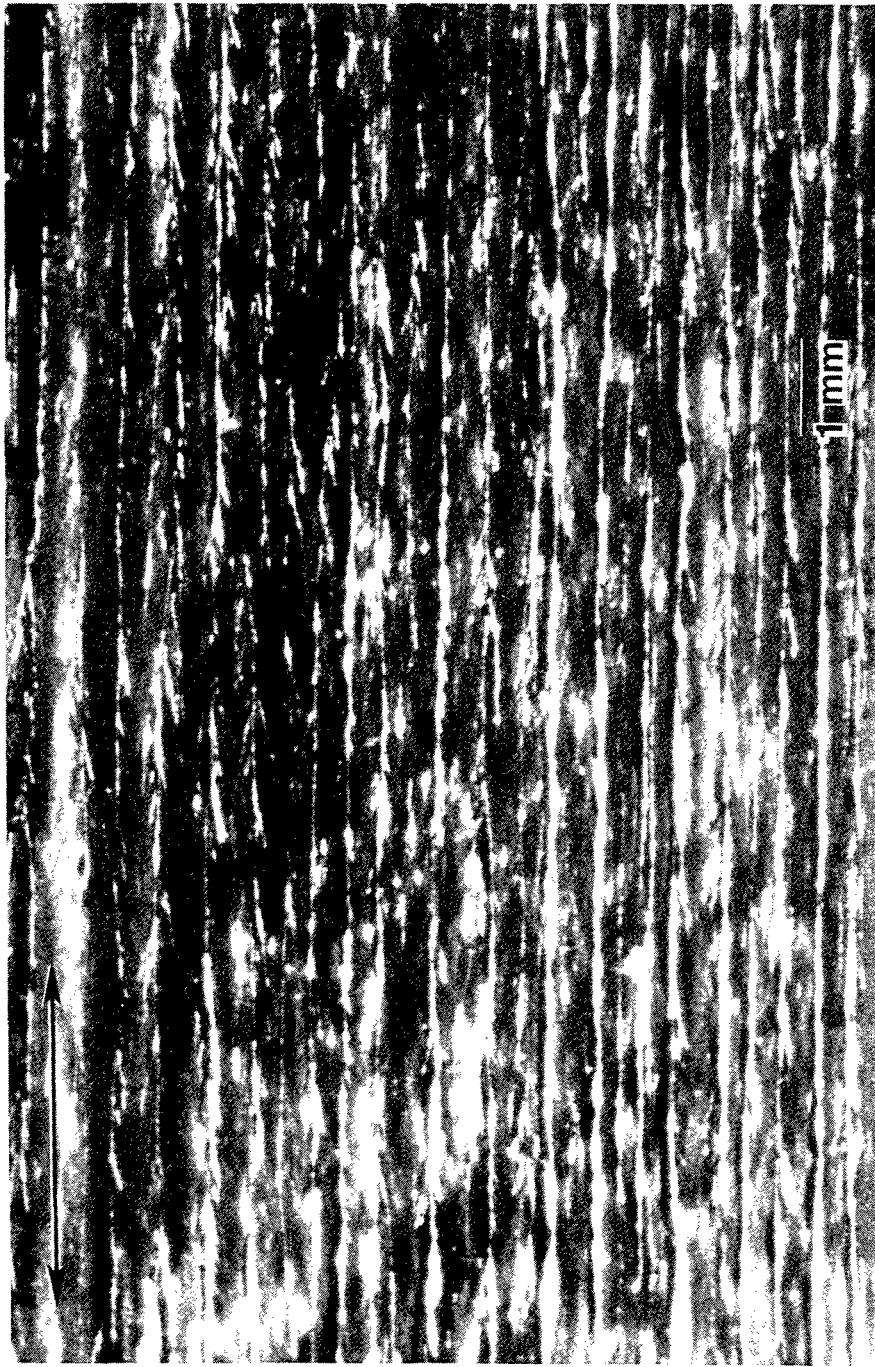


Figure 3.13: (a) PBT 3271-9-4 as-extruded, side 1



Figure 3.13: (b) PBT 3271-9-4 as-extruded, side 2

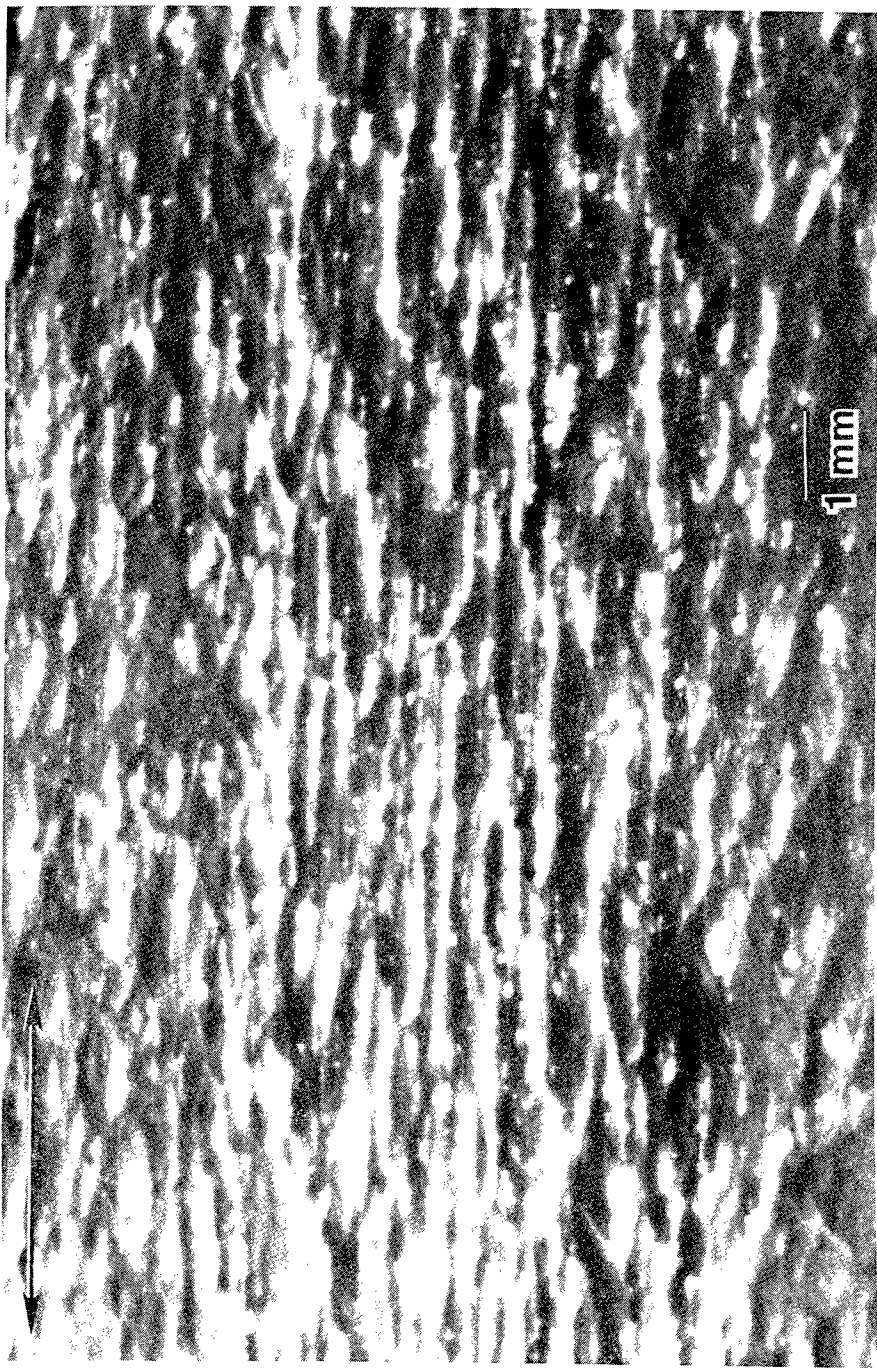


Figure 3.13: (c) PBT 3271-9-4 annealed at 475°C , side 1



Figure 3.13: (d) PBT 3271-9-4 annealed at 475°C, side 2

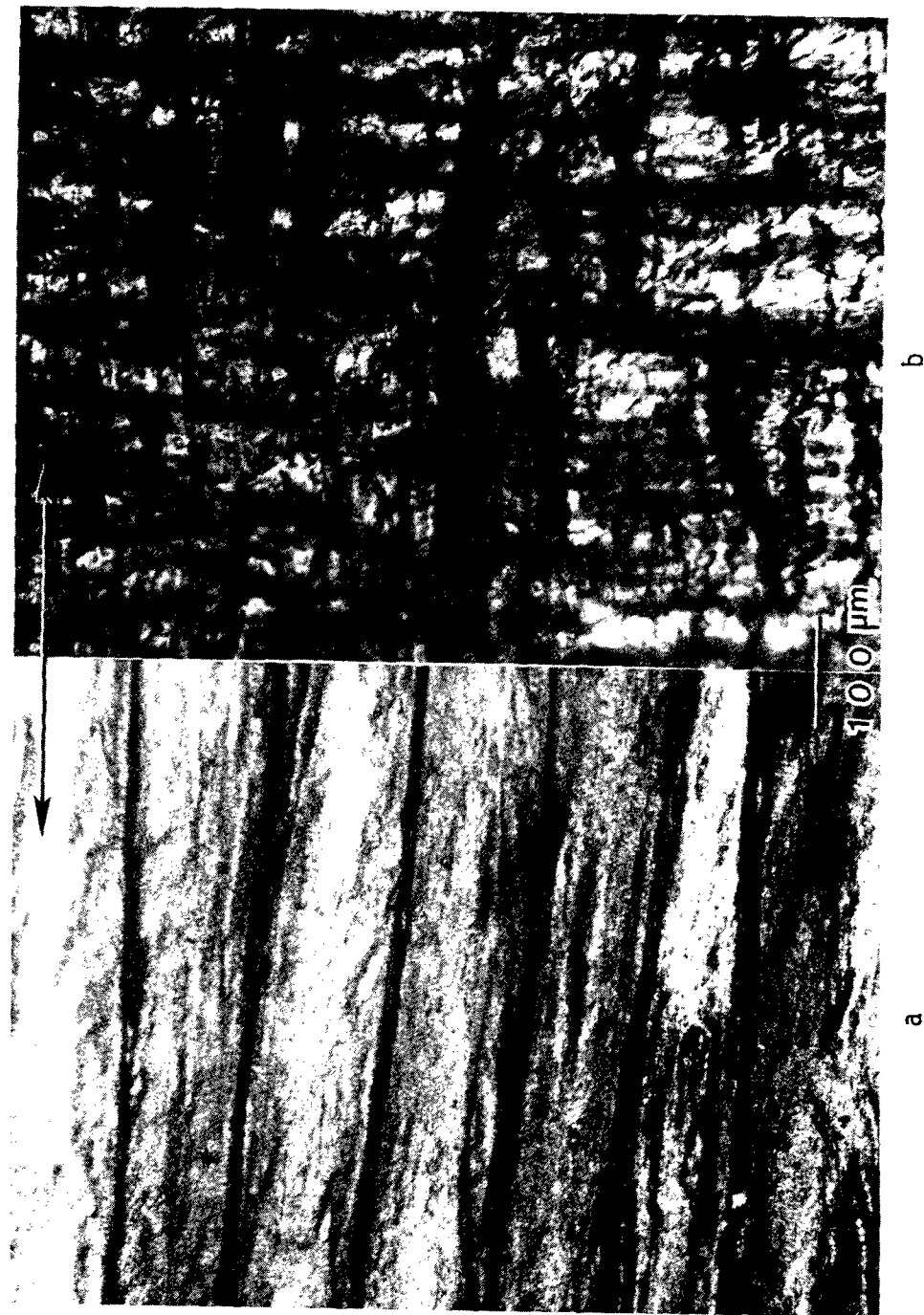


Figure 3.14: Reflected polarized light micrograph of PBT 28555-25-4
(a) side 1 (b) side 2

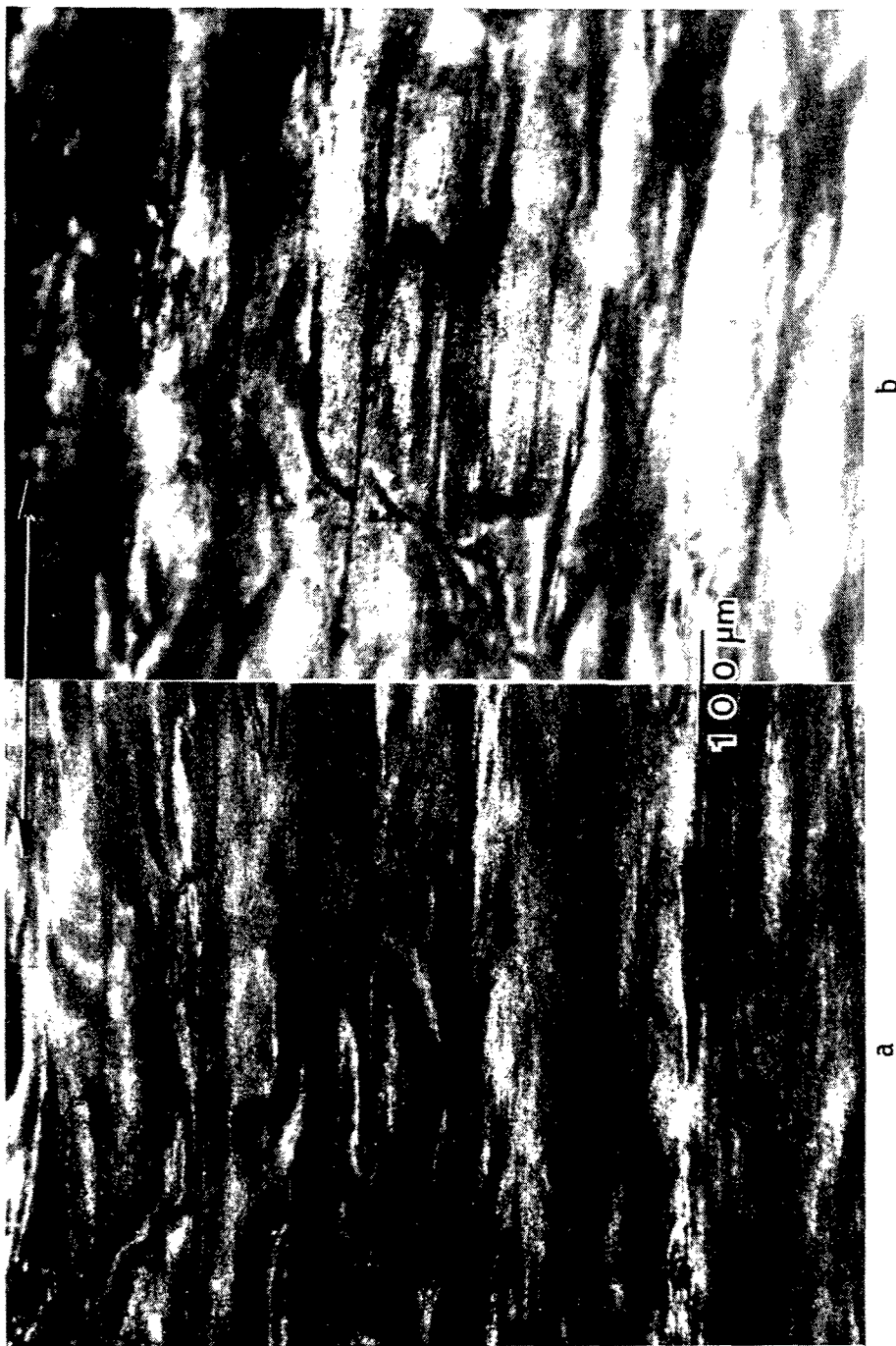


Figure 3.15: Reflected polarized light micrograph of PBT 28555-25-4
annealed at 475°C
(a) side 1 (b) side 2



Figure 3.16: SEI of PBT film from PPA solution

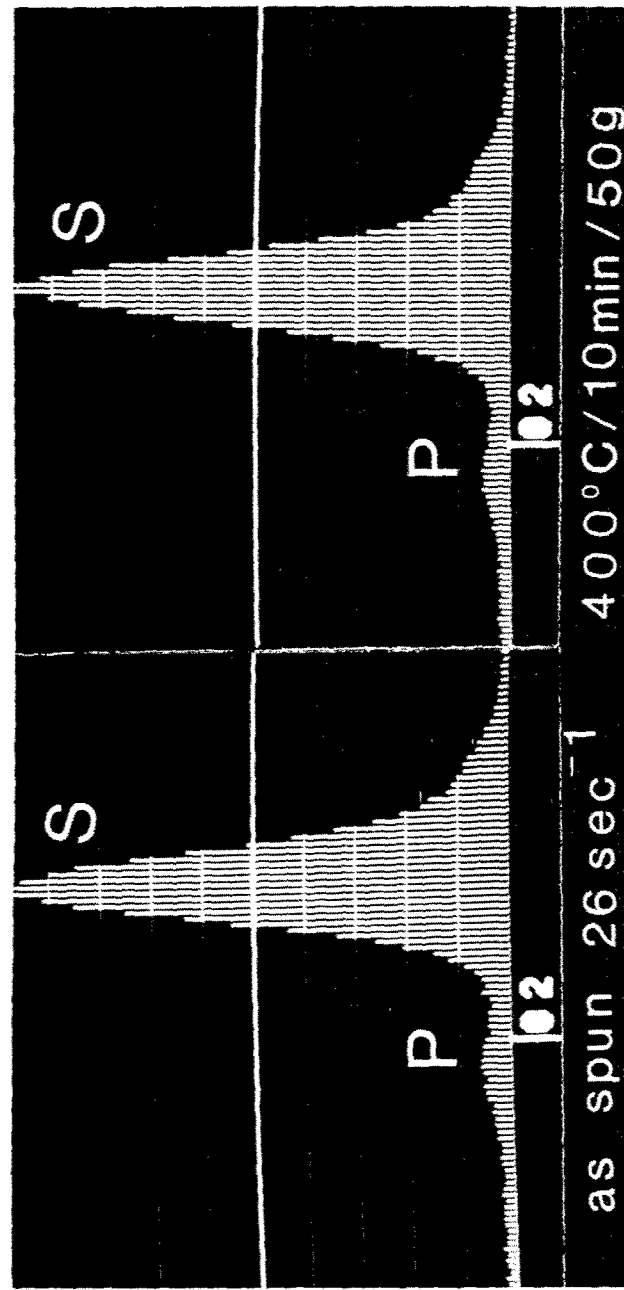
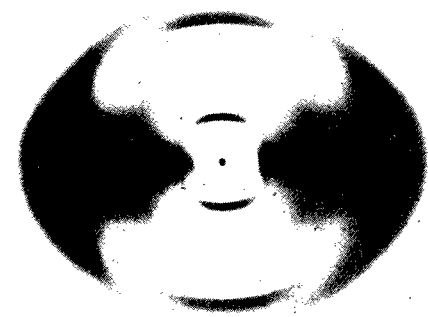
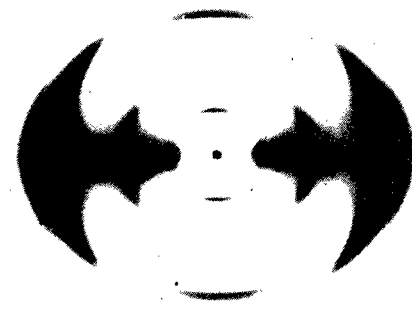


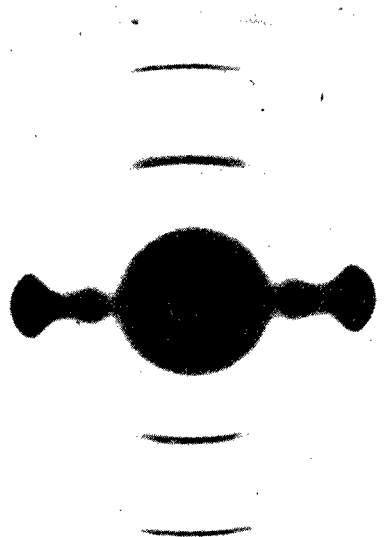
Figure 3.17: X-ray microanalysis of PBT film from PPA.
 $\gamma = 26 \text{ gm}^{-1}$



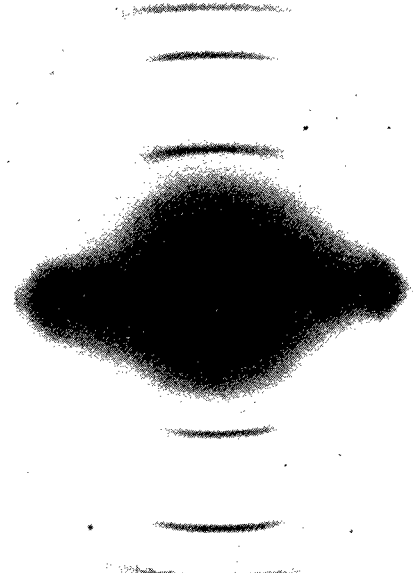
a



b



c



d

Figure 3.18: WAXD and SAED of as-extruded and annealed PBT films
(a) as-extruded, WAXS (b) annealed at 475°C WAXS
(c) as-extruded SAED (d) annealed at 475°C SAED

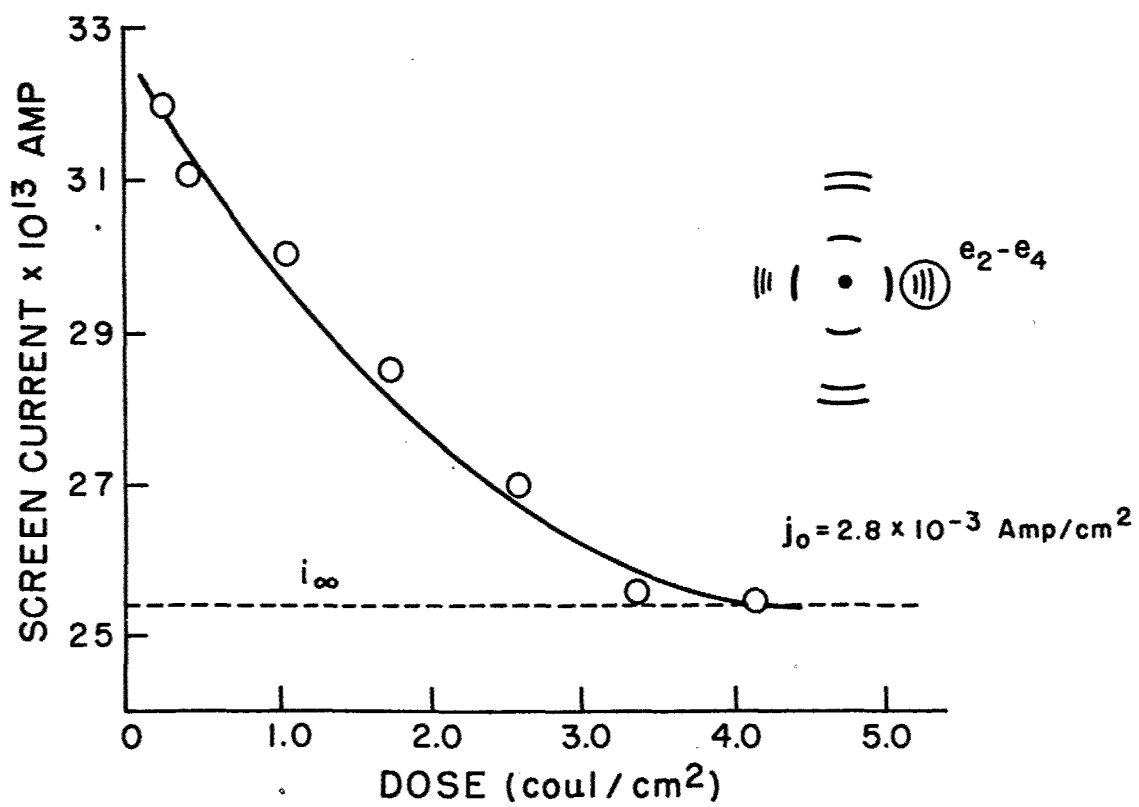


Figure 3.19: Decrease of scattered intensity from e_2 , e_3 , e_4 reflections from PBT

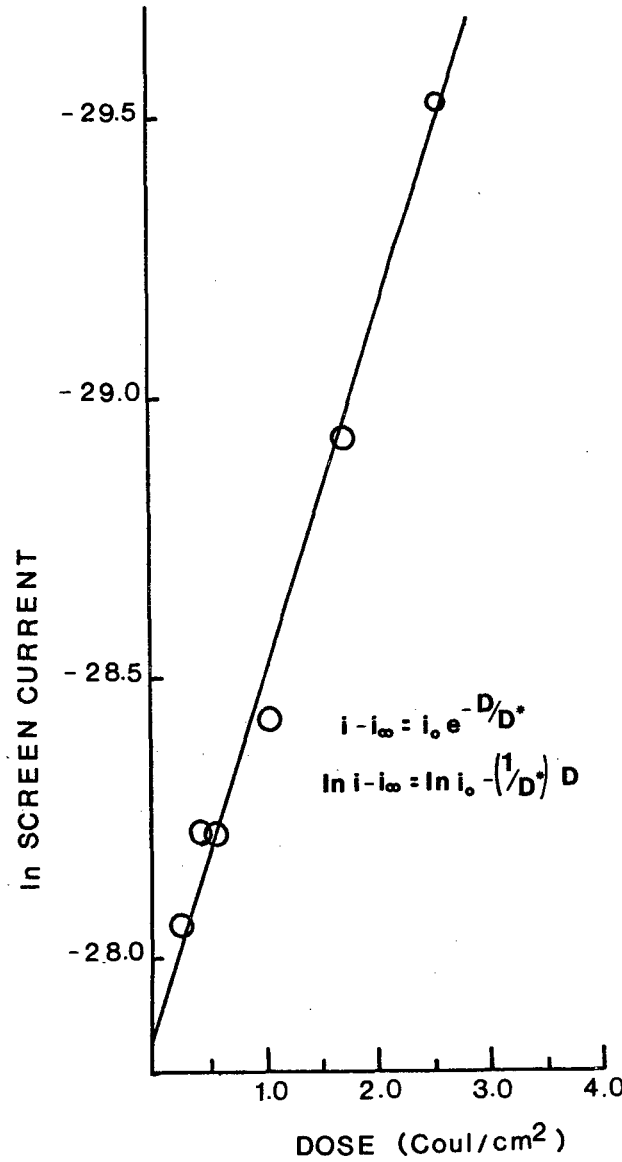


Figure 3.20: Determination of D^* for e_2-4 reflections from PBT 28555-25-4

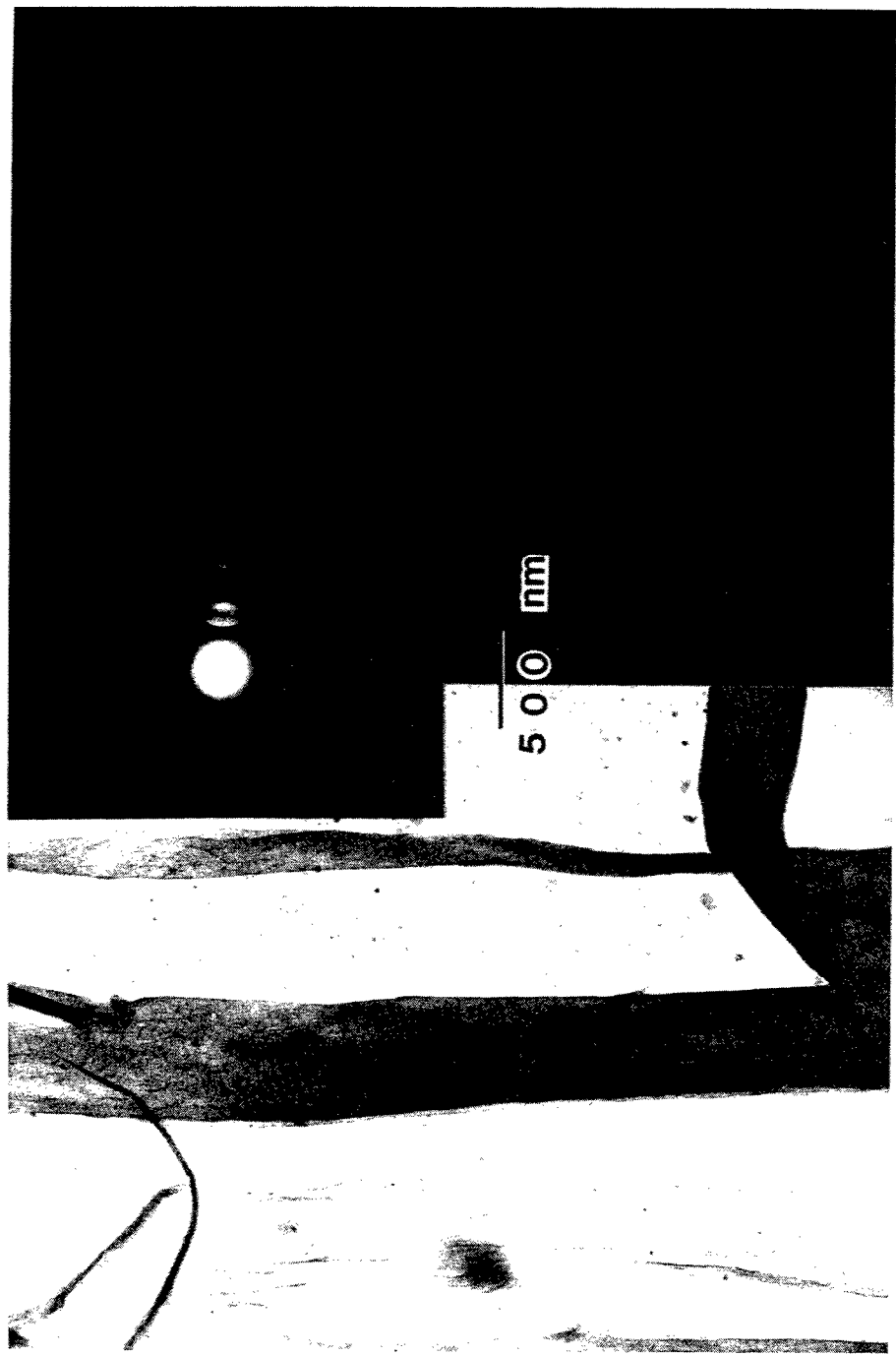


Figure 3.21: BF/DF pair from PBT 28555-25-4 annealed at 475°C prepared by detachment replication

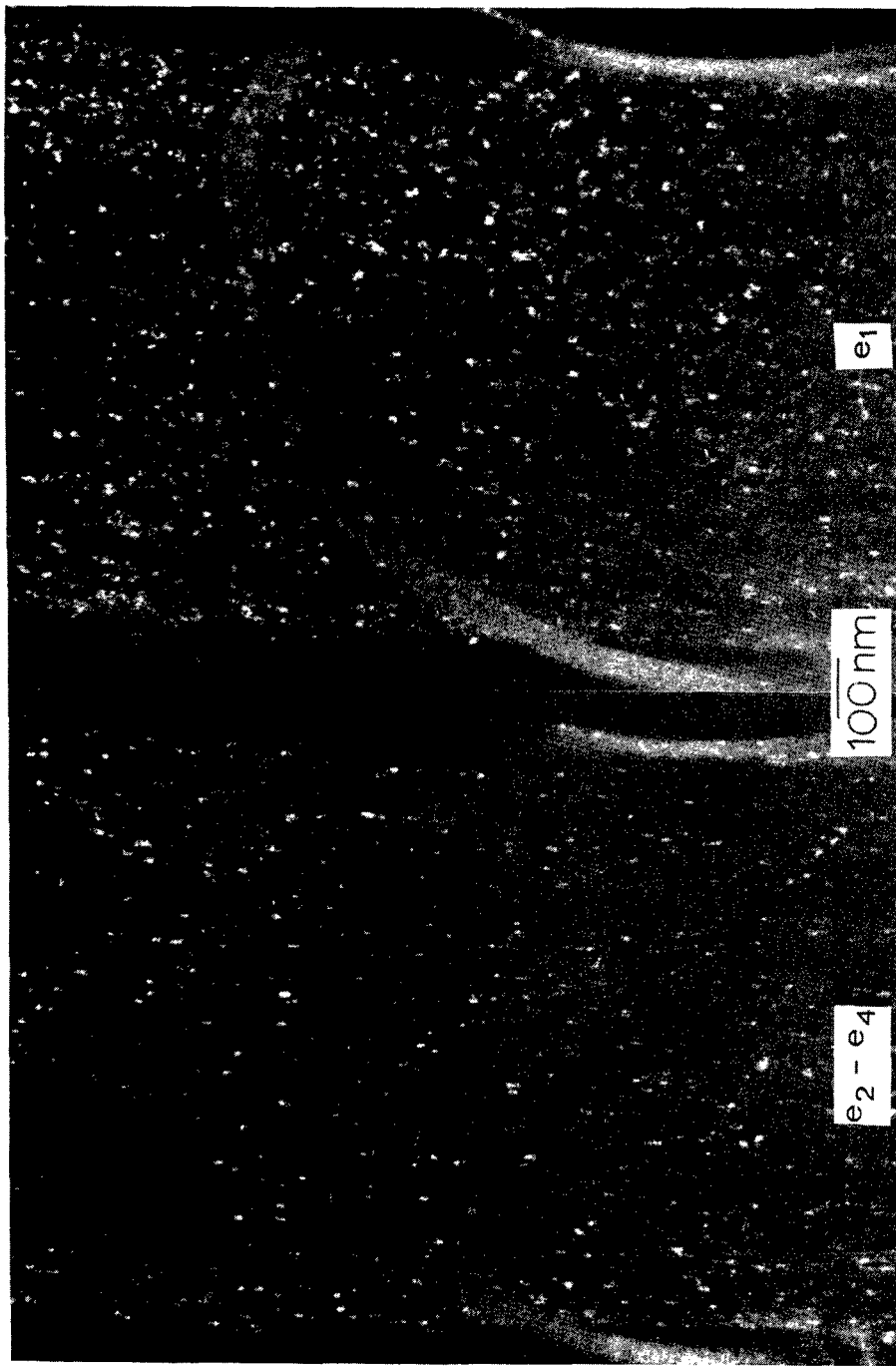


Figure 3.22: Successive DF images from e_1 and e_2-e_4 reflections
PBT annealed at 475°C

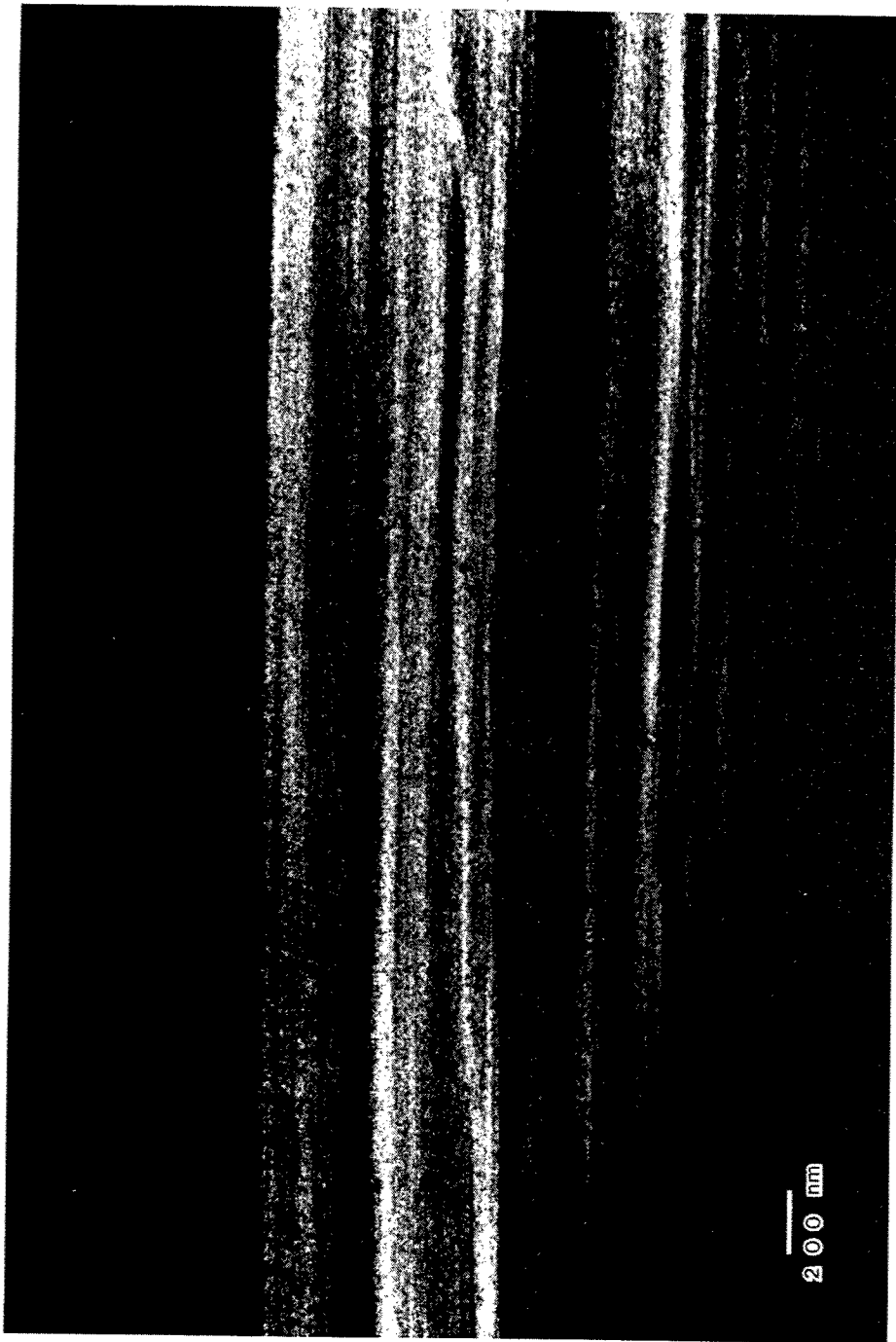


Figure 3.23: DF image from PBT 28555-19-2 as-spun

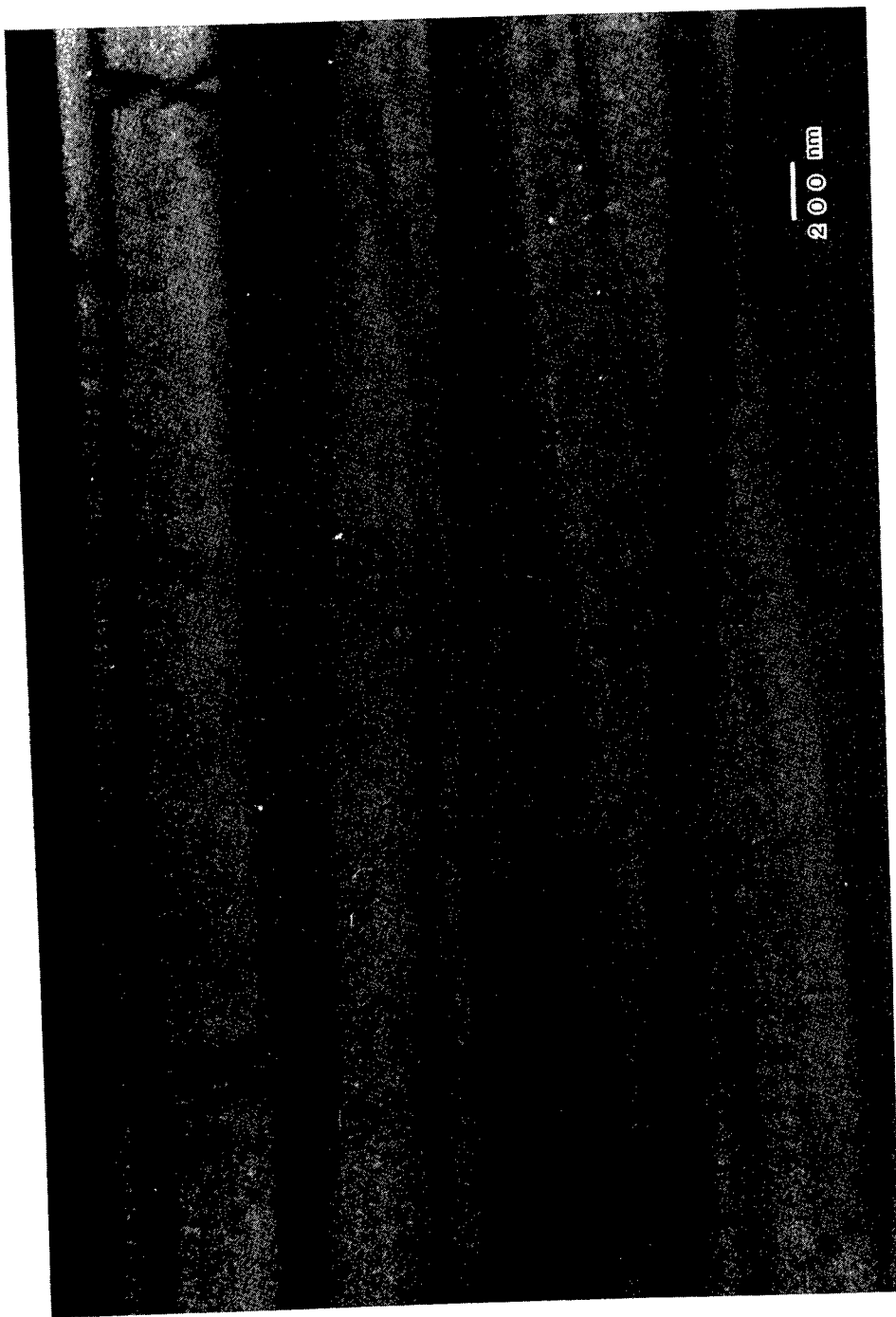


Figure 3.24: DF image from 28555-19-5 as-spun

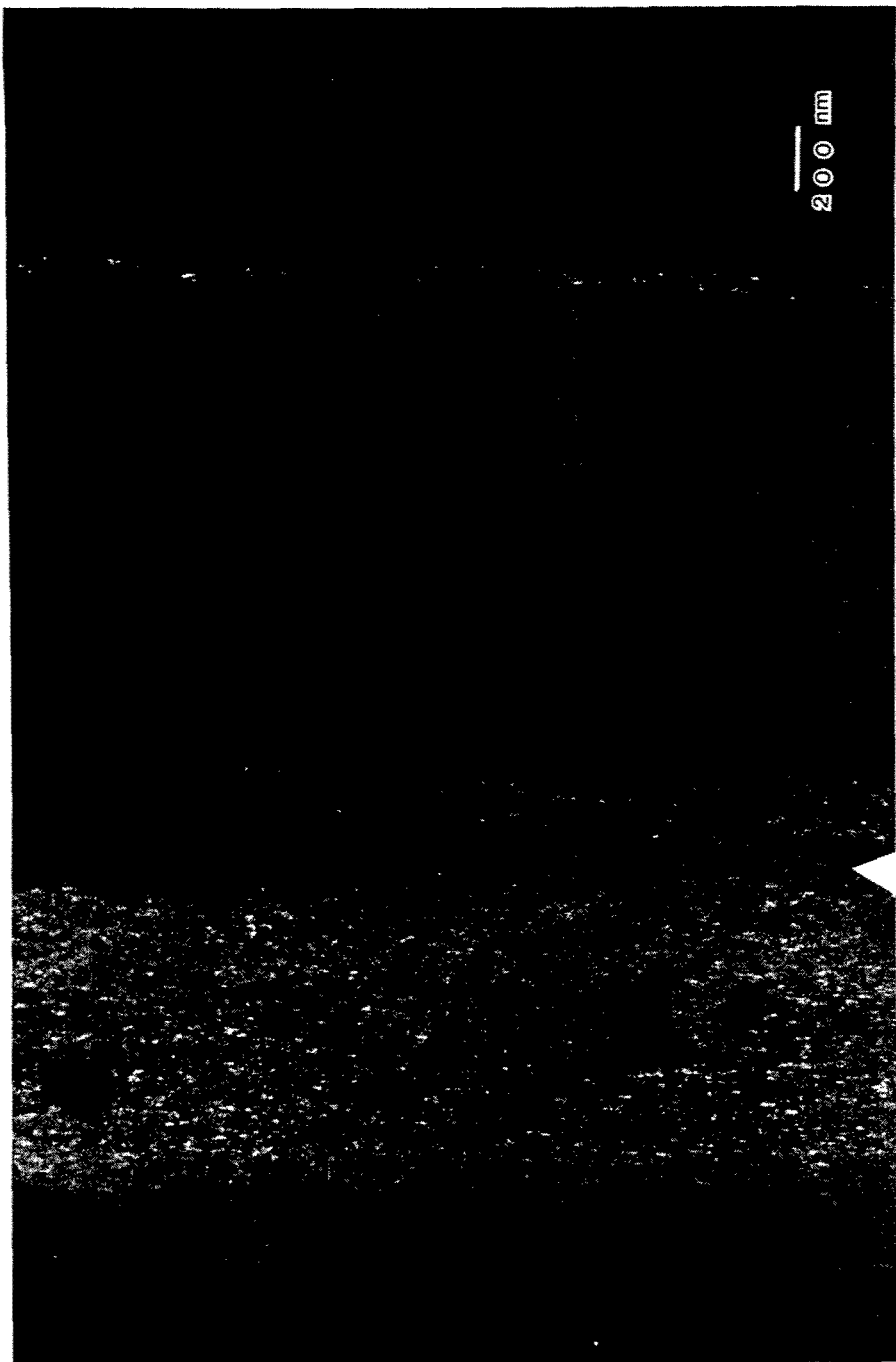


Figure 3.25: DF image from heat treated PBT 28413-40-1

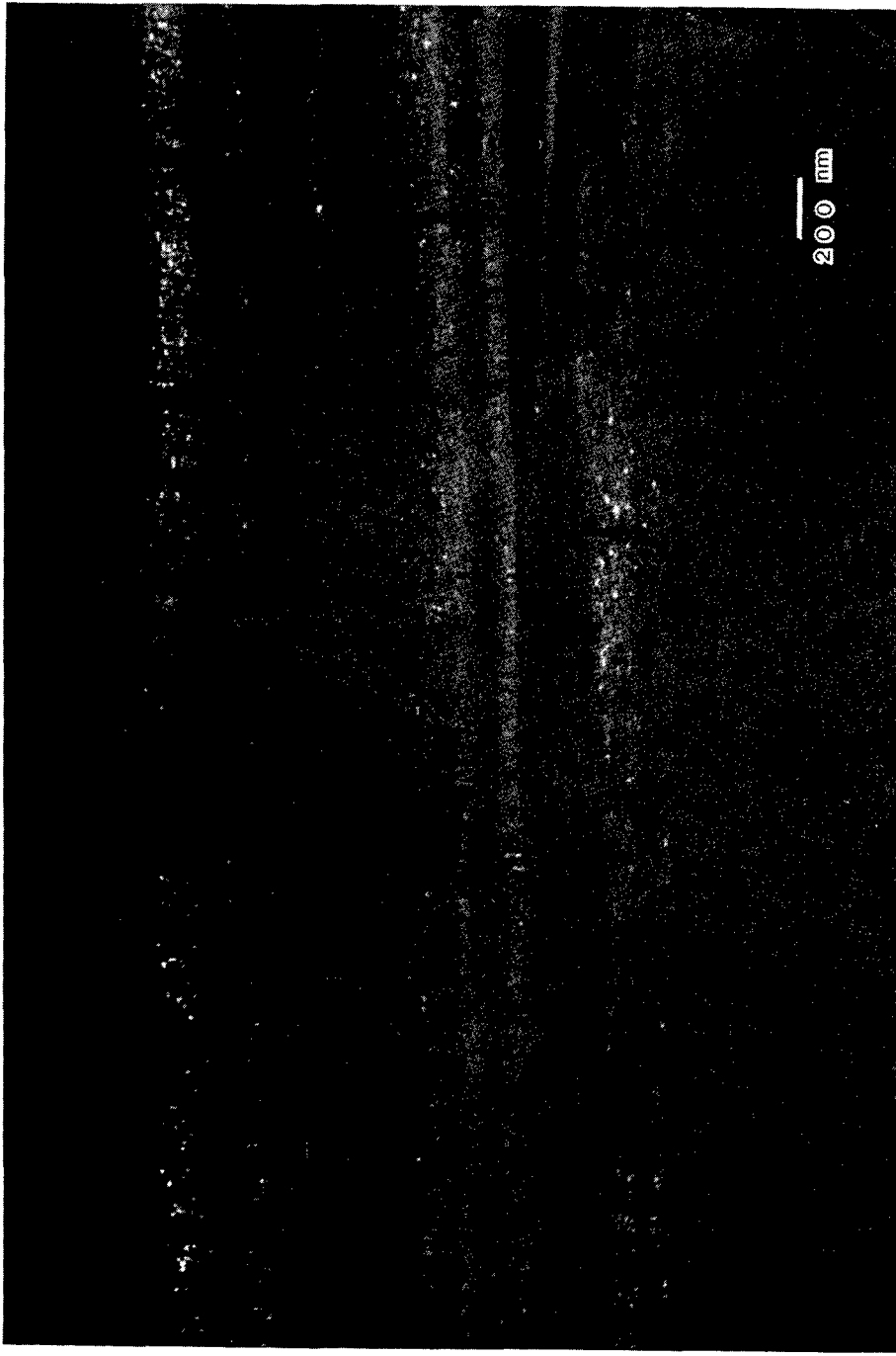


Figure 3.26: DF image from heat treated PBT 28413-40-4

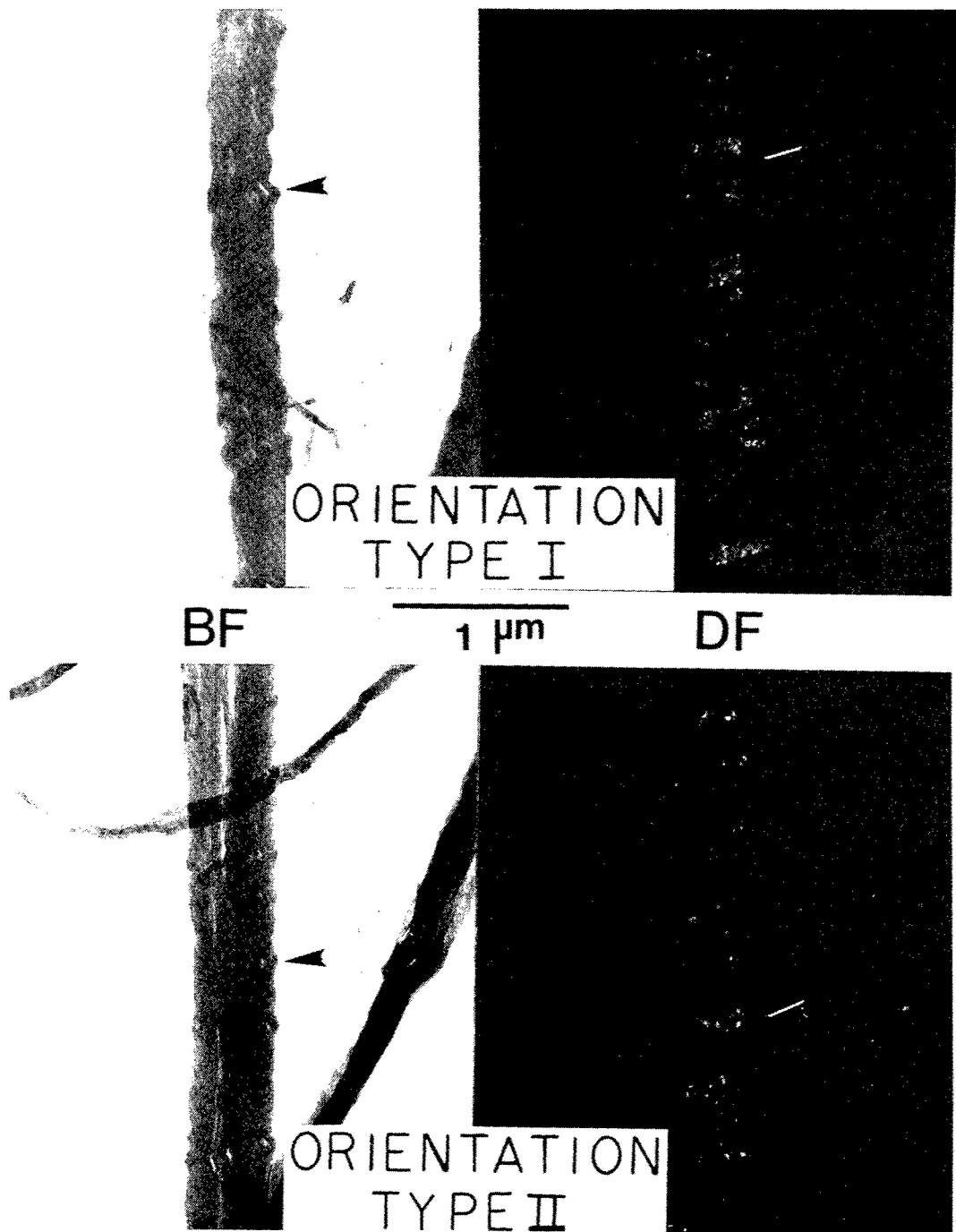


Figure 3.27: Kink bands observed in PBT fibers prepared by sonication

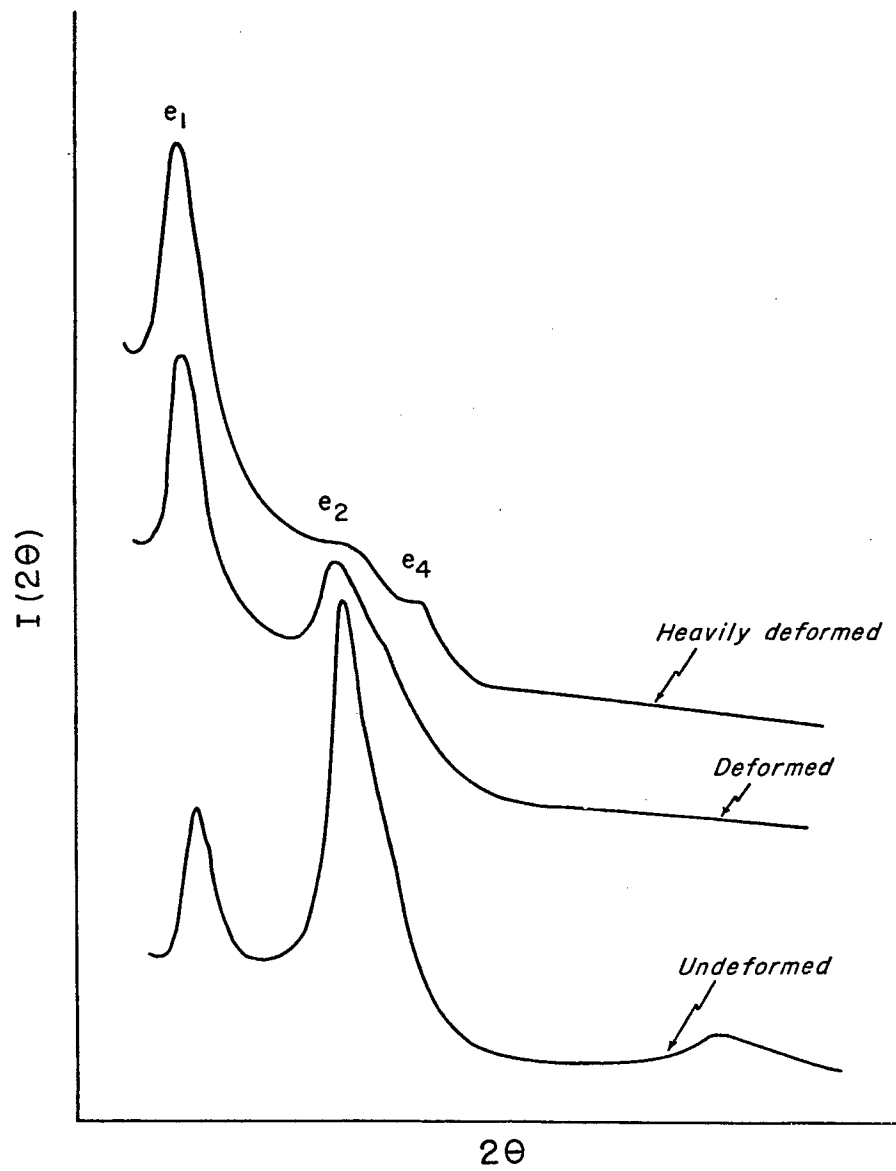


Figure 3.28: Microdensitometry of SAED from PBT 28413-40-1 rolled at 400°C

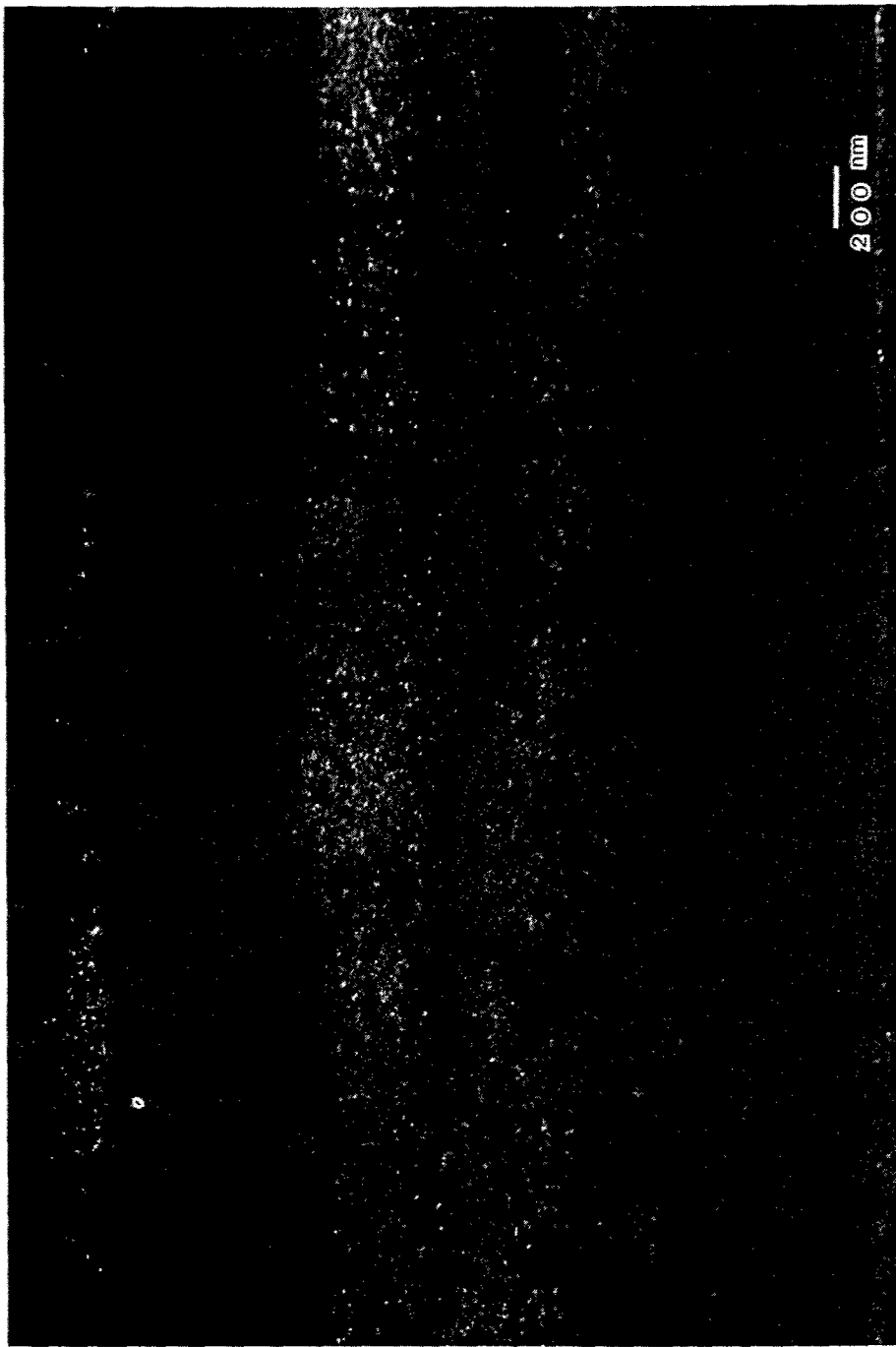


Figure 3.29: DF image from rolled specimen of PBT 28413-40-1 from e1

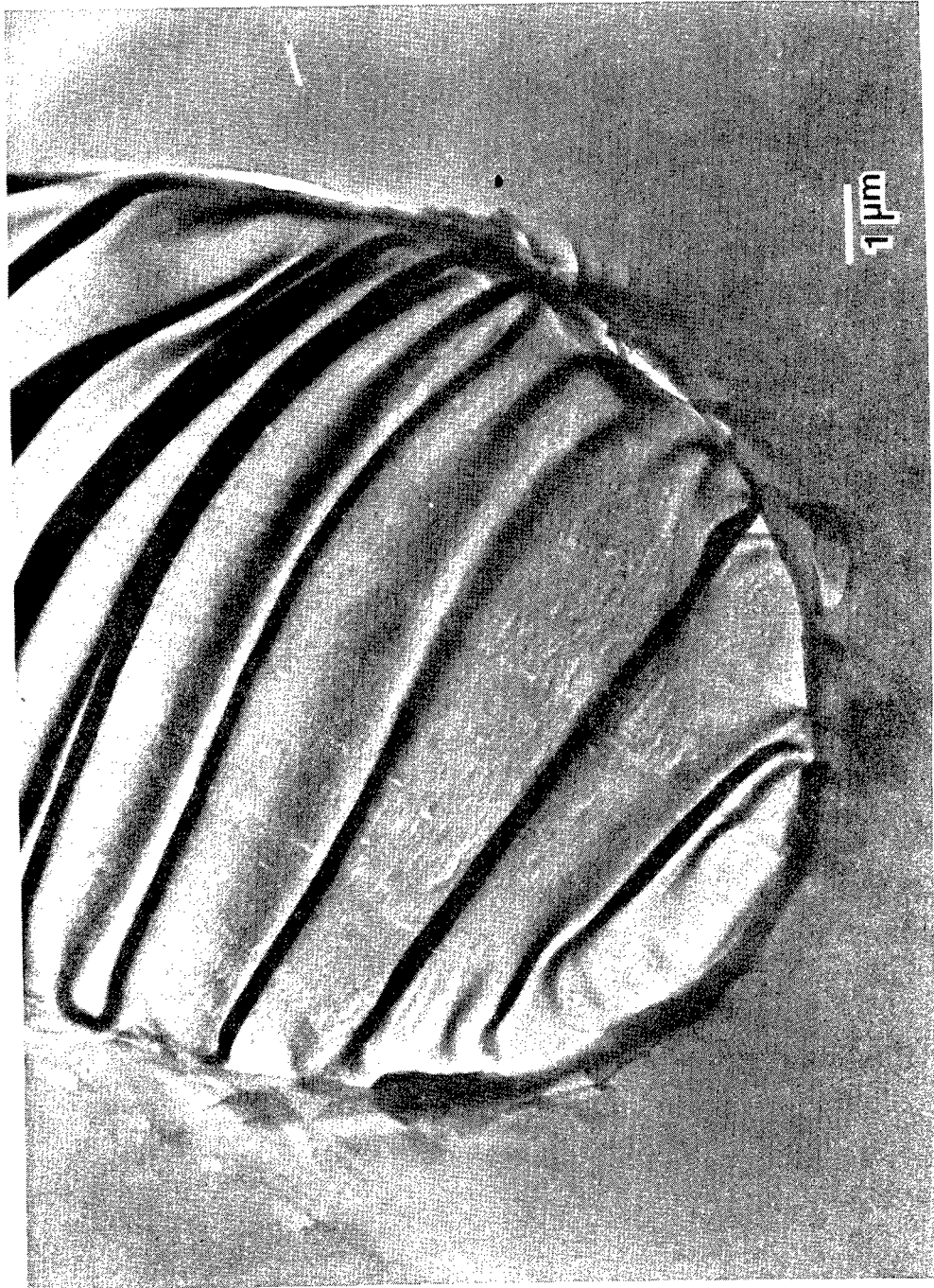


Figure 3.30: Microtomed section of PBT fiber embedded in epoxy

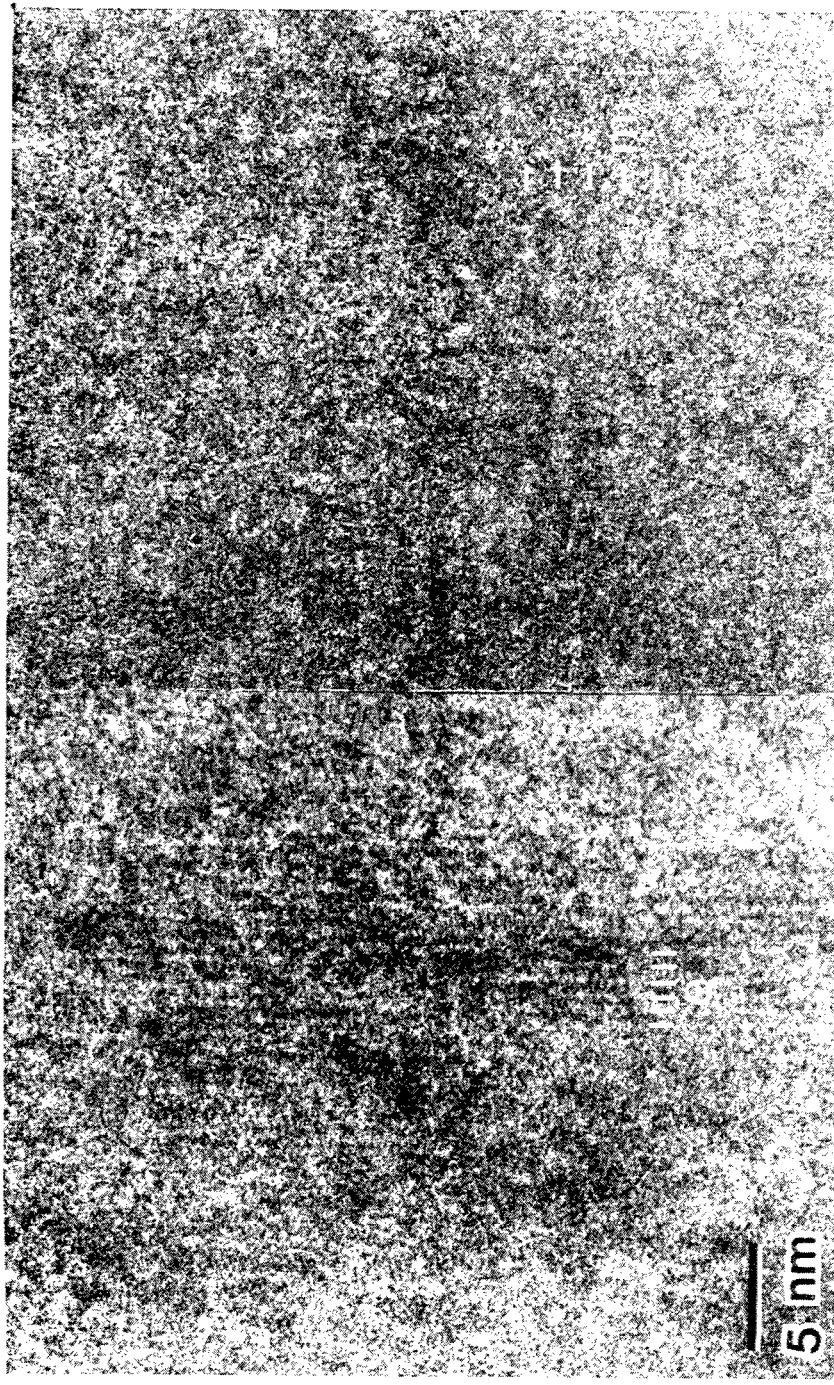


Figure 3.31: Axial bright field lattice image of PBT showing 5.8 \AA lattice spacing

PBT (AS SPUN)

SEQ. NO.
3109

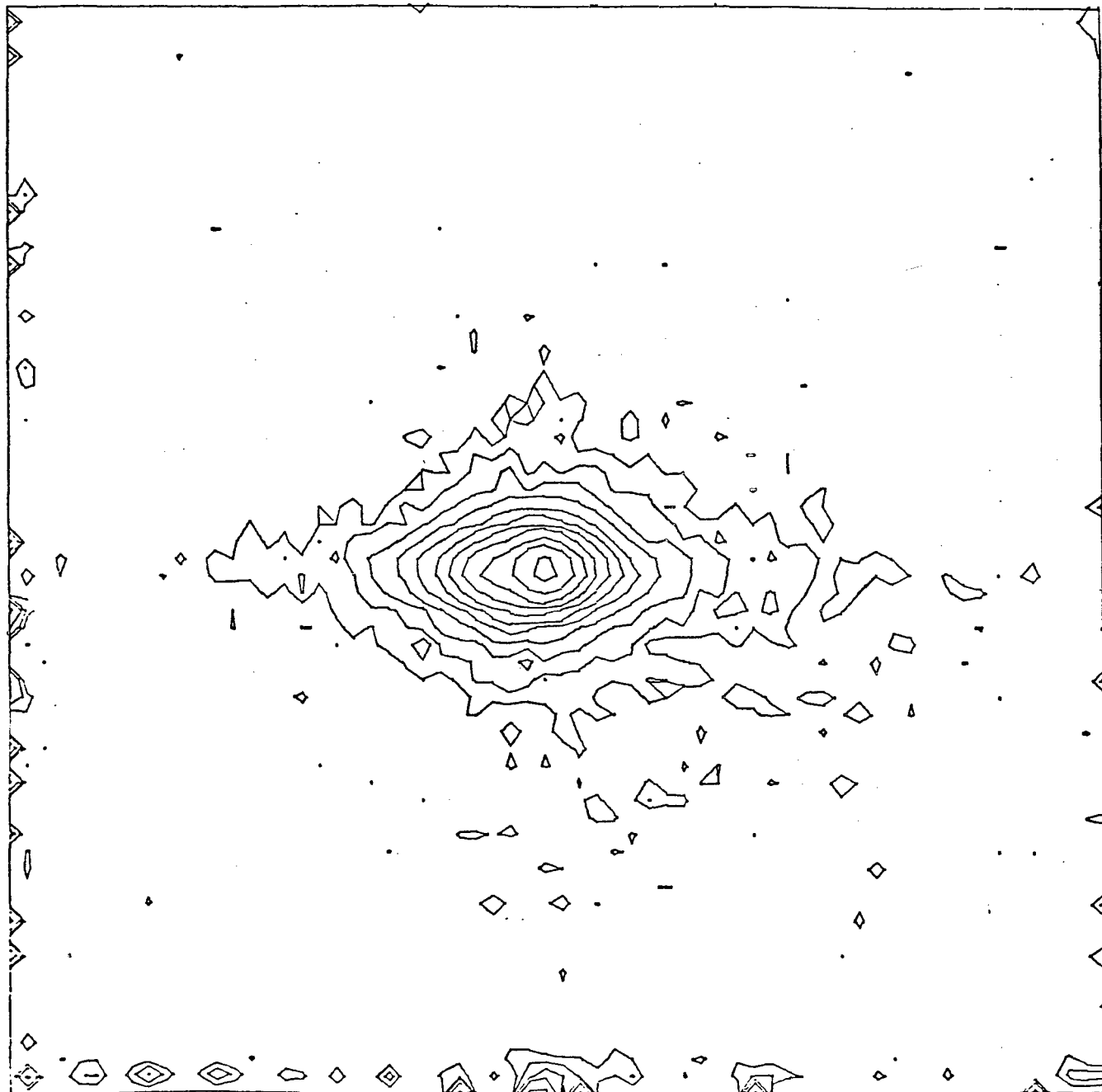


Figure 3.32: SAXS from as-spun PBT fibers (fiber direction vertical)

PBT (HEAT TREATED)

SEQ. NO.
3108

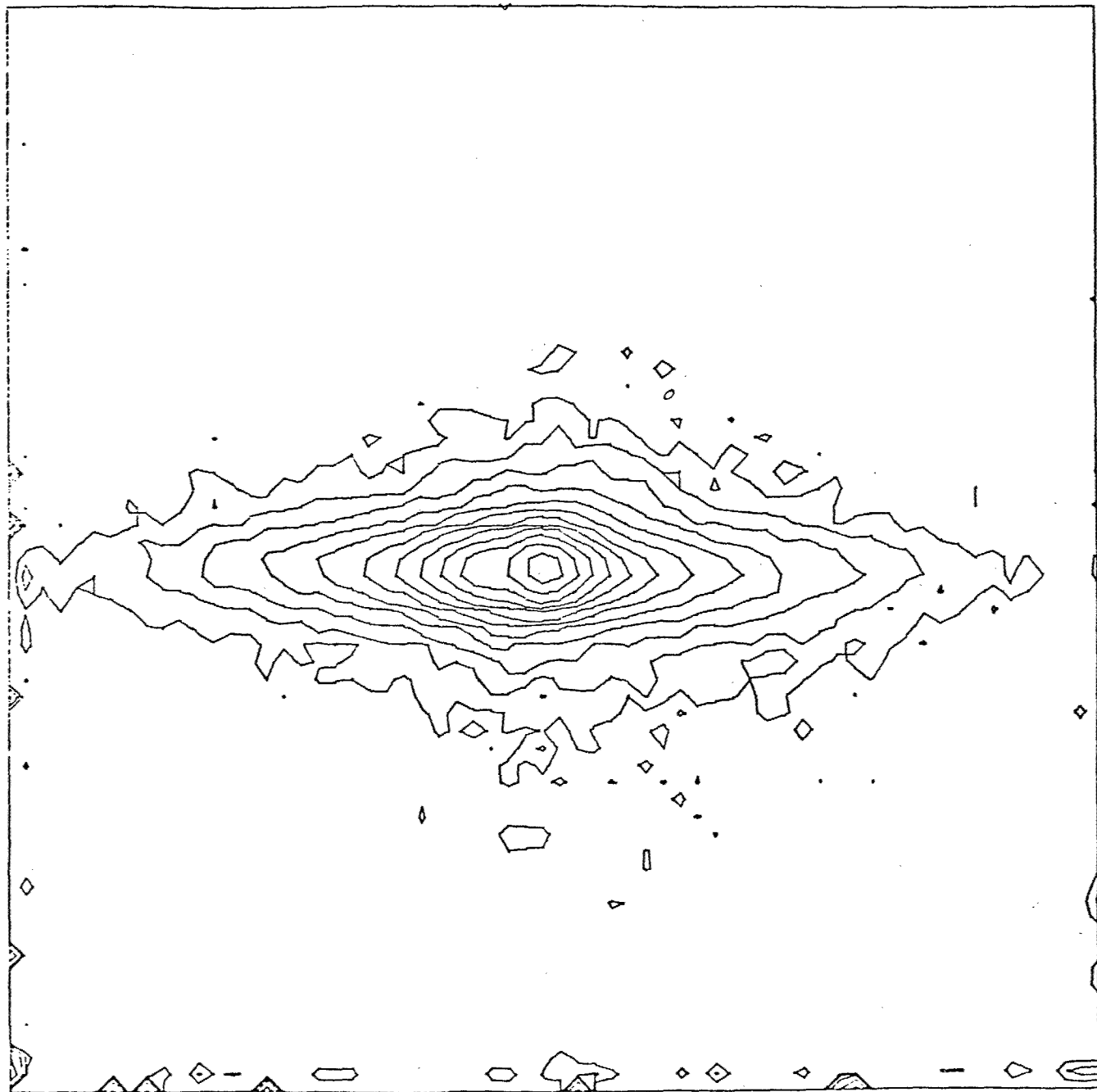


Figure 3.33: SAXS from annealed PBT fibers (fiber direction vertical)

SECTION 4: MECHANICAL PROPERTIES

4.1 Tensile Properties

The tensile mechanical properties of the as-spun and heat-set PBT fibers reported here were determined in compliance with ASTM D3379-75e Standard Test Method for Tensile Strength and Young's Modulus of High Modulus Single-Filament Materials. A Toyo Tensilon model UTM-II and an Instron Universal Testing Machine were used for the tensile tests to determine axial mechanical properties. A strain rate of 1% per minute was normally used. The typical tensile properties of PBT fibers are given in Table 4.1.

The morphological features of the fibers reported here are based on light optical and electron optical microscopy. Scanning Electron Microscopy (SEM) was done using an ETEC Autoscan operated at 20kV. Fiber samples for SEM observation were first sputter coated with a 350 Å layer of gold in a Polaron E5100 SEM coating unit to minimize charging problems. The interior fiber morphology was studied in two ways: (1) examination of fibers which were peeled longitudinally using needles and tweezers and (2) examination of the fracture ends of failed tensile tested samples.

4.2 Stress-Strain Behavior of As-Spun Fibers

Figure 4.1 schematically illustrates the non-linear stress-strain behavior observed for single filaments during tensile tests. The behavior shown is essentially that of an elastic-plastic body with strain hardening. Plastic deformations of roughly 1-3% were found for the filaments tested. The modulus of elasticity was seen to increase with re-extension after initial plastic

deformation. Qualitatively the same stress-strain behavior was obtained for all as-spun fibers.

4.3 Stress-Strain Behavior of Heat Treated Fibers

Heat treated PBT fibers have exhibited higher moduli, higher strengths, and lower elongations at break than the as-spun PBT fibers. The stress-strain behavior of free annealed (without tension or stretch) fibers is shown in Figure 4.2 for various annealing temperatures. For higher annealing temperatures lower elongations at break and higher moduli are achieved; however, the strength of the fibers is unaltered by free annealing. The overall stress-strain behavior of free annealed fibers is elastic-plastic as is the as-spun fiber, with the relative amount of plastic deformation being less the higher the anneal temperature. When tension is applied during the heat treatment the resulting fiber possesses a linear elastic stress-strain behavior as indicated in Figure 4.3. These fibers have been found to possess higher strengths and moduli as compared with the as-spun and free annealed PBT fibers.

4.4 Review of the Mechanical Behavior-Microstructure Observations

The morphology of both as-spun and annealed PBT fibers is of a fibrillar nature. The mechanically peeled fibers clearly illustrate this feature (see Figure 4.4). The length to width ratio of the fibrils is extremely large. Electron diffraction and wide angle x-ray diffraction studies indicate near perfect molecular orientation along the fiber axis. The composition of a microfibril would not consist of non-crystalline regions due to the extended chain of PBT molecules. Also slack or loose tie molecules in the structure would not be expected by similar reasoning.

Thus the structure of PBT fibers does not permit adequate description of the mechanical properties by conventional models [34].

The existence of a shear or slip mechanism to completely account for plastic deformation is unlikely for the PBT fibers. Due to the geometry of the fibrillar elements ($L \gg W$) the activation energy for a shear displacement process would be larger than the activation energy for rupture of the element. The slip mechanism by consecutive displacement of parts of fibrils is also unlikely by absence of amorphous areas in fibrillar elements. Also, the plastic deformation resulting from such shear displacement is normally much higher than the plastic deformation observed here. Materials which possess such a slip mechanism exhibit a decrease of their elastic limit upon annealing. Our results have shown an increase in the elastic limit and a decrease in the amount of plastic deformation upon annealing. In addition, no such plastic nature was observed for poly(p-phenylene terephthalamide) (PPTA) fibers which possess a similar type of fibrillar structure.

A modulus increase with plastic deformation and annealing also cannot be explained due to increased numbers of taut tie molecules or by orientation of amorphous regions. The small magnitude of plastic deformation suggests that molecular orientation and fibril aspect ratio changes would be negligible as far as modulus enhancement is concerned. The geometrical characteristics of the fibrillar elements ($L \gg W$) prevents mutual sliding and therefore the increased size of the laterally ordered regions during annealing should not lead to the change of elastic modulus in longitudinal direction. From these observations then, it is necessary to examine other possible models which will correctly

describe the observed mechanical behavior while being compatible with the observed structure.

4.5 Internal Stress Model

A structural model possessing internal stresses can be used to explain the mechanical behavior of both as-spun and heat-treated fibers. We first consider the reasons for residual stresses and some experimental evidence of the existence of internal stresses in fibers.

Formation of internal stress could arise during the coagulation step of the dry-jet wet-spinning process. The polymer dope filaments are roughly 10% PBT by volume. A substantial (~ 90%) volume change is required in going from the dope to the solid PBT fibers. As a dope filament enters the coagulation bath, the outer area or skin area is exposed to the coagulant immediately and the process of coagulation (and volume change) proceeds from the outside in. The interior or core of the fiber will, as a result, coagulate slightly later in time than the skin area. If the skin acquires sufficient mechanical integrity as it coagulates, it will tend to resist further shape changes which the core region requires as the core now begins to change in volume due to coagulation. The result of the fiber interior wanting to decrease dramatically in volume while the skin areas want to remain unchanged in dimension is the development of a high component of axial tensile stress in the core region and, for equilibrium, the development of compressive stresses in the skin region (Figure 4.5). Strong radial and hoop stresses are also produced during the shrinkage.

The presence of the voids and deformation bands are most likely caused by these high shrinkage stresses which develop during the fiber coagulation

process. Cavitation (voids) could be caused by the tensile failure of the partially coagulated core. As mentioned, the skin areas would be under the influence of axial compressive stresses and, because of the anisotropy of this material, compressive buckling could result in the circumferential banding observed in the fibers.

Residual or internal stresses in materials can be measured by observing changes in shape or strain in an object as a result of removal of part of the material. Residual stresses can also be measured by assessing the elastic strain in the crystal lattice by x-ray diffraciton. The small size and limited crystallinity of these PBT fibers makes such experiments difficult to perform. Instead of trying to cut away a piece of the fiber, we attempted to selectively destroy a section of the fiber using a laser. The change in fiber shape resulting from this damage could then be easily observed by optical microscopy.

PBT fibers were placed in a laser beam so as to permit damage to occur in a region near the fiber surface. This is equivalent to the release of compressive internal stress in the skin of the fiber (see Figure 4.5). Such a relief of a portion of the internal stress would result in bending of the remainder of the structure with the damage region on the concave side. Figure 4.6 illustrates a damaged PBT fiber showing the damaged region on the concave side. PPTA fibers and heat treated PBT fibers which display linear elastic stress-strain curves (and are, therefore, assumed to be free of residual stress) showed no warpage from this burning technique. Thus, the laser burning technique has provided a qualitative measure of internal stress in as-spun PBT fibers.

4.6 Mechanism of Plastic Deformation

A structural model possessing internal stress, such as depicted in Figure 4.7, can be used to explain an apparent elastic-plastic behavior. Consider four rods all having the same elastic properties but originally of different lengths - the two outer rods having the same length but being longer than the central rods. If the rods are constrained to have the same length (different from the original lengths), internal stress is produced: tensile forces in the center rods and compressive forces in the outer rods. If this elementary model for fibers with internal stress is now deformed, and its stress-strain behavior observed, it is found to exhibit an apparent plastic behavior. This apparent plastic behavior is the result of the redistribution of forces when the center rods reach their critical breaking load and fail. In other words, because of the initial internal stresses the four rods do not act identically and failure of the central rods precedes complete structure failure giving an apparent plastic behavior. If some distribution of internal stress is assumed across the fiber cross-section, a smooth elastic-plastic stress-strain curve can be predicted.

This fiber internal stress model attributes the deviations from linear-elastic behavior to the fracture of fibrillar elements which have a higher tensile stress as a result of the applied load plus original internal stress. The plastic part of the stress-strain curve, then is the result of the continual consecutive fracture of overstressed elements in the fiber. Because the fibrillar elements do not act cooperatively as far as fracture is concerned, the overall fiber strength is less than an identical fiber with no internal stress.

This internal stress model, while able to explain an elastic-plastic type of

behavior, is still inadequate because it is not able to explain an increase in observed modulus with plastic deformation.

4.7 Increase of Elastic Modulus During Plastic Deformation

An elastic-plastic behavior with increasing modulus can be demonstrated by a modified internal stress model (see Figure 4.8). In this model the compressive internal stresses are high enough to have caused buckling of the outer rods of the model structure. If this structure is now deformed, its stress-strain behavior exhibits an elastic-plastic nature with increasing modulus.

During loading the deformation behavior of such a system will be similar to the previous one with the difference that in the process of plastic deformation the straightening of initially buckled elements takes place (see Figure 4.8). During unloading, friction forces are enough to prevent sliding between fibrils and therefore the elastic modulus of unloading will correspond to the effective modulus of a structure with continuous elements. The compliance of straight fully extended fibrillar elements is lower than buckled ones and explains the increase of elastic modulus of the system caused by plastic deformation.

The existance of buckled elements in the initial structure (as-spun fiber) and the tranformation of buckled elements into straight elements during plastic deformation is documented by scanning electron microscopy investigations.

Figure 4.9 shows the micrographs of as-spun and plastically deformed PBT fibers. It can be seen that the surface of an as-spun fiber contains a number of kink type defects while the surface of a plastically deformed fiber is rather homogeneous. The micrographs of peeled fibers (see Figure 4.10) show that these defects are not purely surface type, but the kink elements go entirely through the outer region of cross section of the as-spun fiber.

4.8 Change of Mechanical Properties with Annealing

The forces preventing the relief of residual stresses (σ_i) are the forces of interaction between fibrils. If the stress necessary to move a fibrillar element relative to its neighbors is ψ , then the value of residual stress should satisfy the following inequality:

$$\sigma_i \leq \psi \quad (1)$$

The value of interfibrillar interaction, ψ , is proportional to the surface area of the fibril. It is natural to assume that this interaction is also dependent on temperature:

$$\psi = \psi(T, L, r) \quad (2)$$

where L is the fibril length and r is the parameter describing the cross sectional area. If the annealing is done at a sufficiently high temperature, T_0 , then the value of the maximum internal stress in the material is determined by:

$$\sigma_i^{(\max)} = \psi(T_0, L, r) \quad (3)$$

The value of the elastic limit in the previously described model corresponds to the onset of fracture of overstressed structural elements,

$$\sigma_b = \sigma_i^{(\max)} + \sigma_y \quad (4)$$

where σ_b is the tensile strength of the fibril and σ_y is the stress at the elastic limit. Figure 4.11 shows that the elastic limit depends linearly on the annealing temperature and therefore, in correspondence with equation (3), the force of interfibrillar interaction is also a linearly decreasing function of temperature.

Annealing, therefore, leads to a reduction of the internal stress and explains the decrease in the strain at break with annealing. The strain at break ϵ_b is determined by the maximum value of deformation of the initially compressed elements, i.e.

$$\epsilon_b = \epsilon_0 + \epsilon_c \quad (5)$$

where ϵ_0 is the strain at break of a fibrillar element in the absence of residual stress and ϵ_c is the strain of compression caused by the presence of the initial internal stress. During annealing the value of the internal stress is decreased with increased annealing temperature thereby decreasing ϵ_c and explaining the decrease in strain at break with annealing temperature. The increase of elastic modulus with annealing temperature, as well as with plastic deformation, can be explained by the straightening out of buckled elements. The reduction of forces of interaction between fibrils with increased temperature makes possible their mutual displacement under the action of internal stresses, thus allowing for the straightening out of bent elements. As can be seen from equation (3), during annealing in the absence of external forces, internal stresses cannot be released completely because of a finite ψ up to the temperature of destruction of the fibrillar structure. For this reason, in spite of the lowering of internal stresses, the mechanism of fiber fracture remains the same as in the as spun fibers. Because the fibrillar elements do not act cooperatively, the consecutive fracture of elements occurs and the fiber strength remains essentially independent of annealing temperature.

On the other hand, because of the finite length of fibrillar elements where load transfer is through shear, in presence of an external load during annealing

equation (3) becomes:

$$\sigma_i(\max) + \sigma_{\text{appl}} = \psi(T_0, L, r) \quad (6)$$

where σ_{appl} is the stress caused by the external tensile load. If the value of the external load at a particular annealing temperature satisfies the condition:

$$\psi(T_0, L, r) - \sigma_{\text{appl}} = 0 \quad (7)$$

then the complete release of internal stress is possible at a non-zero value of the interfibrillar force of interaction. The mechanism of fracture becomes quite different since now fibrillar elements act cooperatively. In this way, annealing in the presence of an appropriate external tensile force leads to complete release of internal stress which in turn leads to the essential increase of fiber strength (see Figure 4.12).

Since the dependence of interfibrillar interaction forces on the annealing temperature can be found (in accordance with the internal stress model) from the dependence of the elastic limit on annealing temperature, then equation (7) permits the determination of conditions necessary for the complete release of internal stress (see Figure 4.12), i.e. to determine the minimum value of the external tensile force in correspondence with the chosen value of the annealing temperature. Obviously, the upper bound for the external load should be the value of the elastic limit (σ_y) for the as-spun fiber (i.e. the case where the fiber would be damaged by the fracture of initially overstressed fibrillar elements) and the upper bound for the annealing temperature is determined by the onset of thermal degradation (see Figure 4.12).

4.9 Fatigue Properties

The tension-tension fatigue study was carried out on a vibron dynamic

viscoelastometer (Toyo Measuring Instruments Company), with modifications to allow the measurement of steady load. A working gauge length of 20 mm was chosen for the experiments. Samples were tested at different levels of steady load, F_0 (see Figure 4.13). The value of dynamic force, F_d , was 6.3 gm and cycling frequency was 110 Hertz. The tests were conducted at room temperature.

4.10 Fatigue Properties of Heat Treated Fibers

Heat treated PBT-27554-42-2 fiber appears to behave during the fatigue test like a perfectly elastic material. The dissipation factor ($\tan \delta$) was found equal to 0, and the dynamic modulus of elasticity was found equal to the static value (approximately 1500 gm/denier).

The number of cycles to failure is in the following ranges: for $F_0 = 15$ gm, from 0 to 18×10^6 cycles, and for $F_0 = 10$ gm, from 0.4×10^6 to 30×10^6 cycles. A distribution curve constructed from the results of 15 tests ($F_0 = 15$ gm) is shown in Figure 4.14. The large range in the experimental data and the nonsymmetry of the distribution curve can be explained, first of all, by the difference in strength properties of particular filaments, which also is seen in the tensile tests. The fact that the fatigue lifetime of some specimens tested at $F_0 = 10$ gm was smaller than the fatigue lifetime of specimens tested at $F_0 = 15$ gm shows that the method of mounting and/or application of load in the apparatus is critical.

The average values of fatigue lifetime were determined by two methods: (A) arithmetic average $\{N\}_A$, and (B) maximum of the curve of the distribution $\{N\}_m$ (see Figure 4.14) and were found to be:

for $F_0 = 10$ gm: $\{N\}_A = 16 \times 10^6$ cycles, $\{N\}_m = 26 \times 10^6$ cycles

for $F_0 = 15$ gm: $\{N\}_A = 6 \times 10^6$ cycles, $\{N\}_m = 10.5 \times 10^6$ cycles

Taking into account the factors influencing the strength of the particular specimens, it seems that the average $\{N\}_m$ should better characterize the fatigue lifetime of the material than the average $\{N\}_A$. The range of fatigue lifetime data for the specimens prepared from the same fiber filament is much narrower than for the set of specimens prepared from different fiber filaments. The experiments on simple tensile failure allow one to select the filament from the yarn of typically 5 filaments, which has the most representative strength properties for that given set of fiber filaments. By this procedure, the average value $\{N\}_A$ is practically the same as the average $\{N\}_m$ determined on a set of specimens obtained by random choice from all filaments of the fiber. In order to reduce the number of tests, the following fatigue experiments concentrated on fiber filaments previously selected by simple tensile failure testing.

4.11 Fatigue Properties of As-Spun Fibers

To ascertain the influence of heat treatment on fatigue behavior of PBT fibers the fatigue tests on as-spun PBT-27554-33-5-255 fiber, which is the precursor of heat treated PBT-27554-42-2 fiber were carried out. The value of steady load was equal to 12 gm. Five specimens were tested and the average value of fatigue lifetime was found equal to 0.8×10^6 cycles.

It is known [35] that one of the main factors influencing on the fatigue lifetime of the particular fiber is the ratio of the value of maximum load, P_{max} , in fatigue test to the value of force at break, P_B , in the simple tension test. Therefore, it seems reasonable for the fibers characterized by different values of strength in tension, to compare their fatigue properties at the same values of the ratio P_{max}/P_B , rather than at equal values of maximum load. In this way, the data obtained for as-spun fibers should be considered relative to

the data obtained for heat treated fibers at mean load value equal to 15 gm. Such a comparison shows that heat treatment leads to an approximate 13 fold increase of fatigue lifetime of PBT fibers.

4.12 Torsion Tests

The character of deformation of PBT fibers (PBT-27554-42-2) in twisting was determined by the measurement of elastic component of shear strain during twisting of the fiber filament. The diagram (see Figure 4.15) shows the dependence of elastic component of shear strain, γ (shear strain referred to the surface layer of the fiber material). The dotted line corresponds to the behavior of an ideally elastic material, i.e., if the whole strain is completely reversible. Up to about a 5% strain, correspondently to π radians of twist angle per mm of fiber length, the strain is elastic. However, further twisting causes the strain to become partially irreversible and for large angles of twist, the main part of strain is irreversible. In spite of the fact that in tension fracture occurs at small deformation, brittle fracture in twisting was not observed, indicating high fiber anisotropy.

The influence of twist on tensile strength of PBT fibers was also studied. The fiber filaments were given preliminary twisting and then pulled in tension up to failure. The results are shown in Figure 4.16, where γ is the shear strain referred to the surface layer of the fiber filaments and F_b is the tensile strength in grams.

If the shear strain is less than 25% (corresponding to 3 turns per mm for fiber length), the influence of twist on tensile strength is not observed and consequently this value can be considered as a limit of safe twisting. However, larger twist leads to reduction (up to 60%) of the tensile strength of the

fiber.

SEM of the fracture surface (see Figure 4.17) shows that fracture occurs by axial splitting, with splits being longer than in simple tension test.

4.13 Environmental Effects

The effect of various environments on the mechanical properties of PBT-9-10 (5.3 denier fiber) has been studied over periods of up to 155 days. Fiber samples were placed in sealed containers of various liquid environments and removed at various times, water washed, then mounted for regular tensile testing under room conditions. Mechanical properties are reported on a weight basis using the original untreated fiber denier. The environments studied were petroleum ether (Skelly F), chloroform, dimethylacetamide (DMAc), sulfuric acid, nitric acid, acetone and water. Samples were tested after the following time periods: 3 hours, 1, 4, 8 and 155 days. Values of fiber modulus, strain at break and strength for the DMAc, Skelly F, H_2SO_4 and water environments are summarized in Figures 4.18 - 4.20.

Fibers placed in chloroform, acetone and nitric acid were only studied up to an 8 day period. Chloroform and acetone environments showed effects equivalent to the DMAc and Skelly F environments for these times. The nitric acid environment reduced the strain at break about the same as did the sulfuric acid but did not reduce the modulus or strength as drastically. The figures indicate that over the 8-day period, the mechanical properties are approximately unchanged for all but the two acid environments. Over 155 days only modulus remains fairly unchanged for the same environments.

The retention of mechanical properties of as-spun PBT fibers has been found to be extremely good after exposure to a variety of harsh chemical environments.

After 200 exposure hours to all but the strong acid environments, essentially 100% retention of both modulus and strength was observed. The strong acid environments show immediate effects of deterioration of the fiber mechanical properties.

Table 4.1 Mechanical Properties of Selected Fibers

Fiber	Apparent Modulus [g/d]	ϵ_b [%]	T_b [g/d]
As-Spun			
28555-19-2	500	3.5	12.5
-19-3	380	4.8	12.3
-19-4	500	4.3	12.9
-19-5	300	5.8	11.9
Heat Treated			
28413-40-1	550	2.1	10.8
-40-2	550	2.1	11.5
-40-3	400	2.0	7.6
-40-4	1170	1.6	18.2
-40-5	770	1.6	9.9
-40-6	860	1.6	12.5
-40-7	800	1.5	11.0

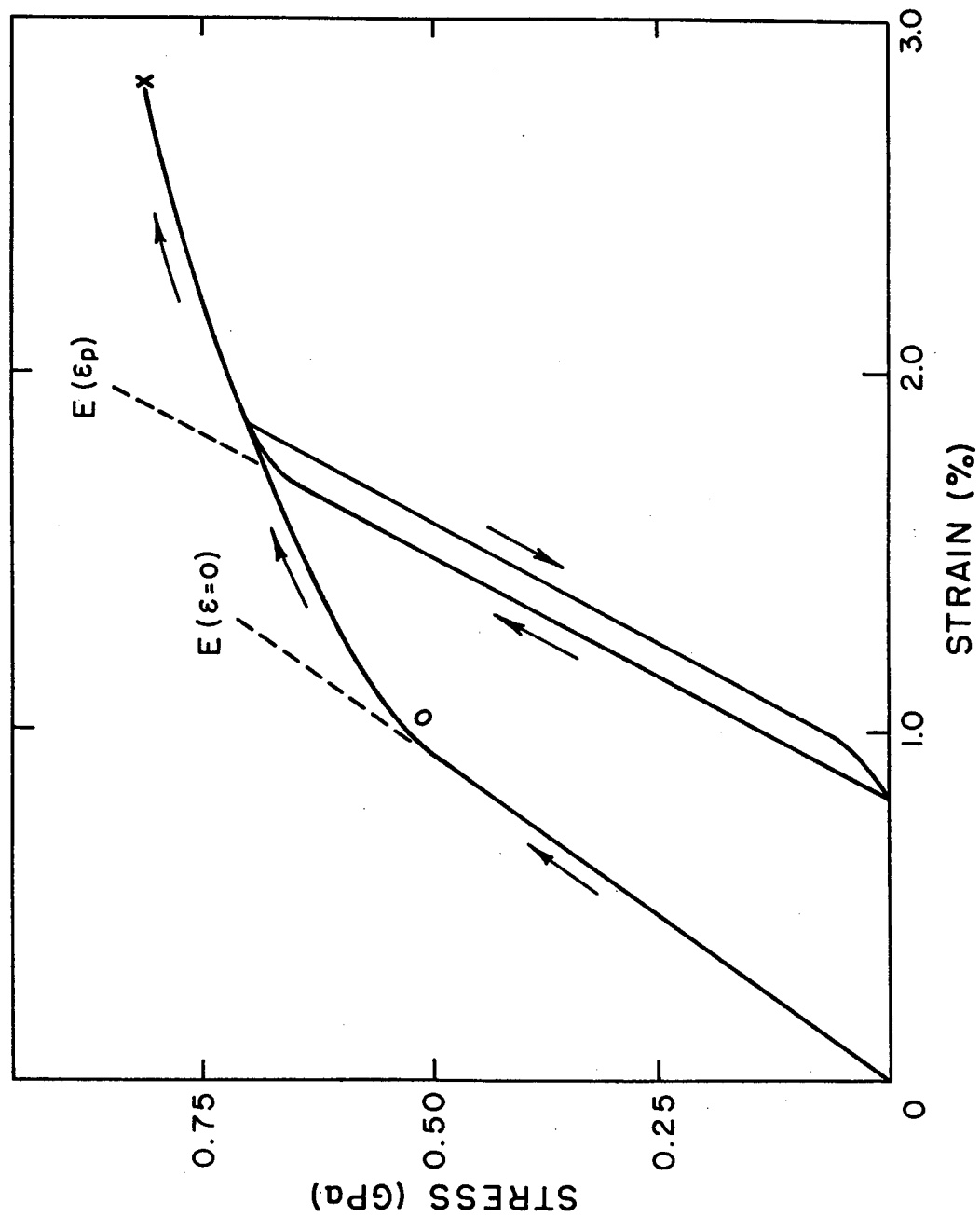


Figure 4.1: Stress-strain behavior of as-spun PBT fibers

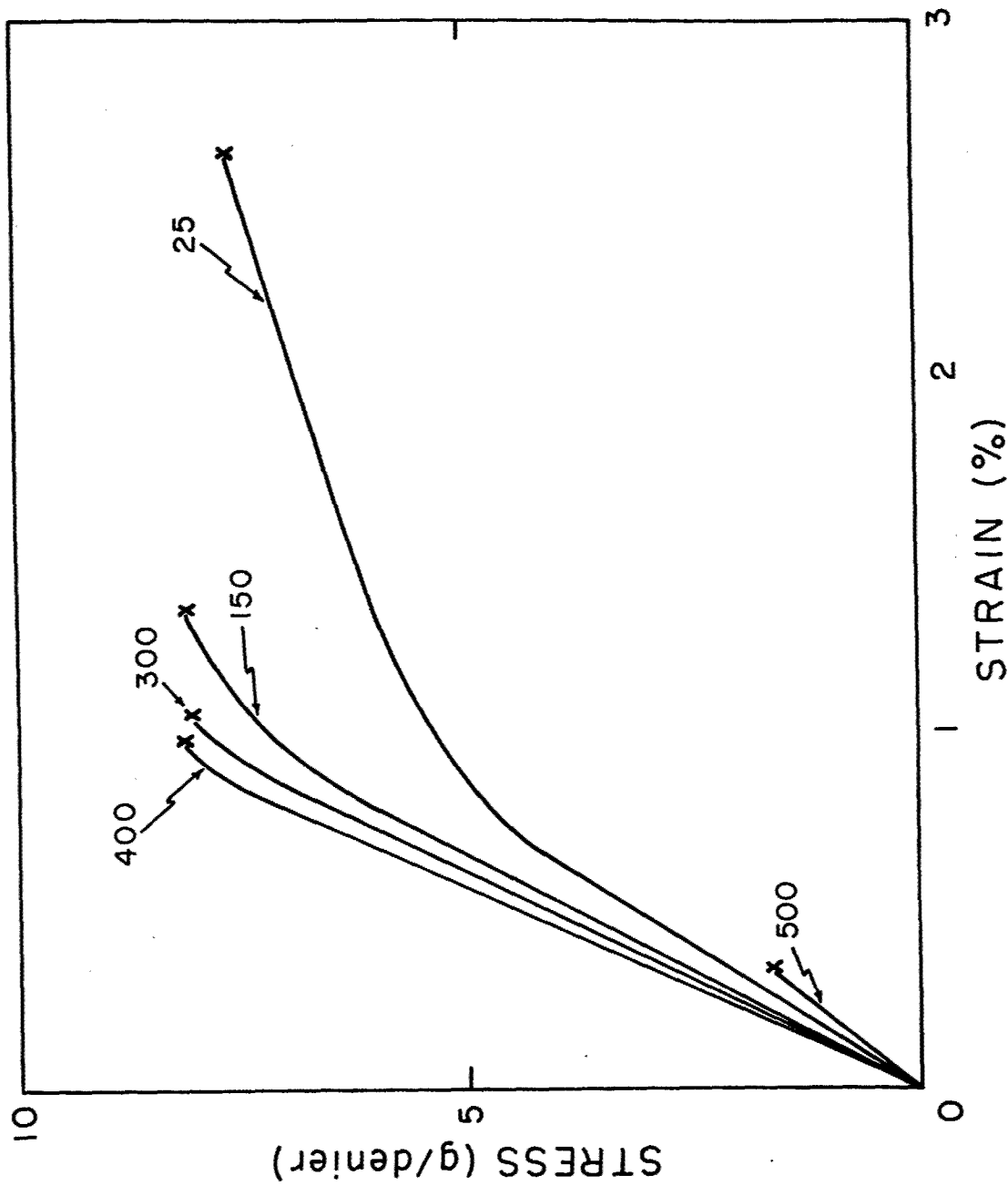


Figure 4.2: Stress-strain behavior of free annealed fibers

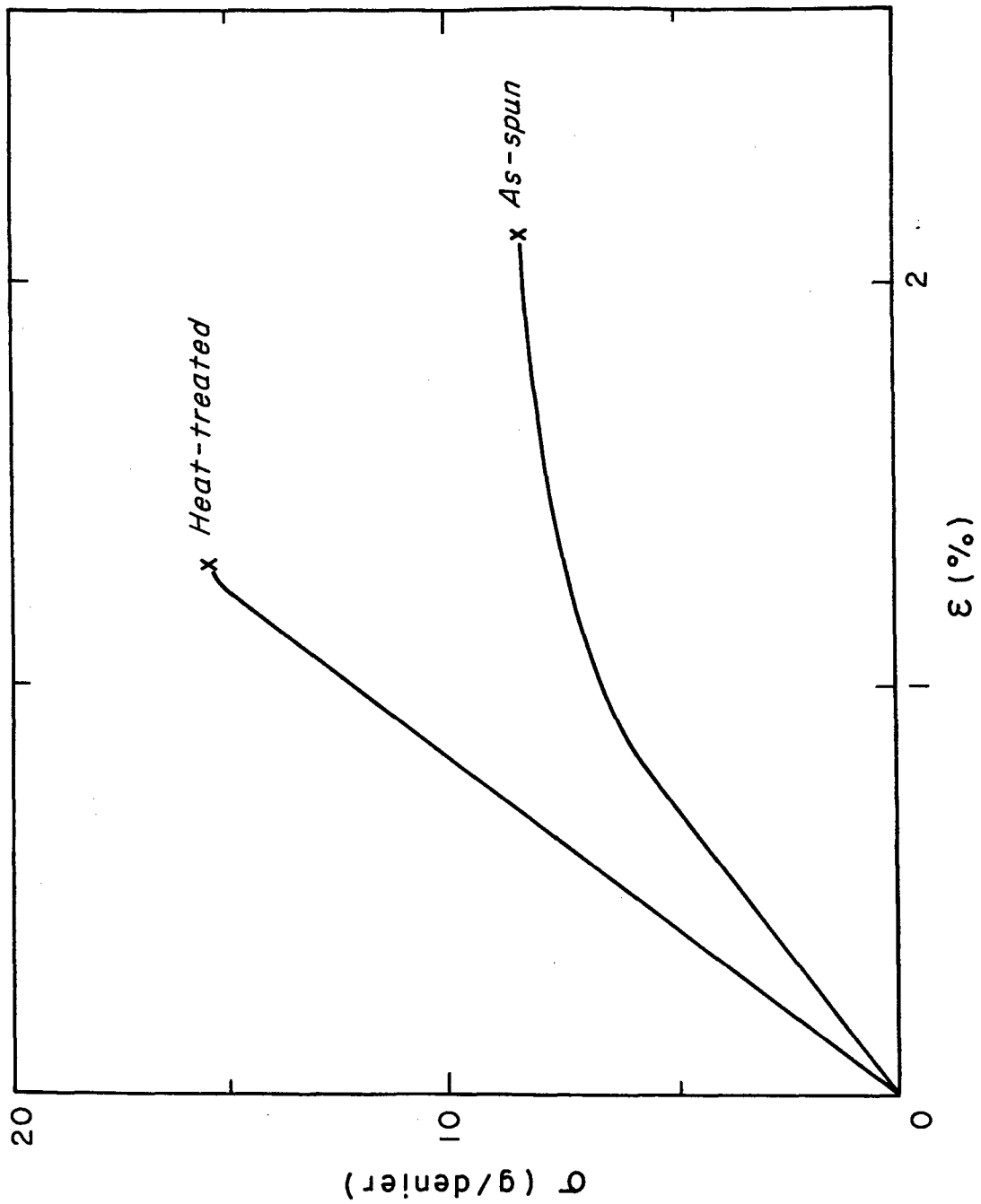


Figure 4.3: Comparison of heat treated and as-spun fiber behavior

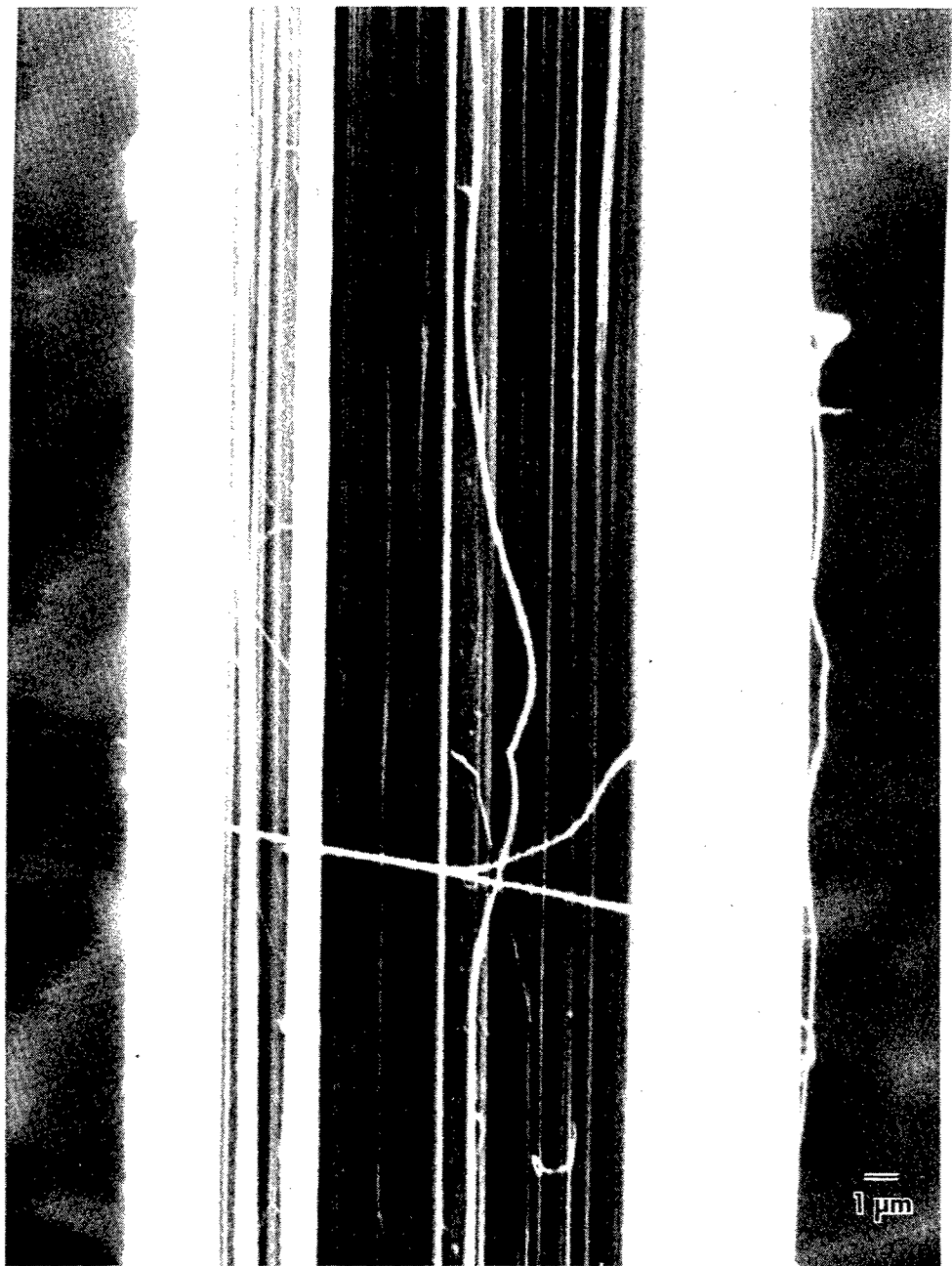


Figure 4.4: Fibrillar morphology of PBT fibers revealed by mechanical peeling

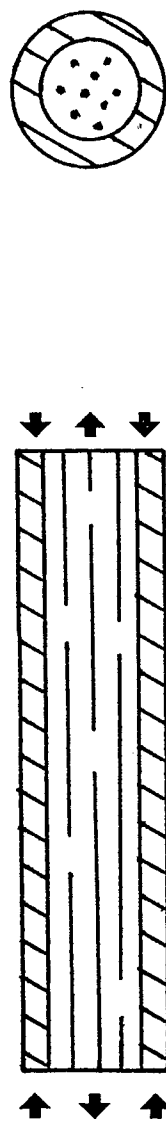


Figure 4.5: Representation of axial residual stresses in as-spun fibers

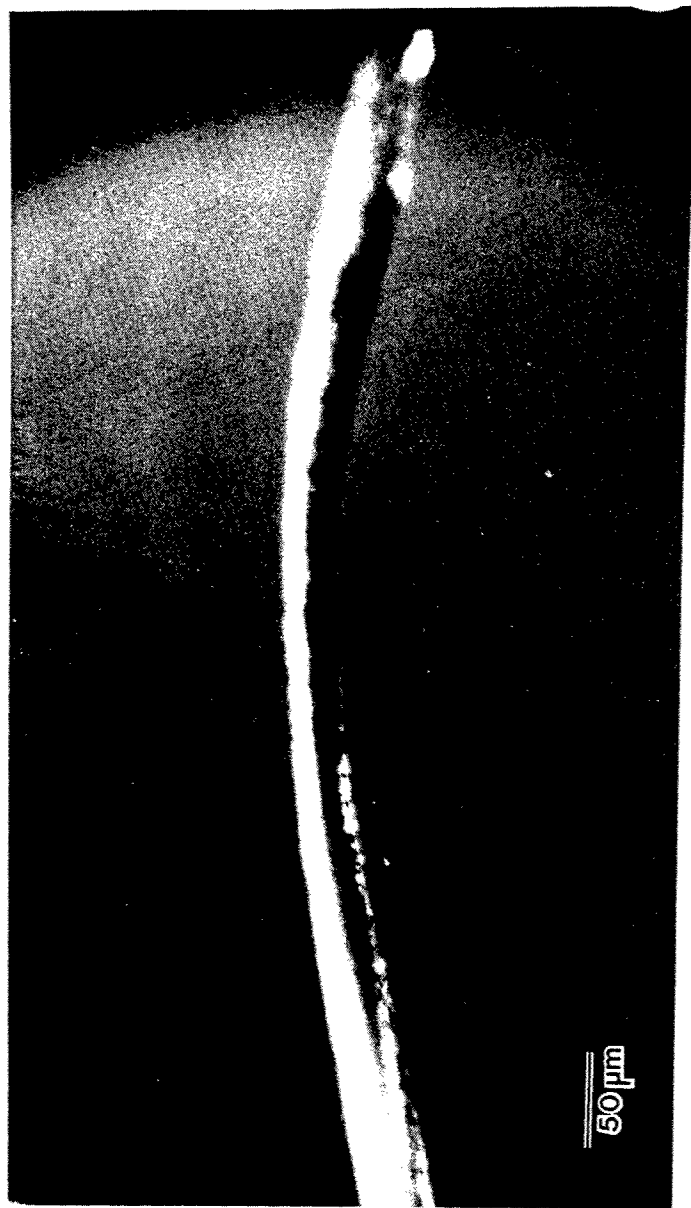


Figure 4.6: Optical micrograph of laser damaged as-spun PBT fiber

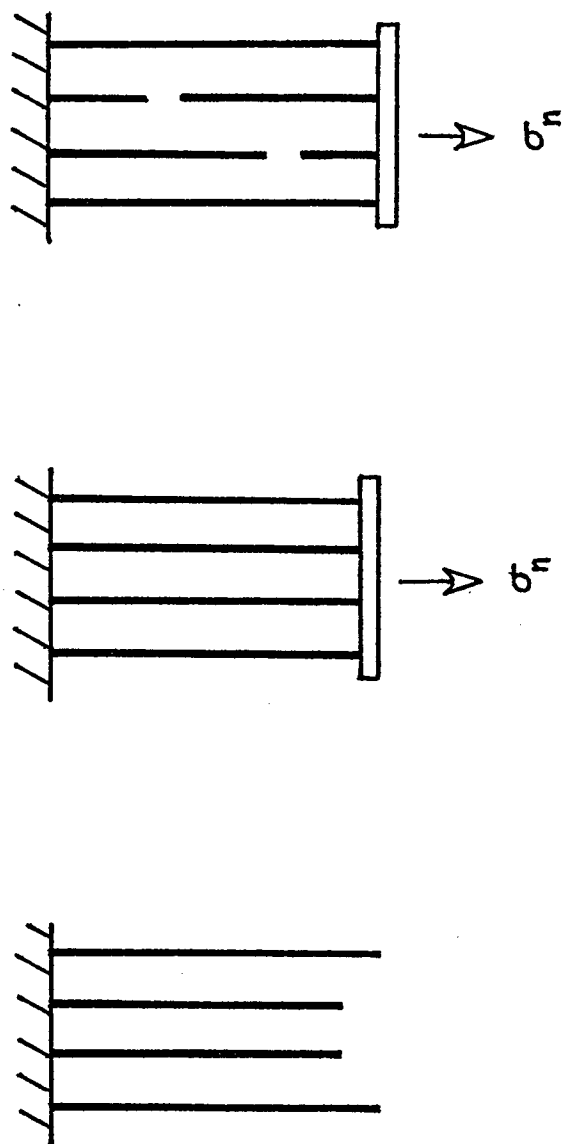


Figure 4.7: Residual stress structural model

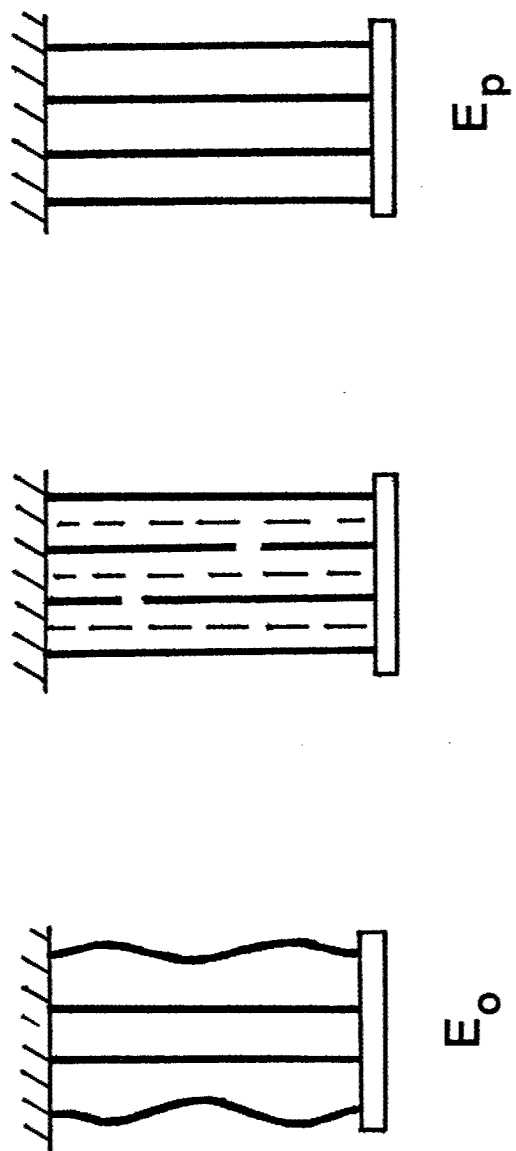
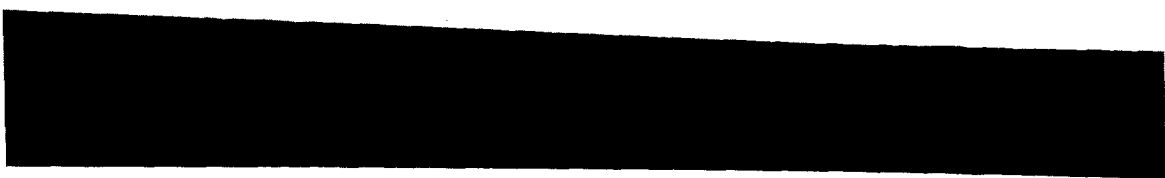


Figure 4.8: Residual stress structural model with buckling of compressed elements

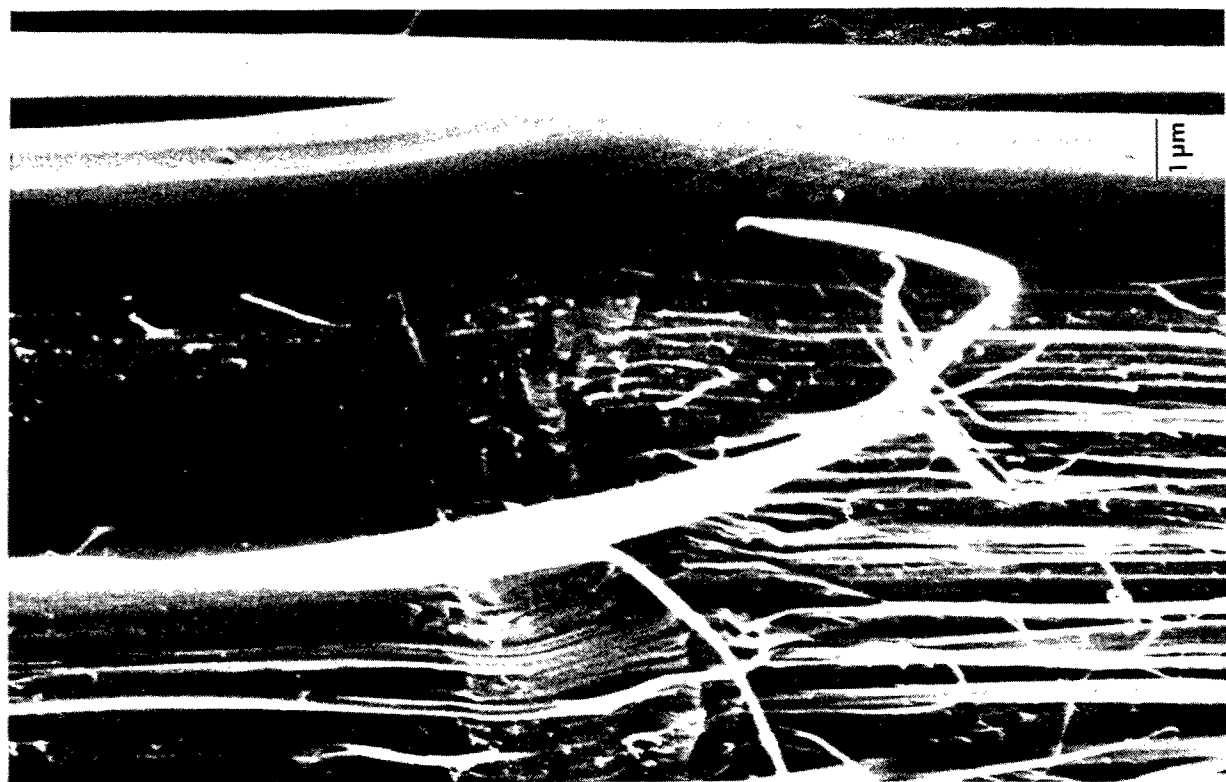


b



a

Figure 4.9: Surface of (a) as-spun undeformed and (b) as-spun deformed fibers



a



b

Figure 4.10: Mechanically peeled fibers (a) as-spun undeformed (b) as-spun deformed

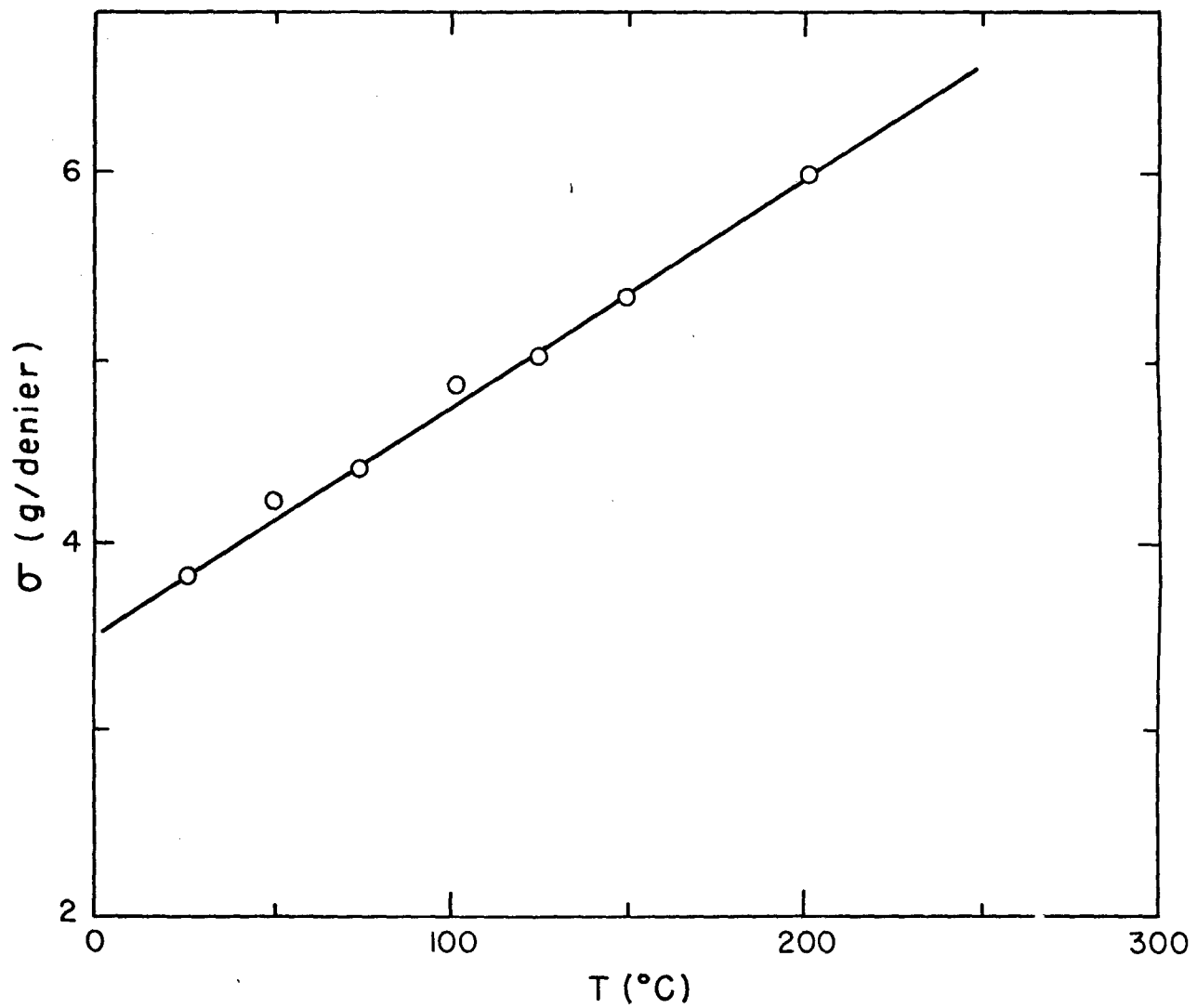


Figure 4.11: Dependence of fiber yield stress on free annealing temperature

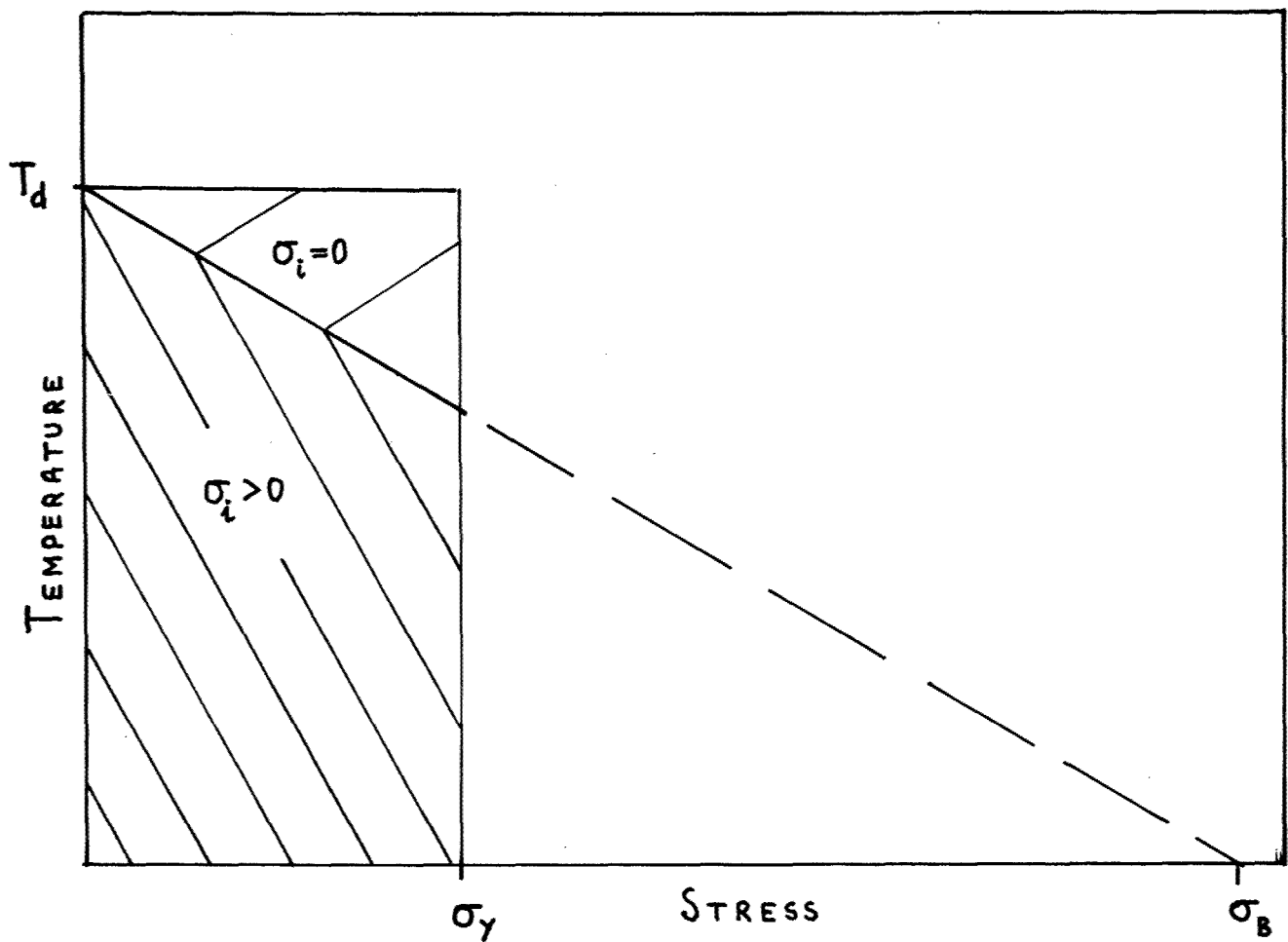


Figure 4.12: Stress-temperature bounds for relief of residual stresses

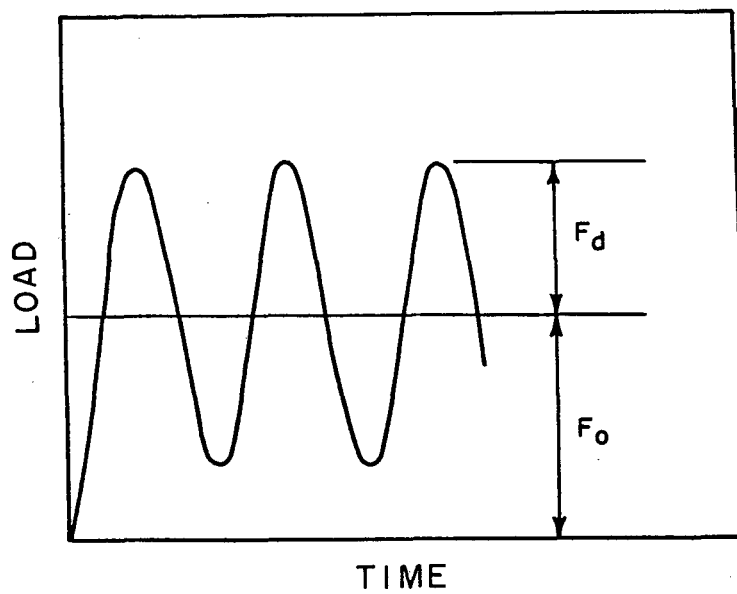


Figure 4.13: Loading conditions for fatigue testing
 F_d = dynamic force, F_0 = steady force

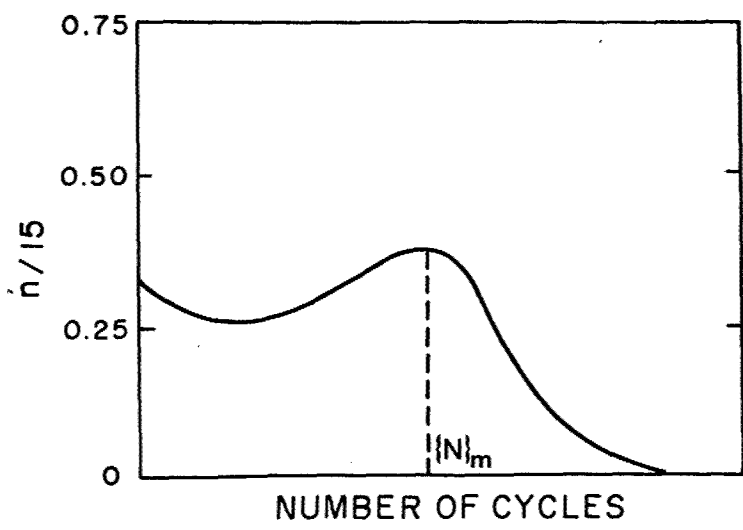


Figure 4.14: The distribution of the number of specimens (n) as a function of lifetime in fatigue tests

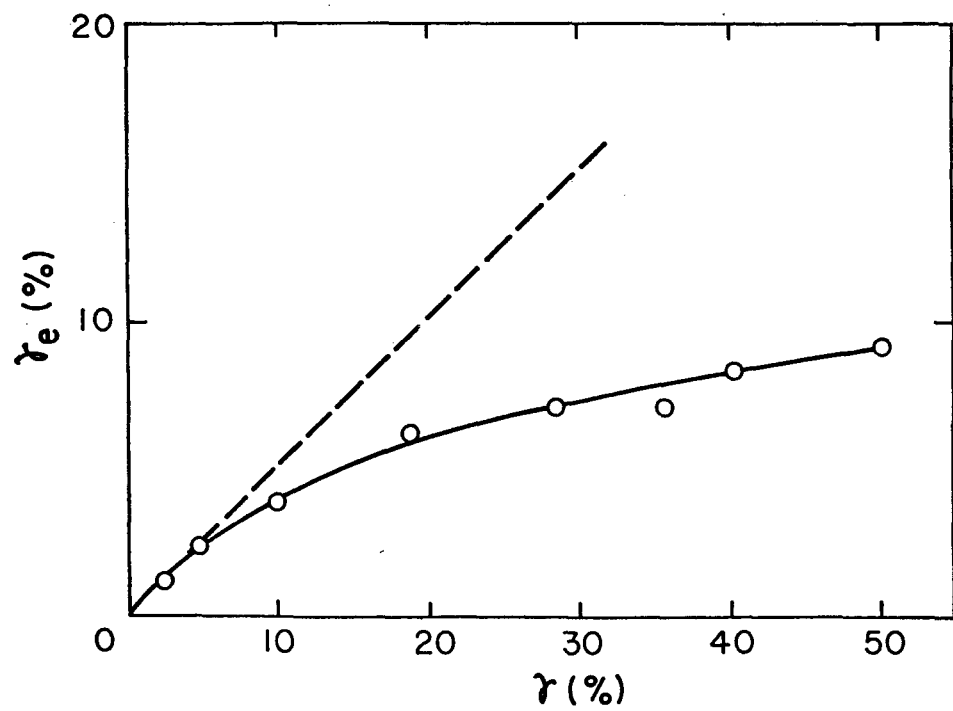


Figure 4.15: Elastic component of twisting strain (γ_e) as a function of total strain (γ)

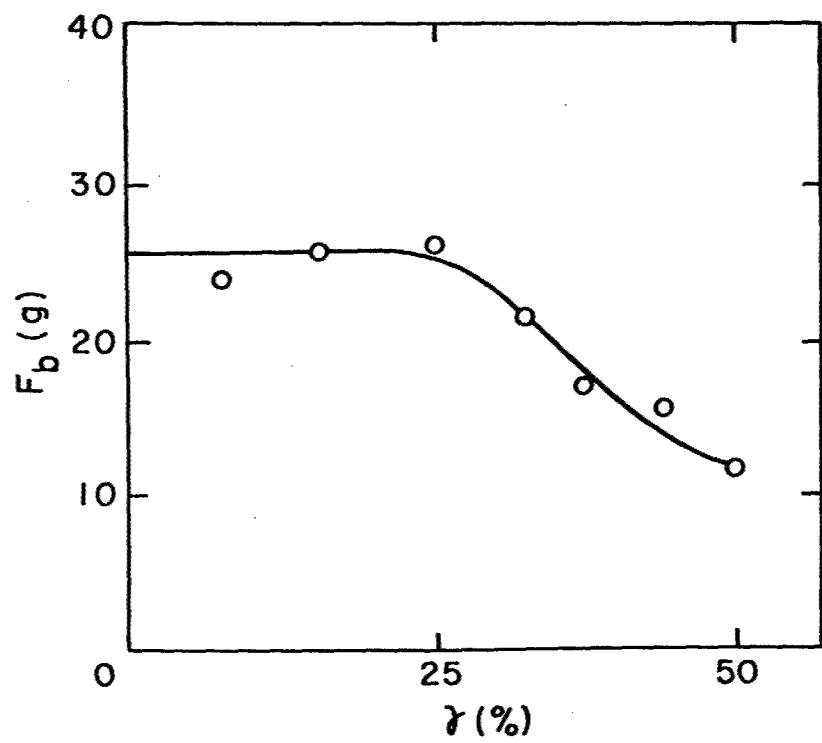


Figure 4.16: Effect of twisting on longitudinal strength of PBT fibers

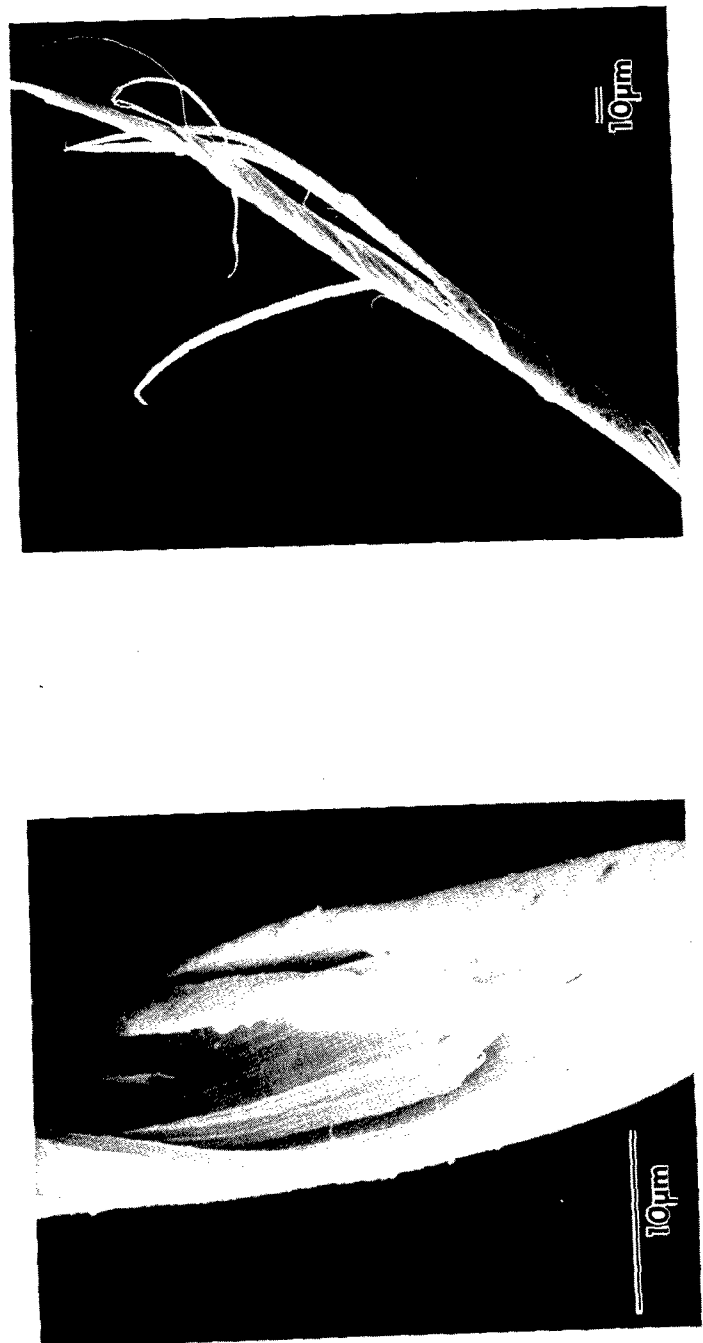


Figure 4.17: SEM micrographs of fracture surface of PBT fiber in torsion-tension test

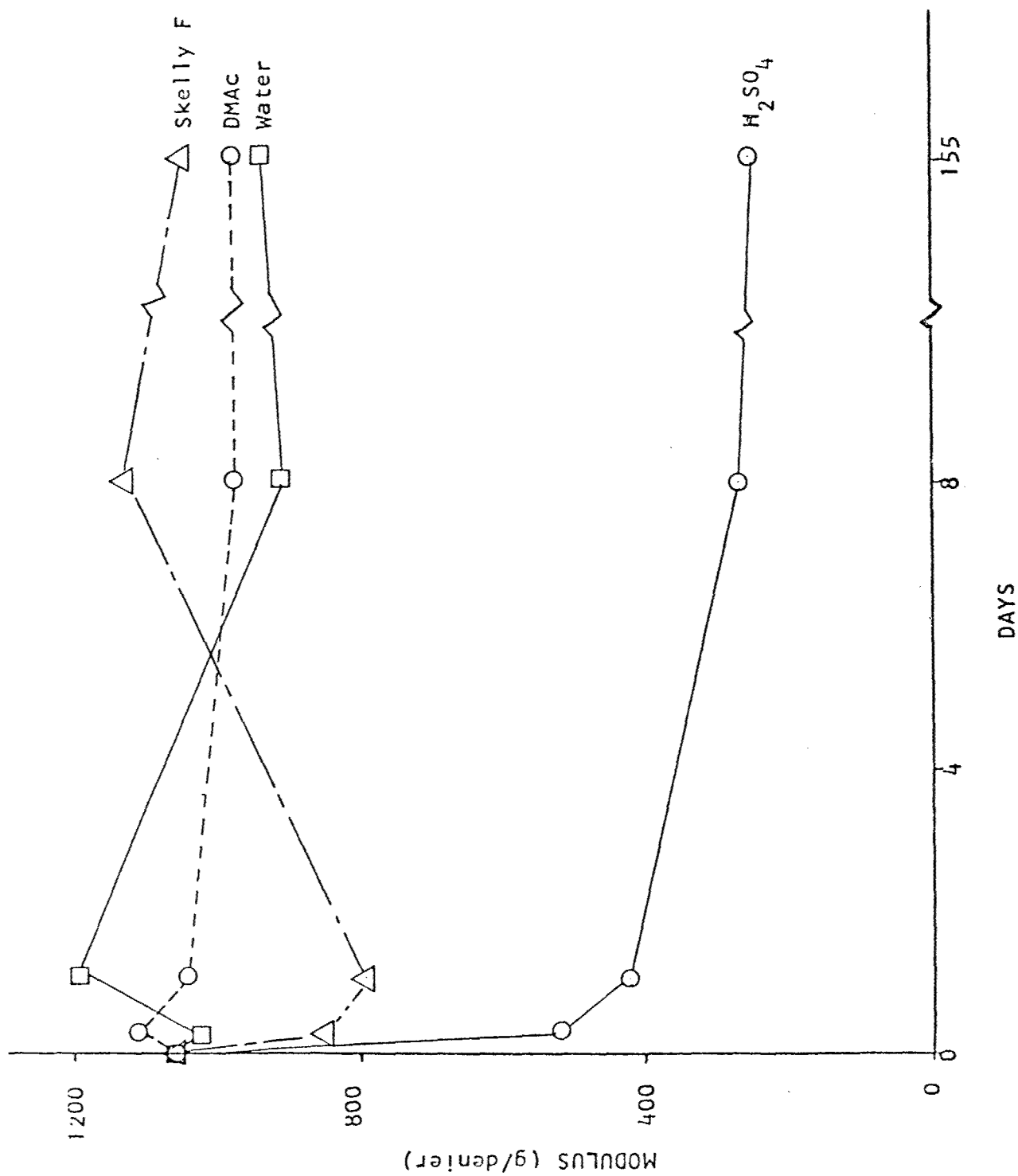


Figure 4.18: Effect of exposure to harsh environment on fiber modulus

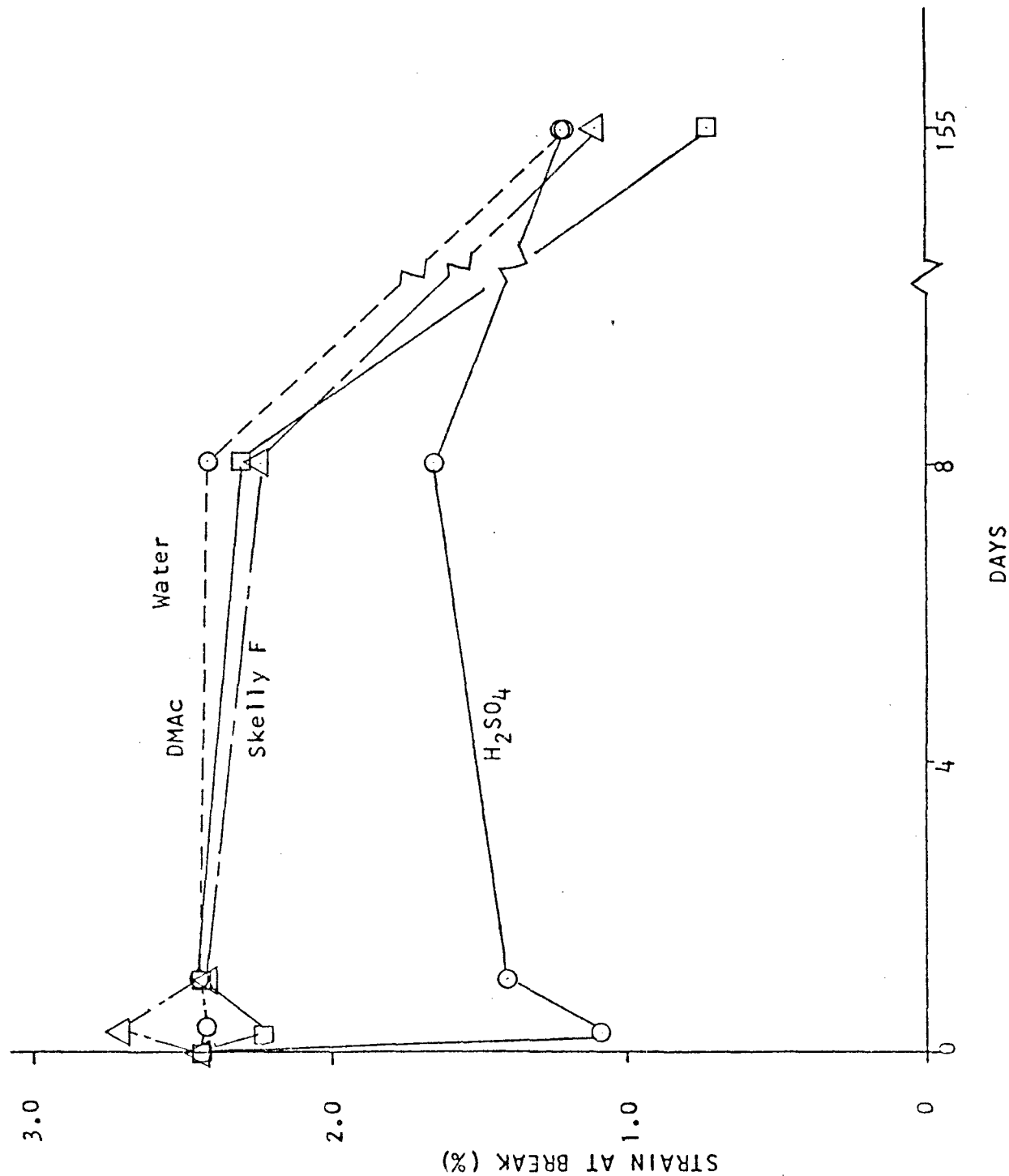


Figure 4.19: Effect of exposure to harsh environments on fiber strain at break

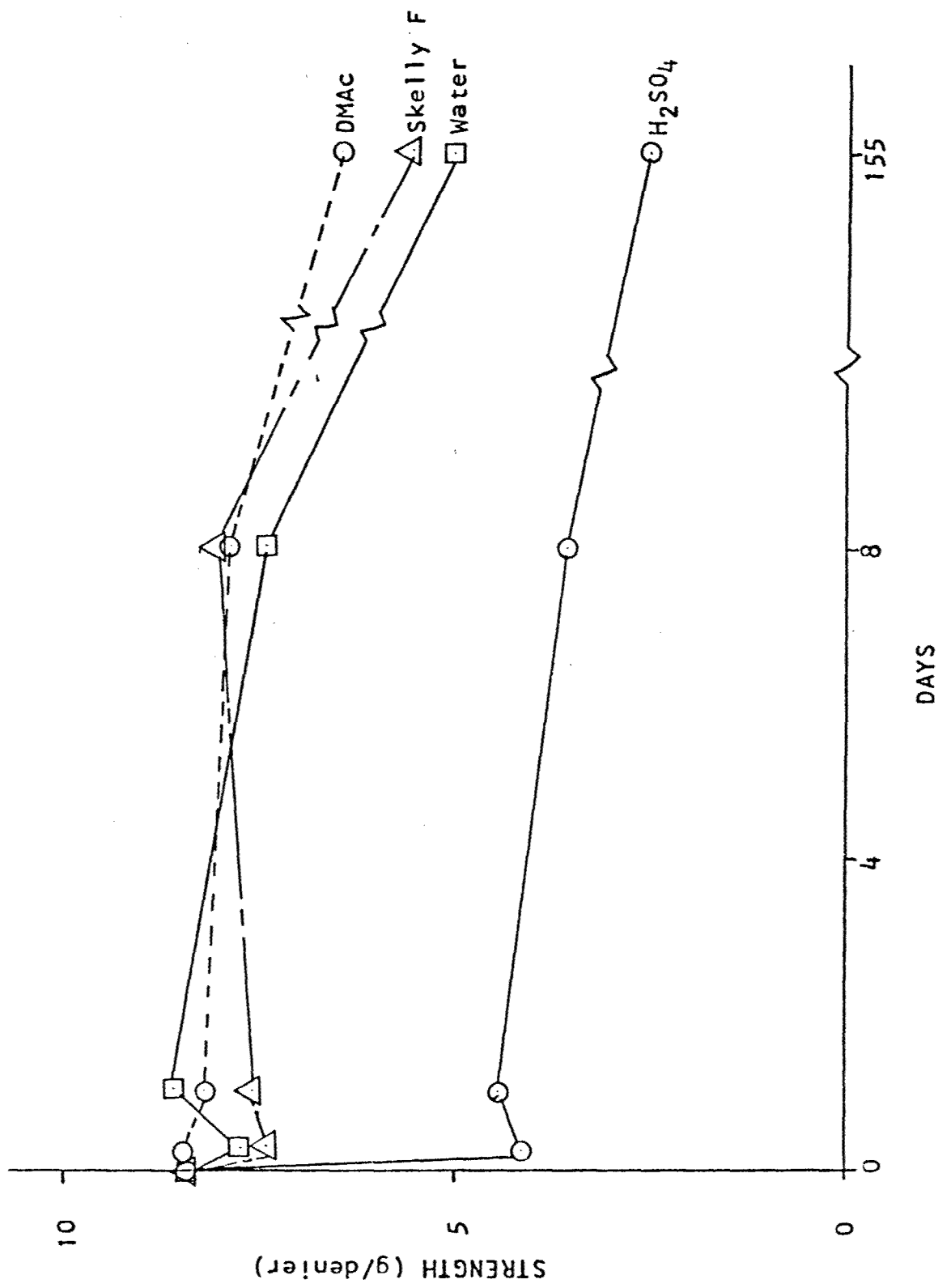


Figure 4.20: Effect of exposure to harsh environments on fiber strength

REFERENCES

1. G.C. Berry, *J. Polym. Sci. - Polym. Symposia* 65, 143 (1978).
2. C.P. Wong, H. Ohnuma and G.C. Berry, *J. Polym. Sci. - Polym. Symposia* 65, 173 (1978).
3. G.C. Berry, P.C. Metzger, S. Venkatraman and D.B. Cotts, *Polymer Preprints*, 20(1), 42 (1979).
4. L. Penn and F. Milanovich, *Polymer*, 20, 31 (1979).
5. K. Haraguchi, T. Kajiyama and M. Takayanagi, *J. Appl. Polym. Sci.*, 23, 915 (1979).
6. P.P. Shorygin, *Zh. Fiz. Khim.*, 15, 1075 (1941).
7. J. Behringer, in *Raman Spectroscopy*, H.Z. Szymanski (Ed.), Plenum Press, N.Y. (1967).
8. M.W. Wellman, W.W. Adams, D.S. Dudes, D.R. Wiff and A.V. Fratini, *Amer. Cryst. Assoc. Proceed. Abstracts*, Boston (August, 1979).
9. F.R. Dollish, W.G. Fateley and F.F. Bentley, *Characteristic Raman Frequencies of Organic Compounds*, John Wiley & Sons, N.Y. (1974).
10. H.H. Jaffe and M. Orchin, *Theory and Applications of Ultraviolet Spectroscopy*, Wiley and Sons, N.Y. (1962), p. 430.
11. E.D. Schmid and B. Brosa, *J. Chem. Phys.*, 56, 6267 (1972).
12. W.J. Welsh, P. Bhaumik and J.E. Mark, First Annual Report for Air Force Office of Scientific Research, No. 78-3683 (November, 1979).
13. A.V. Fratini, *private communication*.
14. M.M. Cordes and J.L. Walter, *Spectrochim. Acta*, 24A, 237, 1421 (1968).

15. G. Sbrana, E. Castellucci and M. Ginanneschi, *Spectrochim. Acta* 23A, 751 (1967).
16. A. Leifer, D. Bonis, M. Collins, P. Dougherty, A.J. Fusco, M. Koral and J.E. LuValle, *Spectrochim. Acta*, 20, 909 (1964).
17. J.K. Wilmhurst and H.J. Bernstein, *Can. J. Chem.*, 35, 1183 (1957).
18. R. Foglizzo and A. Novak, *J. Chim. Phys.*, 66, 1539 (1969).
19. K.W.F. Kohlrausch and R. Seka, *Chem. Ber.*, 71, 1563 (1938).
20. G.M. Venkatesh and S.L. Hsu, submitted for publication.
21. V.N. Filimonov and D.S. Bystrov, *Optics and Spectroscopy* 12, 31 (1962); and the pertinent references cited therein.
22. W.W. Adams, L.V. Azaroff, and A.K. Kulshreshtha, *Zeitschrift fur Kristallographie* 150, 321-326 (1979).
23. E.J. Roche, T. Takahashi and E.L. Thomas: A. French and K. Gardner, eds. Fiber Diffraction Methods, ACS Symposium Series #141, pp. 303-314 American Chemical Society, Washington, D.C., 1980.
24. E.D.T. Atkins, private communications.
25. S. Chandrasekhar, Liquid Crystals, Cambridge (1977).
26. J. Nehring and A. Sanpe, *J. Chem. Soc. (London) Faraday Transactions II*, 68, 1-15 (1972).
27. L.S. Singer, "High Modulus Fibers from Mesophase Pitch" Ch. 9 in A. Ciferri and I.M. Ward (Eds.), Ultra High Modulus Fibers, Applied Science, London (1979).
28. E.C. Chenevey, Contract # F33615-79-C-5071, Processing of Rodlike Polymers, Letter Report #1, June 1980.
29. D.C. Bassett, "Surface Detachment from Polyethylene Crystals", *Phil. Mag.*, 6, 103 (1961).
30. D.T. Grubb and G.W. Groves "Rate of Damage of Polymer Crystals in the Electron Microscope: Dependence on Temperature and Beam Voltage", *Phil. Mag.*, 24, 815-828 (1971).

31. M.G. Dobb, D.J. Johnson, and B.P. Saville, "Direct Observation of Structure in High Modulus Aromatic Fibers", *J. Polym. Sci: Polym. Symp.*, 58, 237-251 (1977).
32. M.G. Dobb, D.J. Johnson and B.P. Saville, "Structural Aspects of High Modulus Aromatic Polyamide Fibers", *Phil. Trans. Roy. Soc. London A*, 294, 483-485 (1979).
33. M.W. Wellman, W.W. Adams, D.R. Wiff and A.V. Fratini, AFML-TR-79-4184, Part I (1979).
34. A. Peterlin, *Int. J. of Fracture*, 11, 761-780 (1975).
35. A.R. Bunsell, *J. Mater. Sci.*, 10, 1300-1308 (1975).

U.S. GOVERNMENT PRINTING OFFICE: 1981-757-002/13